



ASTRO-H Space X-ray Observatory White Paper

Clusters of Galaxies and Related Science

T. Kitayama (Toho University), M. Bautz (MIT), M. Markevitch (NASA/GSFC),
 K. Matsushita (Tokyo University of Science), S. Allen (Stanford University), M. Kawaharada (JAXA),
 B. McNamara (University of Waterloo), N. Ota (Nara Women's University), H. Akamatsu (SRON),
 J. de Plaa (SRON), M. Galeazzi (University of Miami), G. Madejski (Stanford University),
 R. Main (University of Waterloo), E. Miller (MIT), K. Nakazawa (University of Tokyo), H. Russel (University
 of Waterloo¹), K. Sato (Tokyo University of Science), N. Sekiya (JAXA/University of Tokyo),
 A. Simionescu (JAXA), T. Tamura (JAXA), Y. Uchida (JAXA/University of Tokyo), E. Ursino (University
 of Miami), N. Werner (Stanford University), I. Zhuravleva (Stanford University), and J. ZuHone
 (NASA/GSFC)

on behalf of the ASTRO-H Science Working Group

Abstract

The next generation X-ray observatory *ASTRO-H* will open up a new dimension in the study of galaxy clusters by achieving for the first time the spectral resolution required to measure velocities of the intracluster plasma, and extending at the same time the spectral coverage to energies well beyond 10 keV. This white paper provides an overview of the capabilities of *ASTRO-H* for exploring gas motions in galaxy clusters including their cosmological implications, the physics of AGN feedback, dynamics of cluster mergers as well as associated high-energy processes, chemical enrichment of the intracluster medium, and the nature of missing baryons and unidentified dark matter.

¹Also at Institute of Astronomy, University of Cambridge

Complete list of the ASTRO-H Science Working Group

Tadayuki Takahashi^a, Kazuhisa Mitsuda^a, Richard Kelley^b, Felix Aharonian^c, Hiroki Akamatsu^d, Fumie Akimoto^e, Steve Allen^f, Naohisa Anabuki^g, Lorella Angelini^b, Keith Arnaud^b, Marc Audardⁱ, Hisamitsu Awaki^j, Aya Bamba^k, Marshall Bautz^l, Roger Blandford^f, Laura Brenneman^b, Greg Brown^m, Edward Cackettⁿ, Maria Chernyakova^c, Meng Chiao^b, Paolo Coppi^o, Elisa Costantini^d, Jelle de Plaa^d, Jan-Willem den Herder^d, Chris Done^p, Tadayasu Dotani^a, Ken Ebisawa^a, Megan Eckart^b, Teruaki Enoto^q, Yuichiro Ezoe^r, Andrew Fabianⁿ, Carlo Ferrignoⁱ, Adam Foster^s, Ryuichi Fujimoto^t, Yasushi Fukazawa^u, Stefan Funk^f, Akihiro Furuzawa^e, Massimiliano Galeazzi^v, Luigi Gallo^w, Poshak Gandhi^p, Matteo Guainazzi^x, Yoshito Haba^y, Kenji Hamaguchi^h, Isamu Hatsukade^z, Takayuki Hayashi^a, Katsuhiro Hayashi^a, Kiyoshi Hayashida^g, Junko Hiraga^{aa}, Ann Hornschemeier^b, Akio Hoshino^{ab}, John Hughes^{ac}, Una Hwang^{ad}, Ryo Iizuka^a, Yoshiyuki Inoue^a, Hajime Inoue^a, Kazunori Ishibashi^e, Manabu Ishida^a, Kumi Ishikawa^q, Yoshitaka Ishisaki^f, Masayuki Ito^{ae}, Naoko Iyomoto^{af}, Jelle Kaastra^d, Timothy Kallman^b, Tuneyoshi Kamae^f, Jun Kataoka^{ag}, Satoru Katsuda^a, Junichiro Katsuta^u, Madoka Kawaharada^a, Nobuyuki Kawai^{ah}, Dmitry Khangulyan^a, Caroline Kilbourne^b, Masashi Kimura^{ai}, Shunji Kitamoto^{ab}, Tetsu Kitayama^{aj}, Takayoshi Kohmura^{ak}, Motohide Kokubun^a, Saori Konami^r, Katsuji Koyama^{al}, Hans Krimm^b, Aya Kubota^{am}, Hideyo Kunieda^e, Stephanie LaMassa^o, Philippe Laurent^{an}, François Lebrun^{an}, Maurice Leutenegger^b, Olivier Limousin^{an}, Michael Loewenstein^b, Knox Long^{ao}, David Lumb^{ap}, Grzegorz Madejski^f, Yoshitomo Maeda^a, Kazuo Makishima^{aa}, Maxim Markevitch^b, Hironori Matsumoto^e, Kyoko Matsushita^{aq}, Dan McCammon^{af}, Brian McNamara^{as}, Jon Miller^{at}, Eric Miller^l, Shin Mineshige^{au}, Ikuyuki Mitsuishi^e, Takuya Miyazawa^e, Tsunefumi Mizuno^u, Koji Mori^z, Hideyuki Mori^e, Koji Mukai^b, Hiroshi Murakami^{av}, Toshio Murakami^t, Richard Mushotzky^h, Ryo Nagino^g, Takao Nakagawa^a, Hiroshi Nakajima^g, Takeshi Nakamori^{aw}, Shinya Nakashima^a, Kazuhiro Nakazawa^{aa}, Masayoshi Nobukawa^{al}, Hirofumi Noda^q, Masaharu Nomachi^{ax}, Steve O' Dell^{ay}, Hirokazu Odaka^a, Takaya Ohashi^r, Masanori Ohno^u, Takashi Okajima^b, Naomi Ota^{az}, Masanobu Ozaki^a, Frits Paerels^{ba}, Stéphane Paltaniⁱ, Arvind Parmar^x, Robert Petre^b, Ciro Pintoⁿ, Martin Pohlⁱ, F. Scott Porter^b, Katja Pottschmidt^b, Brian Ramsey^{ay}, Rubens Reis^{at}, Christopher Reynolds^h, Claudio Ricci^{au}, Helen Russellⁿ, Samar Safi-Harb^{bb}, Shinya Saito^a, Hiroaki Sameshima^a, Goro Sato^{ag}, Kosuke Sato^{aq}, Rie Sato^a, Makoto Sawada^k, Peter Serlemitsos^b, Hiromi Seta^{bc}, Aurora Simionescu^a, Randall Smith^s, Yang Soong^b, Łukasz Stawarz^a, Yasuharu Sugawara^{bd}, Satoshi Sugita^j, Andrew Szymkowiak^o, Hiroyasu Tajima^e, Hiromitsu Takahashi^u, Hiroaki Takahashi^g, Yoh Takei^a, Toru Tamagawa^q, Takayuki Tamura^a, Keisuke Tamura^e, Takaaki Tanaka^{al}, Yasuo Tanaka^a, Yasuyuki Tanaka^u, Makoto Tashiro^{bc}, Yuzuru Tawara^e, Yukikatsu Terada^{bc}, Yuichi Terashima^j, Francesco Tombesi^b, Hiroshi Tomida^{ai}, Yohko Tsuboi^{bd}, Masahiro Tsujimoto^a, Hiroshi Tsunemi^g, Takeshi Tsuru^{al}, Hiroyuki Uchida^{al}, Yasunobu Uchiyama^{ab}, Hideki Uchiyama^{be}, Yoshihiro Ueda^{au}, Shutaro Ueda^g, Shiro Ueno^{ai}, Shinichiro Uno^{bf}, Meg Urry^o, Eugenio Ursino^v, Cor de Vries^d, Shin Watanabe^a, Norbert Werner^f, Dan Wilkins^w, Shinya Yamada^r, Hiroya Yamaguchi^b, Kazutaka Yamaoka^e, Noriko Yamasaki^a, Makoto Yamauchi^z, Shigeo Yamauchi^{az}, Tahir Yaqoob^b, Yoichi Yatsu^{ah}, Daisuke Yonetoku^t, Atsumasa Yoshida^k, Takayuki Yuasa^q, Irina Zhuravleva^f, Abderahmen Zoghbi^h, and John ZuHone^b

^aInstitute of Space and Astronautical Science (ISAS), Japan Aerospace Exploration Agency (JAXA), Kanagawa 252-5210, Japan

^bNASA/Goddard Space Flight Center, MD 20771, USA

^cAstronomy and Astrophysics Section, Dublin Institute for Advanced Studies, Dublin 2, Ireland

^dSRON Netherlands Institute for Space Research, Utrecht, The Netherlands

^eDepartment of Physics, Nagoya University, Aichi 338-8570, Japan

^fKavli Institute for Particle Astrophysics and Cosmology, Stanford University, CA 94305, USA

^gDepartment of Earth and Space Science, Osaka University, Osaka 560-0043, Japan

^hDepartment of Astronomy, University of Maryland, MD 20742, USA

ⁱUniversité de Genève, Genève 4, Switzerland

^jDepartment of Physics, Ehime University, Ehime 790-8577, Japan

^kDepartment of Physics and Mathematics, Aoyama Gakuin University, Kanagawa 229-8558, Japan

^lKavli Institute for Astrophysics and Space Research, Massachusetts Institute of Technology, MA 02139, USA

^mLawrence Livermore National Laboratory, CA 94550, USA

ⁿInstitute of Astronomy, Cambridge University, CB3 0HA, UK

^oYale Center for Astronomy and Astrophysics, Yale University, CT 06520-8121, USA

^pDepartment of Physics, University of Durham, DH1 3LE, UK

^qRIKEN, Saitama 351-0198, Japan

^rDepartment of Physics, Tokyo Metropolitan University, Tokyo 192-0397, Japan

^sHarvard-Smithsonian Center for Astrophysics, MA 02138, USA

- ^tFaculty of Mathematics and Physics, Kanazawa University, Ishikawa 920-1192, Japan
- ^uDepartment of Physical Science, Hiroshima University, Hiroshima 739-8526, Japan
- ^vPhysics Department, University of Miami, FL 33124, USA
- ^wDepartment of Astronomy and Physics, Saint Mary's University, Nova Scotia B3H 3C3, Canada
- ^xEuropean Space Agency (ESA), European Space Astronomy Centre (ESAC), Madrid, Spain
- ^yDepartment of Physics and Astronomy, Aichi University of Education, Aichi 448-8543, Japan
- ^zDepartment of Applied Physics, University of Miyazaki, Miyazaki 889-2192, Japan
- ^{aa}Department of Physics, University of Tokyo, Tokyo 113-0033, Japan
- ^{ab}Department of Physics, Rikkyo University, Tokyo 171-8501, Japan
- ^{ac}Department of Physics and Astronomy, Rutgers University, NJ 08854-8019, USA
- ^{ad}Department of Physics and Astronomy, Johns Hopkins University, MD 21218, USA
- ^{ae}Faculty of Human Development, Kobe University, Hyogo 657-8501, Japan
- ^{af}Kyushu University, Fukuoka 819-0395, Japan
- ^{ag}Research Institute for Science and Engineering, Waseda University, Tokyo 169-8555, Japan
- ^{ah}Department of Physics, Tokyo Institute of Technology, Tokyo 152-8551, Japan
- ^{ai}Tsukuba Space Center (TKSC), Japan Aerospace Exploration Agency (JAXA), Ibaraki 305-8505, Japan
- ^{aj}Department of Physics, Toho University, Chiba 274-8510, Japan
- ^{ak}Department of Physics, Tokyo University of Science, Chiba 278-8510, Japan
- ^{al}Department of Physics, Kyoto University, Kyoto 606-8502, Japan
- ^{am}Department of Electronic Information Systems, Shibaura Institute of Technology, Saitama 337-8570, Japan
- ^{an}IRFU/Service d'Astrophysique, CEA Saclay, 91191 Gif-sur-Yvette Cedex, France
- ^{ao}Space Telescope Science Institute, MD 21218, USA
- ^{ap}European Space Agency (ESA), European Space Research and Technology Centre (ESTEC), 2200 AG Noordwijk, The Netherlands
- ^{aq}Department of Physics, Tokyo University of Science, Tokyo 162-8601, Japan
- ^{ar}Department of Physics, University of Wisconsin, WI 53706, USA
- ^{as}University of Waterloo, Ontario N2L 3G1, Canada
- ^{at}Department of Astronomy, University of Michigan, MI 48109, USA
- ^{au}Department of Astronomy, Kyoto University, Kyoto 606-8502, Japan
- ^{av}Department of Information Science, Faculty of Liberal Arts, Tohoku Gakuin University, Miyagi 981-3193, Japan
- ^{aw}Department of Physics, Faculty of Science, Yamagata University, Yamagata 990-8560, Japan
- ^{ax}Laboratory of Nuclear Studies, Osaka University, Osaka 560-0043, Japan
- ^{ay}NASA/Marshall Space Flight Center, AL 35812, USA
- ^{az}Department of Physics, Faculty of Science, Nara Women's University, Nara 630-8506, Japan
- ^{ba}Department of Astronomy, Columbia University, NY 10027, USA
- ^{bb}Department of Physics and Astronomy, University of Manitoba, MB R3T 2N2, Canada
- ^{bc}Department of Physics, Saitama University, Saitama 338-8570, Japan
- ^{bd}Department of Physics, Chuo University, Tokyo 112-8551, Japan
- ^{be}Science Education, Faculty of Education, Shizuoka University, Shizuoka 422-8529, Japan
- ^{bf}Faculty of Social and Information Sciences, Nihon Fukushi University, Aichi 475-0012, Japan

Contents

1	Executive Summary: Opening a New Dimension in Galaxy Cluster Research	6
2	Nature of Gas Motions in the X-ray Brightest Galaxy Cluster	8
2.1	Background and Previous Studies	8
2.1.1	Gas motions in cool core clusters	8
2.1.2	The Perseus Cluster	9
2.2	Prospects and Strategy	10
2.2.1	The nature of gas motions	10
2.2.2	Temperature structure and cooling	14
2.3	Targets and Feasibility	15
2.3.1	Dynamics of the intra-cluster medium	15
2.3.2	The temperature structure of the ICM	19
2.3.3	Chemical abundance measurements	20
2.3.4	The AGN emission	20
2.3.5	Diffuse non-thermal emission	22
2.4	Remarks on sources of systematic uncertainty	22
3	A Detailed View of AGN Feedback	22
3.1	Background and Previous Studies	23
3.1.1	The cooling flow problem and the necessity for AGN feedback	23
3.1.2	Previous observations of AGN feedback in M87	23
3.2	Prospects and Strategy	24
3.2.1	Dynamics of gas uplift	24
3.2.2	AGN-induced metal transport	24
3.2.3	Turbulent motions in the hot ICM	25
3.3	Targets and Feasibility	25
3.3.1	The central pointing	26
3.3.2	The offset pointings	27
3.4	Remarks on sources of systematic uncertainty	29
3.5	Beyond Feasibility	29
4	Plasma Kinematics and Cluster Masses	31
4.1	Background and Previous Studies	31
4.2	Prospects and Strategy	33
4.3	Targets and Feasibility	34
4.3.1	Abell 2029	35
4.3.2	Abell 2199	36
4.3.3	Abell 1795	37
4.3.4	Abell 478	42
4.4	Discussion	42
4.5	Beyond Feasibility	46
5	Mapping Gas Flows and Turbulence in Merging Galaxy Clusters	47
5.1	Background and Previous Studies	48
5.2	Prospects and Strategy	49
5.3	Targets and Feasibility	50
5.3.1	Coma	52
5.3.2	A3667	52
5.3.3	A2319	55

5.3.4	A754	56
5.3.5	A2256	56
5.4	Beyond Feasibility	57
6	High-energy Processes	57
6.1	Background and Previous Studies	57
6.2	Prospects and Strategy	58
6.3	Targets and Feasibility	59
6.3.1	The NW relic of Abell 3667	59
6.3.2	Very hot gas at the center of Abell 3667	60
6.3.3	Coma cluster	61
6.4	Lessons Learned from <i>NuSTAR</i>	62
7	Chemical Composition and Evolution	63
7.1	Background and Previous Studies	64
7.2	Prospects and Strategy	66
7.3	Targets and Feasibility	67
7.3.1	The metals in the cool cores	67
7.3.2	Metal distributions outside cool-cores	70
7.3.3	NGC 5044 and galaxies	71
7.4	Beyond Feasibility	71
7.4.1	Detection of rare elements	71
7.4.2	Abundances as a function of redshift	72
8	Detecting and Characterizing the Warm-Hot Intergalactic Medium	72
8.1	Background and Previous Studies	73
8.2	Prospects and Strategy	74
8.3	Targets and Feasibility	75
8.3.1	Between A222 and A223	76
8.3.2	Between A3556 and A3558 in the Shapley supercluster	78
8.4	Between A2804 and A2811 in the Sculptor supercluster	78
8.4.1	Science outcome	79
9	A Spectroscopic Search for Dark Matter	80
9.1	Background and Previous Studies	80
9.2	Prospects and Strategy	80
9.3	Targets and Feasibility	81
A	Systematic Errors in Gas Velocities	83
A.1	Bulk Velocity	83
A.2	Turbulent Velocity	84
A.2.1	Instrumental broadening	85
A.2.2	Thermal broadening	87
A.2.3	Combined error	87

1 Executive Summary: Opening a New Dimension in Galaxy Cluster Research

The *ASTRO-H* satellite, the first X-ray observatory with a focal plane calorimeter, will open up a new dimension in the research of galaxy clusters. The high energy resolution of the non-dispersive Soft X-ray Spectrometer (SXS) will make it possible to detect dozens of emission lines from highly ionized ions and measure, for the first time, their line profiles with sufficient accuracy to study gas motions. The Hard X-ray Imager (HXI) will extend the simultaneous spectral coverage to energies well above 10 keV, which is critical for studying both thermal and nonthermal gas in clusters.

The present white paper aims to demonstrate the above capabilities explicitly on representative galaxy clusters to aid and encourage the broader astrophysical community in developing *ASTRO-H* science. It is a compilation of documents showing detailed feasibility studies done by the *ASTRO-H* Science Working Group in an effort to select targets for the Performance Verification phase of the mission. As such, each section is intended to provide a self-contained description of its subject and to be accessible independently of the other sections. In this section, we summarize a range of science topics covered in the paper and guide the readers to the subsequent sections for more details of new results expected from early observations of *ASTRO-H*.¹

From cluster dynamics to plasma microphysics

Clusters of galaxies form via the infall and accretion of surrounding matter, including smaller clusters and galaxy groups. In the course of a merger, a significant fraction of the energy of the infalling gas is thermalized via shocks. How efficiently this happens depends on the microphysics of the intracluster medium (ICM) dominated by plasma with temperatures $10^7 - 10^8$ K. The ICM is permeated by weak, tangled magnetic fields, which makes its basic properties, such as its thermal conductivity and viscosity, difficult to model. To complicate the picture, many merging clusters host diffuse synchrotron radio halos, produced by ultra-relativistic electrons co-existing with the thermal ICM. These relativistic particles are believed to be re-accelerated by ICM turbulence. Turbulence also reorders and amplifies the ICM magnetic fields.

A critical, missing piece of this picture is the direct observation of gas motions, both streaming and turbulent. Turbulence should be sensitive to the ICM viscosity. By measuring ICM bulk velocities and turbulence, and comparing these data with detailed magnetohydrodynamic (MHD) simulations, we can hope to improve our understanding of the most important physical aspects of the ICM.

The brightest, nearest clusters, which provide the strongest signal and the finest spatial information, are natural early targets for these measurements. Observations toward the Perseus and Coma clusters, for example, will provide a first-ever detection of intracluster turbulence and constrain its power spectrum in a relatively relaxed cluster and in one that has experienced a recent merger, respectively (Sec. 2 and 5). Observations of nearby clusters harboring cold fronts, such as A3667, will provide further information on the plasma physics operating in intermediate stages of clusters growth.

These three clusters also exhibit (non-thermal) radio emission of various morphologies. While associated non-thermal X-ray emission has so far been elusive, the deep HXI observations made simultaneously with the SXS studies will provide new limits and will also map the hottest thermal components recently discovered in some clusters (Sec. 6).

Direct contributions to cosmology

Clusters are the largest virialized structures in the Universe, and are thus sensitive probes for cosmology including the nature of dark energy. The ability of clusters to constrain cosmology depends critically on the accuracy with which cluster masses can be determined. One of the most important techniques for measuring cluster masses uses X-ray observations and relies on the assumption that the ICM is in hydrostatic equilibrium. Any break of this key assumption, for example due to bulk or turbulent motions in the ICM, can thus lead to a bias in the cosmological constraints from X-ray clusters.

¹Coordinators of this section: M. Markevitch, T. Kitayama, S. W. Allen, K. Matsushita

SXS observations of bright, nearby ($z < 0.1$) clusters will place strong limits on deviations from hydrostatic equilibrium. Pressure contributions from gas motions will be measured to an accuracy of a few percent in apparently relaxed clusters such as A2029 (Sec. 4). While a substantial investment of the *ASTRO-H* observing time is required, measurements of turbulent and bulk motions up to radii $\sim r_{2500}^2$ for a sample of nearby relaxed clusters will contribute significantly to improved constraints on dark energy and other cosmological parameters.

High-resolution X-ray spectroscopy is also a unique tool for detecting the Warm-Hot Intergalactic Medium (WHIM), which is predicted to contain most of the cosmic baryons at low redshifts and which has eluded detection so far. Current searches are limited to absorption lines in the spectra of distant quasars. SXS offers a chance to detect the denser regions of WHIM in emission. Deep, well-selected pointings hold the potential to improve our understanding of the WHIM (Sec. 8).

Finally, the nature of dark matter is among the most important unresolved questions in all of science. Certain plausible warm dark matter candidates, such as a hypothetical sterile neutrino in the \sim keV mass range, are predicted to decay, emitting a line in the soft X-ray energy band. If present, SXS may detect such a line from the dark matter concentrations being observed for other purposes, e.g., in galaxy clusters and the Galactic Center (Sec. 9).

The physics of AGN feedback

Feedback from active galactic nuclei (AGN) plays an important role in galaxy formation, preventing runaway cooling in cluster cores and causing the largest, elliptical galaxies to appear ‘red and dead’. AGN inflate ‘bubbles’ filled with relativistic plasma, displacing the ambient X-ray gas and driving weak shocks, and dragging the coolest, lowest entropy material (the fuel for future star formation) up and out of galaxy and cluster centers. We outline a strategy for studying feedback in the bright Virgo and Perseus clusters, where ongoing feedback is observed in their central galaxies, M87 and NGC 1275, respectively (Sec. 2 and 3). For M87 in particular, high-resolution SXS spectra will reveal the dynamics and microphysics of AGN feedback, allowing us to map the line-of-sight velocity component of the gas uplifted by the AGN. The data should also allow us to measure turbulence induced by the rise of the radio bubbles and by AGN-driven shock fronts. In addition, SXS observations will robustly measure how AGN-driven gas motions spread metals produced in central galaxies out into the surrounding ICM.

The chemical composition of the ICM

The ICM provides a reservoir storing essentially all of the metals ever ejected from cluster galaxies. Measurements of metal abundances in the ICM therefore provide a unique insight into the history of star formation and the evolution of galaxies. Galaxies in clusters are mostly early-type and have a different chemical evolution history than the Milky Way. Most metals synthesized in cluster galaxies escape into the ICM, but the deep gravitational potential wells of clusters keep them locked within the virial radii.

The ICM is optically thin and in, or very close to, collisional ionization equilibrium, with heavy elements highly ionized. Therefore, spectral modeling of the ICM is relatively simple. With previous X-ray satellites, emission lines of highly abundant elements, such as O, Si, S and Fe in the ICM have been detected. *ASTRO-H* will be able to detect weaker lines from rare elements like Al, Na, Mn, and Cr from the brightest cluster cores. The abundances of various elements provide sensitive tests of the nature of the stellar population of the cluster galaxies and their IMF, as well as information about the physics of SN Ia explosions.

For bright clusters, the above study can be done using the same data sets as other science goals (Sec. 7). For example, due to its relatively low ICM temperature, the Virgo cluster will produce prominent lines below $E \sim 3$ keV, making it an ideal target for precise measurements of the abundances of elements from N to Al. The Perseus cluster is a target of choice for accurate abundance measurements of the iron-peak elements, Mn, Cr,

² r_{2500} is the radius within which the average cluster matter density is 2500 times the critical density of the Universe; about 20% of the virial radius. It is often chosen for cosmological tests because the X-ray emission is easily measurable and the hydrostatic equilibrium assumption is expected to hold there.

Fe and Ni. Measurements of the radial abundance profiles will also help us better understand the enrichment history of the ICM.

Organization of the paper

As indicated above, coordinated observations of a carefully selected sample of targets are crucial for maximizing the scientific outcome of the mission. Subsequent sections of this paper are thereby ordered as follows. We first focus on two representative objects, the Perseus cluster and the Virgo cluster in Sections 2 and 3, respectively; the former is the *brightest* extragalactic extended X-ray source, which yields the highest photon statistics essential for high-resolution spectroscopy, whereas the latter is the *nearest* galaxy cluster which enables us to zoom into the closest environments of the central AGN and associated feedback processes. Thereafter, we discuss each of key science topics more systematically for a sample of clusters. Section 4 presents a search for turbulence at larger radii in several relaxed clusters including A2029 and its implications on the mass measurements. Sections 5 and 6 explore the capabilities of SXS and HXI, respectively, for studying dynamics, turbulent power spectrum, and high energy processes in merging clusters such as Coma and A3667. The significance and prospects of elemental abundance measurements in a variety of clusters are summarized in Section 7. Finally, Sections 8 and 9 describe possible spectroscopic searches for missing baryons and dark matter, respectively.

2 Nature of Gas Motions in the X-ray Brightest Galaxy Cluster

Overview

The Perseus Cluster, being the X-ray brightest cluster in the sky, serves as a prime target for high-resolution spectroscopic studies by *ASTRO-H*. Previous observations of this system have led to a series of landmark discoveries and we expect *ASTRO-H* observations to do the same. *ASTRO-H* will reveal in unprecedented detail the nature of gas motions, and the thermodynamic and chemical structure of the ICM, which are critically important for understanding galaxy formation and for cosmological studies using clusters. A mosaic of observations sampling the cluster from the core to r_{2500} will provide the first constraints on the typical spatial scales and velocities of turbulent gas motions. The same data will simultaneously probe resonance scattering in the core, providing additional constraints on the anisotropy of gas motions. The results for Perseus will provide an essential benchmark for studies of more distant, relaxed clusters used for evolutionary studies and cosmological tests, and address directly the energy dissipation in cluster cores (crucial for keeping the balance between heating and cooling), the chemical composition of the ICM, and the bias in mass measurements due to turbulence and bulk motions.³

2.1 Background and Previous Studies

2.1.1 Gas motions in cool core clusters

To answer some of the most important questions regarding the formation and evolution of galaxies and clusters of galaxies requires detailed knowledge of the dynamics and physics of the hot, X-ray emitting ICM. Critical questions include: how do AGN and merger induced bulk motions, turbulent eddies, shocks and sound waves dissipate energy into the surrounding medium? How efficiently does mixing between the different gas phases occur? Answering these questions requires observational constraints on gas motions, viscosity, and thermal conduction.

Constraints on gas motions from the broadening of emission lines have so far only been obtained for the cooling cores of galaxy clusters with strongly centrally peaked surface brightness distributions, using the reflection grating spectrometers on board *XMM-Newton* (the best constraints on turbulent velocities are of the order of

³Coordinators of this section: N. Werner, S. W. Allen, T. Tamura

few hundred km s^{-1} ; Sanders et al., 2010, 2011; Sanders & Fabian, 2013). Because the *XMM-Newton* gratings operate as slitless spectrometers, spectral lines are broadened by the width of the spatial distribution of the emitting ion in the source and the results therefore have large systematic uncertainties. Observations of line broadening with *ASTRO-H*SXS will not suffer from these uncertainties and will therefore tightly constrain small scale (~ 25 kpc) gas motions to a level more than an order of magnitude more precise. Possible sources of small scale turbulence include AGN activity (turbulence induced in the wakes of rising bubbles) and the shear induced by gas sloshing. Observations of line shifts, on the other hand, will allow us to measure coherent bulk motions of the gas in the core of the cluster.

2.1.2 The Perseus Cluster

The Perseus Cluster is a massive, relatively relaxed system at a distance of only 68 Mpc ($z = 0.0179$). *ASTRO-H* observations of this target will provide benchmark measurements of turbulent and ordered motions in the hot X-ray emitting ICM, and of its thermal and chemical structure. *ASTRO-H* observations of the Perseus Cluster will inform studies of more distant systems, including those used for cosmological work.

Extended X-ray emission associated with the Perseus Cluster was discovered by the Uhuru satellite (Gursky et al., 1971; Forman et al., 1972) and this source has been studied extensively by all the subsequent X-ray missions. The cluster X-ray emission was found to be strongly peaked at the position of the brightest cluster galaxy NGC 1275 (Fabian et al., 1981), which harbors a powerful X-ray and radio bright active galactic nucleus (AGN). ROSAT images of the region around NGC 1275 revealed two ‘holes’ in the X-ray emission coincident with the radio lobes (Böhringer et al., 1993; McNamara et al., 1996; Churazov et al., 2000). These observations were critical in revealing how the radio bright jets emanating from the central AGN inflate bubbles in the surrounding ICM, displacing the thermal gas and heating the surrounding ICM. This AGN feedback mechanism is now one of the most vigorously discussed topics in astrophysics, with important implications for the physics of galaxy formation, galaxy clusters, and growth of supermassive black holes. More recent studies of the Perseus Cluster with *Chandra*, *XMM-Newton*, and *Suzaku* further revolutionized our understanding of AGN feedback and cluster physics. Observations of the bright cluster core with *Chandra* revealed a series of X-ray faint cavities inflated by the central AGN, as well as weak shocks and ripples (likely sound waves) being driven by expanding cavities. These shocks and sound waves can in principle heat the ICM isotropically. These data also showed a continuous uplift of cooler multi-phase gas in the wakes of the rising bubbles and ridges of high metallicity in the ICM (Fabian et al., 2000, 2003a,b; Sanders et al., 2004; Sanders & Fabian, 2007; Fabian et al., 2011).

Observations with *XMM-Newton* provided intriguing suggestions for a lack of resonance scattering in the Perseus Cluster core. If confirmed, this would indicate differential gas motions along our line-of-sight with a range of velocities of at least half of the sound speed (Churazov et al., 2004). If the inferred differential gas motions have the character of small scale turbulence then its dissipation could provide enough energy to compensate for the radiative cooling of the ICM. From the Fe-K line emission in spectra obtained by *Suzaku*, Tamura et al. (2014) placed constraints on bulk and turbulent motions, also finding hints of small bulk velocities ($< 300 \text{ km s}^{-1}$) at $2' - 4'$ west of the cluster center.

Extensive *Suzaku* observations of the Perseus Cluster, along 8 different azimuths out to beyond its virial radius, offer the most detailed X-ray observation of the ICM at large radii in any cluster to date, providing important information about cluster growth and the virialization of the ICM (Simionescu et al., 2011, 2012; Urban et al., 2014). The observations indicate that the sloshing/swirling ICM motions (preferentially along the east-west axis of the cluster) extend out to very large radii and suggest that the ICM in the outskirts may be clumpy.

Observations of the Perseus Cluster also provided significant advancements in the studies of the chemical enrichment of the ICM. Recent *Suzaku* observations e.g. provided, for the first time, significant detections of X-ray lines from the rare elements Cr and Mn in addition to other metals previously seen in galaxy clusters (Tamura et al., 2009), as well as evidence that the ICM is enriched homogeneously all the way out to the virial radius of the cluster (Werner et al., 2013).

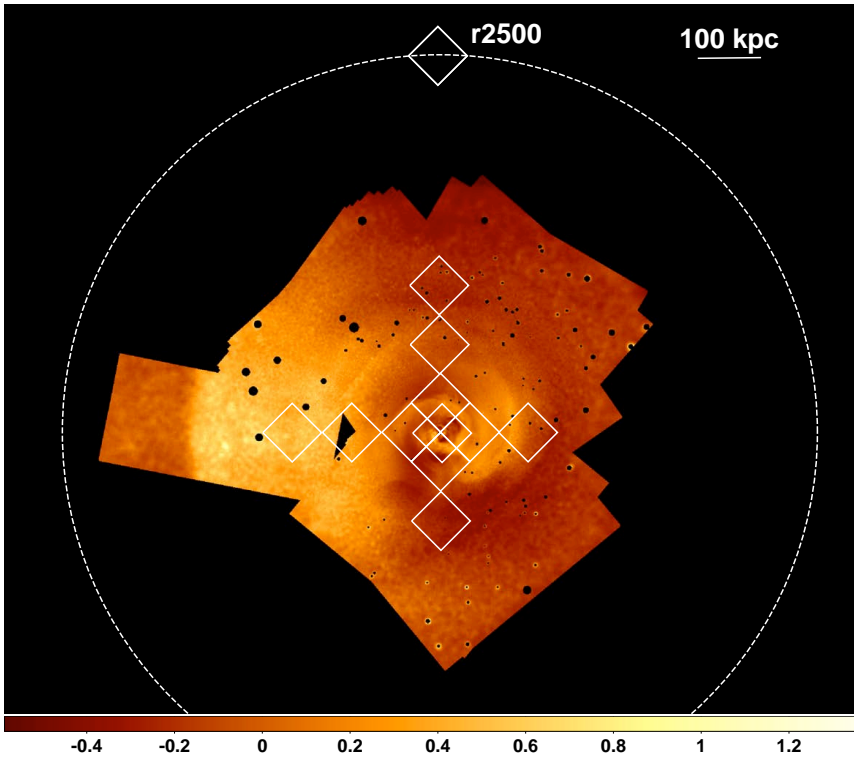


Figure 1: The pointing positions (boxes) over-plotted on the residual *Chandra* image of the cluster, from which a radially symmetric model has been subtracted in order to emphasize the substructure in the cluster core (Fabian et al., 2011). The color shows fractional variation in the X-ray surface brightness. We consider a deep pointing at the cluster core, four pointings centered at $r = 50$ kpc covering the central 130×130 kpc² (these pointings will partially overlap with the central pointing providing valuable information on systematics), four pointings at $r = 140$ kpc at approximately 90 degree azimuthal intervals, two pointings at $r = 240$ kpc to the north and east of the core, and a pointing at r_{2500} ($r = 600$ kpc) along the northern direction. The size of the boxes matches the $3' \times 3'$ field-of-view of SXS. For the five pointings spanning the central 130×130 kpc² and the pointings at $r = 140$ kpc, we will divide the field of view of the *ASTRO-H* SXS into four approximately independent regions, allowing us to study the projected physical properties of the ICM on a spatial scale of 1.5 arcmin. We will study the 1×1 arcmin region centered on the AGN independently.

2.2 Prospects and Strategy

The high X-ray brightness, proximity, and the relatively relaxed morphology make the Perseus Cluster an ideal target to study the dynamics and physics of the hot ICM. We examine the feasibility of a set of twelve pointings spanning a range of radii and azimuths. The surface brightness distribution of the Perseus Cluster is asymmetric due to mild ICM sloshing taking place primarily along the east-west major axis of the cluster (Simionescu et al., 2012), although the cluster is overall in a relatively relaxed configuration. This gas sloshing produces a prominent surface brightness discontinuity at $r \sim 100$ kpc to the west of the cluster center, and a strongly enhanced surface brightness extending all the way to $r \sim 650$ kpc to the east of the core. We consider an initial deep pointing at the cluster core, four pointings centered at $r = 50$ kpc covering the central 130×130 kpc (these pointings will partially overlap with the central pointing providing valuable information on systematics), four pointings at $r = 140$ kpc at approximately 90 degree azimuthal intervals, two pointings at $r = 240$ kpc to the north and east of the core, and a pointing at r_{2500} ($r = 600$ kpc) along the northern direction, which appears to be relatively undisturbed (see Figure 1).

2.2.1 The nature of gas motions

The high resolution *ASTRO-H* SXS spectra of the Perseus Cluster will reveal in unprecedented detail the nature of gas motions in the ICM. Pointed observations of the nucleus and selected locations out to r_{2500} will provide constraints on the typical spatial scales and velocities of turbulent gas motions. The same data will probe resonance scattering in the cluster core, providing additional constraints on the anisotropy of gas motions. Performing this study in the nearest, brightest, massive, relaxed system will provide a benchmark for *ASTRO-H* studies of more distant relaxed clusters used to probe cosmology, and address directly the energy dissipation

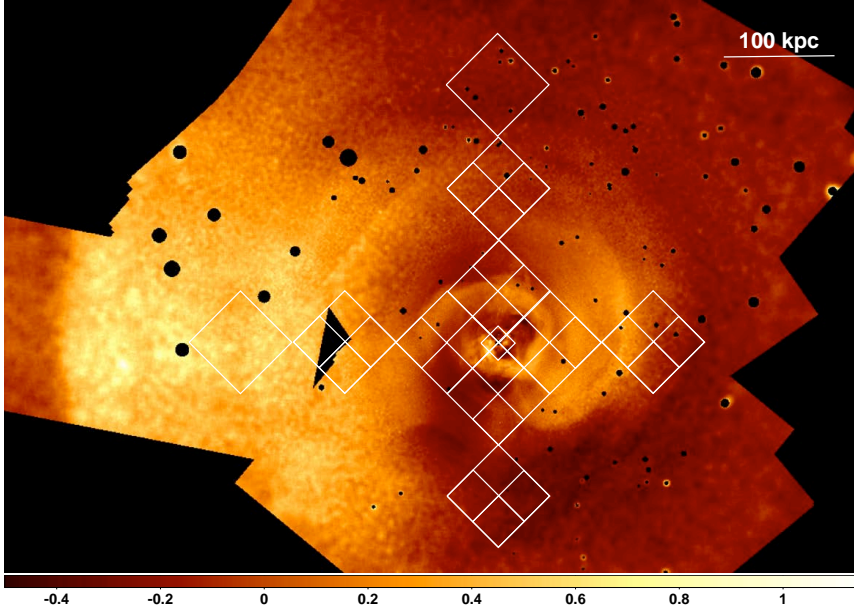


Figure 2: Same as Figure 1, but zoomed in on the pointing positions near the cluster core.

in cluster cores and the bias on cluster mass measurements due to turbulence (see Sec. 4 for details on the mass measurement bias).

The cluster core

The observations of the cluster core considered here involve nine separate pointings: the first (100 ks) targeted on the nucleus of NGC 1275 in the cluster core, four pointings (50 ks each) covering the central $130 \times 130 \text{ kpc}^2$, and four pointings (50 ks each) at approximately 90 degree azimuthal intervals, centered at a radius of $r = 140 \text{ kpc}$ from the cluster center (see Figure 2). For the five pointings spanning the central $130 \times 130 \text{ kpc}^2$ and the pointings at $r = 140 \text{ kpc}$, we will divide the field of view of the *ASTRO-H* SXs into four approximately independent regions, allowing us to study the projected physical properties of the ICM on a spatial scale of 1.5 arcmin. We will study the $1 \times 1 \text{ arcmin}$ region centered on the AGN independently. Goals for these observations include: detecting line broadening due to small scale turbulence; measuring ordered gas motions due to sloshing; obtaining independent constraints on differential gas motions from measurements of resonance scattering; measuring the temperature and chemical structure of the cluster core.

Line shifts and broadening

The pointing strategy mentioned above will enable a search for coherent gas motions due to sloshing that might be ‘rotational’ in nature - due to the swirling of the gas in the gravitational potential of the cluster. Such rotational motion can be clearly seen in the central region of the cluster (Figure 2). The western pointing of this set at $r = 140 \text{ kpc}$ probes a cold front previously identified in *XMM-Newton* and *Chandra* data (Churazov et al., 2003; Fabian et al., 2011) and will allow a search for a velocity shear underneath and across the surface brightness discontinuity. Such velocity shears are predicted by numerical simulations of gas sloshing and are expected to produce turbulence and (re)-accelerate relativistic electrons responsible for the observation of radio mini-halos (ZuHone et al., 2013). The bulk and turbulent velocities will be measured on each side of the cold front and compare the measurements with those obtained on the opposite side of the cluster. We will also search for turbulent and coherent gas motions in the wakes of the buoyantly rising bubbles along the north-south axis (the exact positions of the pointings in the cluster core may be adjusted to better cover interesting features seen

in the high resolution *Chandra* images).

Interpretation of the *ASTRO-H* data will benefit from the existing *Chandra* and *XMM-Newton* observations, which provide complementary information about the history of AGN outbursts producing turbulence. This will provide a more complete picture of how turbulence is driven and eventually dissipated.

Calibration between density and velocity fluctuations

Deep *Chandra* and *XMM-Newton* observations of the Perseus Cluster provide a probe of surface brightness and density fluctuations over a range of length scales. Detailed analysis of *Chandra* images shows that at radii 94–190 kpc, which are covered by four *ASTRO-H* pointings, the amplitude of density fluctuations $\delta\rho/\rho$ is $\sim 7.5\text{--}25\%$ on scales $\sim 14\text{--}90$ kpc (Zhuravleva et al., 2014b). Recently, it has been shown that the amplitudes of density and velocity fluctuations are expected to be approximately linearly related across a broad range of scales; analytical arguments predict a proportionality coefficient between density and velocity fluctuations of $\eta \sim 1$, while cosmological simulations of relaxed clusters show $\eta = 1 \pm 0.3$ (Zhuravleva et al., 2014). Taking $\eta = 1$, the characteristic amplitude of the one-component velocity is predicted to be $\sim 90\text{--}250$ km s⁻¹ on scales $\sim 14\text{--}90$ kpc (Zhuravleva et al., 2014b). Knowing the characteristic velocities on different scales, we can predict the expected line broadening (see equation E9 in Zhuravleva et al., 2012).

ASTRO-H observations will further allow us to directly measure the velocity broadening of emission lines and compare it to the values predicted based on the observed density fluctuations. In particular, the comparison of the predicted line broadening in a given radial range to the measured average value, determined over several pointings, should be useful for calibrating the statistical relation between the density and velocity fluctuations. Moreover, the comparison of the predicted line broadening in the individual pointings with the direct measurements will provide a clue to whether the perturbations driving the turbulence are local (on scales comparable to the field of view of *ASTRO-H*), or the turbulence is driven on larger scales.

Resonance scattering

Although the hot ICM is typically optically thin, at the energies of the strongest resonant transitions, the hot plasma in the dense central regions of galaxies and galaxy clusters can become optically thick (Gilfanov et al., 1987). The transition probabilities of strong resonance lines are large and, if the column density of the ion along a line-of-sight is sufficiently high, photons with the energies of these resonance lines will be absorbed and, within a short time interval, re-emitted in a different direction. Resonance scattering thus suppresses the line intensity in the cluster core and raises the line intensity at intermediate radii. Gilfanov et al. (1987) pointed out that since the optical depth in the core of a resonance line depends on the characteristic velocity of small-scale motion, its measurement gives important information about the turbulent velocities in the hot plasma. Measuring the level of resonance scattering in clusters is thus a good way to determine the characteristic velocity of small-scale turbulence independently of line broadening.

Churazov et al. (2004) used this technique to obtain constraints on differential velocities along our line-of-sight in the Perseus Cluster. They analyzed *XMM-Newton* EPIC data and compared the relative fluxes of the 1s2p and 1s3p He-like Fe lines in the core and in an annulus surrounding the core of the Perseus Cluster. The expected optical depth of the 1s2p Fe XXV resonance line at 6.7 keV is much larger than that of the 1s3p line at 7.9 keV, therefore the ratio provides information about the level of resonance scattering. Xu et al. (2002), Werner et al. (2009), and de Plaa et al. (2012) used the Fe XVII lines at 15Å and 17Å to measure the level of resonance scattering in giant ellipticals and groups of galaxies, placing interesting constraints on turbulence in those systems. High-resolution *ASTRO-H* SXS spectra will allow to search for and study resonance scattering using all of the lines in the available spectral band simultaneously.

Measurements of the suppression of spectral lines due to resonance scattering and their velocity broadening provide two independent, powerful probes of gas motions. These two diagnostics as a function of radius have a different dependence on the directionality of gas motions and therefore they allow us to reveal and place constraints on anisotropy of gas motions in bright cluster cores (Zhuravleva et al., 2011; Rebusco et al., 2008). Measurements of the shapes of strong spectral lines (Zhuravleva et al., 2011; Shang & Oh, 2012, 2013) could also be utilized as a third, independent probe of anisotropy.

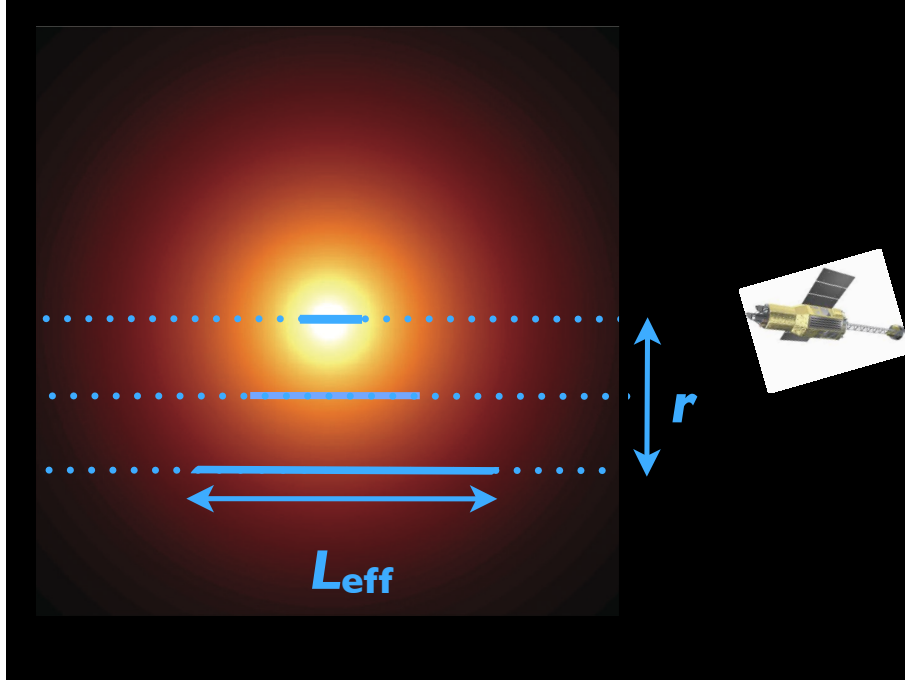


Figure 3: An illustration of how in a cluster with a centrally peaked surface brightness distribution, the projected radius r at which we observe determines the effective length, L_{eff} , from which the largest fraction of line flux (and measured line width) arises.

Measurements on intermediate scales

As a potential strategy, we consider two pointings at $r = 240$ kpc along the minor (northern) and major (eastern) axes, and a pointing at r_{2500} ($r = 600$ kpc) along the relatively undisturbed northern direction (Figure 1). Given the rapidly rising surface brightness profile in the core of the Perseus Cluster, the projected radius r at which we observe determines the effective length, L_{eff} , from which the largest fraction of line flux (and measured line width) arises (see Figure 3; Zhuravleva et al., 2012). This effective length increases as a function of radius. By measuring the width of spectral lines as a function of r , we therefore probe velocities on different spatial scales (L_{eff}). The increase of the effective length, L_{eff} , along the line-of-sight with growing projected distance r implies that larger and larger eddies contribute to the observed line broadening.

For gas motions on spatial scales $L < L_{\text{eff}}$ we expect to see significant line-of-sight velocity dispersions σ_v , resulting in line broadening, but no centroid shifts. The measured width of spectral lines as a function of projected radius $\sigma_v(r)$ therefore probes small scale motions. On the other hand, for gas motions on spatial scales $L > L_{\text{eff}}$, we expect to see significant centroid shifts. These measurements, in principle, provide the root-mean-square of the projected velocities V_{RMS} (see Zhuravleva et al., 2012). The observations on intermediate spatial scales will thus tell us whether the turbulent motions are predominantly small scale or large scale.

Since the projected velocity field mainly depends on large scale motions, while the line broadening is more sensitive to small scale motions, the ratio of the two is a good diagnostic of the shape of the power spectrum of the 3D velocity field. In particular: (i) the radial variations of the line broadening σ_v are closely related to the structure function of the velocity field; (ii) the ratio of the spatial variations of the mean velocity V_{RMS} to the radial variations of the line broadening can be used as a proxy of the velocity field injection scales; (iii) the map of measured line shifts due to large-scale motions can be converted straightforwardly into the power spectrum of the velocity field (Zhuravleva et al., 2012).

Even though it is unlikely that the turbulence follows a single power spectrum throughout the inner volume of the cluster, these observations will provide important constraints on the amplitude of gas velocities as a function of spatial scale and distance from the cluster center. The stratification of the cluster atmosphere, indicated by the radial gradient in the entropy distribution, may lead to an anisotropy in the turbulent velocity field, causing

the largest eddies to be predominantly tangential (on scales smaller than a few tens of kpc, the turbulence is expected to be isotropic). Because potential tangential motions will be probed relatively well by the offset pointings (due to our line-of-sight being parallel to the tangential direction), the large scale eddies should still be detected as a radial increase of the velocity broadening σ_v or shifts in the line centroid. A flattening of σ_v as a function of radius should constrain the largest scale at which turbulence is injected into the ICM inside of the given radius. The actual quality of observational constraints will depend strongly on the intrinsic properties of the velocity field (see Zhuravleva et al. 2012). The results will be interpreted in combination with tailored numerical simulations and the wealth of data obtained with the other X-ray missions.

The measurement at r_{2500}

The pointing at r_{2500} will provide a new benchmark measurement for cosmological studies with galaxy clusters. Measurements of the gas mass fraction, f_{gas} (the ratio of X-ray emitting gas mass to total mass) at intermediate radii in massive clusters provide a powerful tool for cosmology, enabling robust constraints to be placed on cosmological parameters including those describing dark energy (Allen et al., 2004, 2008; Mantz et al., 2014). The Perseus Cluster is the nearest massive cluster suitable for such work.

Recent work using *Chandra* X-ray observations (Mantz et al., 2014) has measured the intrinsic scatter in f_{gas} for a complete, rigorously selected sample of the most massive ($kT > 5$ keV), morphologically-relaxed galaxy clusters known. The measurements are made in an optimized spherical shell spanning radii $0.8-1.2r_{2500}$, finding a system-to-system scatter of $7.4 \pm 2.3\%$ (Mantz et al., 2014). This result places a firm upper limit on the cluster-to-cluster variation in turbulent pressure support at r_{2500} that can be present in massive, relaxed clusters. In a cosmological context, a key task for *ASTRO-H* is to determine the fraction of this scatter that is due to gas motions.

The pointing at r_{2500} in the Perseus Cluster will allow us to measure the line-of-sight velocity dispersion to a precision of ~ 50 km s⁻¹. Such a precision is well matched to probing the expected cluster-to-cluster scatter, which for a characteristic 1D velocity of isotropic turbulence of $v_{\text{turb}} = 300$ km s⁻¹ should be approximately ± 100 km s⁻¹ (68% confidence limit). We envisage that the r_{2500} measurement for Perseus will be among the first and (in the sense of mitigating systematics associated with the *ASTRO-H* PSF) most robust such measurements for an eventual ensemble of such data gathered for bright, nearby clusters over the first few years of the mission. Together these data will determine the average turbulent pressure support in clusters, providing a key reference point for cosmological studies.

The measurement at r_{2500} will complement the full set of observations for the northern arm (minor axis) providing reference measurements of gas velocities, thermodynamics and element abundances with a level of robustness that will be impossible for more distant systems. As discussed in detail in Section 4, r_{2500} is the largest radius out to which interesting measurements of these properties can be made with *ASTRO-H* in reasonable exposure times for local clusters.

2.2.2 Temperature structure and cooling

In addition to the electron temperature determined from the shape of the continuum, high resolution X-ray spectra obtained with the *ASTRO-H* SXS will yield the ionization temperature based on line ratios of He- and H-like ions. For the first time, the quality of the data will, in principle, be sufficient to directly measure the ion temperature of the ICM based on thermal line broadening.

Deep *Chandra* observations of the Perseus Cluster center (Sanders & Fabian, 2007) revealed multi-phase ICM spanning a range of temperatures between $kT = 0.5 - 8$ keV (see Figure 7). The spectral resolution of *ASTRO-H* SXS will allow us to study the ‘multi-phasedness’ of the ICM (the emission measure distribution as a function of temperature) and constrain the cooling rate as a function of location.

This effort will be helped by existing deep *Suzaku* and *XMM-Newton* data, which can be used to estimate the 3D deprojected thermodynamic properties of the ICM, and by *Chandra* data that provide the projected temperature distribution with a spatial resolution of a few arc-seconds. Joint multi-mission analysis of the data will be essential and will also help in constraining mixing and conduction between the different gas phases.

2.3 Targets and Feasibility

The observing strategy described above involves a combination of pointings at various radii and azimuths that will provide a powerful tool to study the gas motions in the hot ICM, and determine its temperature structure and chemical composition. The feasibility of the observations can be assessed using existing, deep *Chandra*, *Suzaku*, and *XMM-Newton* observations, from which we determine the input parameters for the assumed spectral models. For the energy response of the SXS we use the response files ‘ah_sxs_5ev_basefilt_20100712.rmf’ and ‘ah_sxs_7ev_basefilt_20090216.rmf’, which include the current best estimates with 5 eV and 7 eV constant energy resolutions (FWHM), respectively, using baseline filters. For the effective area, we use the file ‘sxt-s_100208_ts02um_of_flatsky-vig1kev_intallpxl.arf’. The effective area model assumes a sky with flat surface brightness and takes into account vignetting effects calculated at 1 keV. The flat sky ARFs available for the SXS are normalized so that the fitting results are provided per square degree, i.e. the true effective area has been multiplied by the field of view of the SXS in units of square degrees. To recover the true effective area we have thus multiplied the existing ARF by $1 \text{ deg}^2/3 \times 3 \text{ sq arcmin} = 400$. For the detector and cosmic X-ray background, we use the parameters provided in the files ‘sxs-bck.fits’ and ‘sxs-cxb.fits’⁴. For the central pointing and the four pointings covering the central 130×130 kpc, we use exposure times of 100 ks and 4×50 ks, respectively. For the four pointings at the radius $r = 140$ kpc, we use an exposure time of 4×50 ks. These observations should gather a sufficient number of X-ray photons to divide the field of view of the SXS into 4 approximately independent region and perform spectral analysis. For the pointings centered at radii of $r = 240$ kpc, we adopt exposure times of 80 ks and 50 ks to the X-ray fainter north and brighter east, respectively. For the pointing at $r = 600$ kpc (r_{2500}) we adopt an exposure time of 300 ks.

For our simulations, we use the SPEX spectral fitting package (Kaastra et al., 1996). We simulate absorbed thermal plasma models with model parameters determined from fitting *Suzaku* spectra extracted at the proposed pointing locations. To account for the AGN in NGC 1275, for the central pointing, we also include a power-law like emission component. We assume isotropic turbulence with a characteristic velocity of 300 km s^{-1} . Furthermore, we assume that the ion temperatures (and thus the thermal broadening of the lines) and their uncertainties are equal to the electron temperatures. We find that by fitting spectra extracted from the full field-of-view of the *ASTRO-H* SXS in the range of 0.3–10 keV, we will be able to measure model parameters with the statistical precisions shown in Table 1 and Table 2 for energy resolution of 5 eV and 7 eV, respectively. The precision of measurements in each of four regions will be approximately a factor of 2 lower. The quoted chemical abundances are with respect to the proto-Solar values of Lodders (2003). We note that the likelihood space is complex, with more than one local minimum. Therefore when working with real data from the satellite, Monte Carlo simulations will be needed to assess the statistical uncertainties robustly.

2.3.1 Dynamics of the intra-cluster medium

In bright, nearby galaxy clusters, such as the Perseus Cluster, *ASTRO-H* will determine the projected velocity v_{bulk} (line centroid) and the line-of-sight velocity dispersion σ_v (line width) as a function of position, providing a measure of the bulk and small scale velocities of the plasma. σ_v is essentially the 1D line-of-sight component of the characteristic velocity of isotropic turbulence, and in this white paper we define $v_{\text{turb}} = \sigma_v$. The observed width of a spectral line is $W_{\text{obs}} = \sqrt{W_{\text{inst}}^2 + W_{\text{therm}}^2 + W_{\text{turb}}^2}$, where W_{inst} is the instrumental line broadening (expected to have a FWHM of 5–7 eV), and $W_{\text{therm}} = 4.35 \text{ eV} \sqrt{kT/4 \text{ keV}}$ and $W_{\text{turb}} = 5.27 \text{ eV} (v_{\text{turb}}/100 \text{ km/s})$ denote the FWHM of the Fe XXV lines at 6.7 keV due to thermal broadening and isotropic turbulence, respectively (e.g. see Table 2 in Rebusco et al., 2008, and Appendix A).

Turbulent line broadening and bulk velocities

In our simulations, we assume turbulence with a characteristic velocity of $v_{\text{turb}} = 300 \text{ km s}^{-1}$. The principal constraints on v_{bulk} and v_{turb} are provided by the 6.7 keV Fe-K lines, which have the best combination of photon statistics and spectral resolution $\Delta E/E$. To illustrate the power of this spectral feature, in Table 1 and 2, we also

⁴*ASTRO-H* response files for spectral simulation can be downloaded from <http://astro-h.isas.jaxa.jp/researchers/sim/response.html>

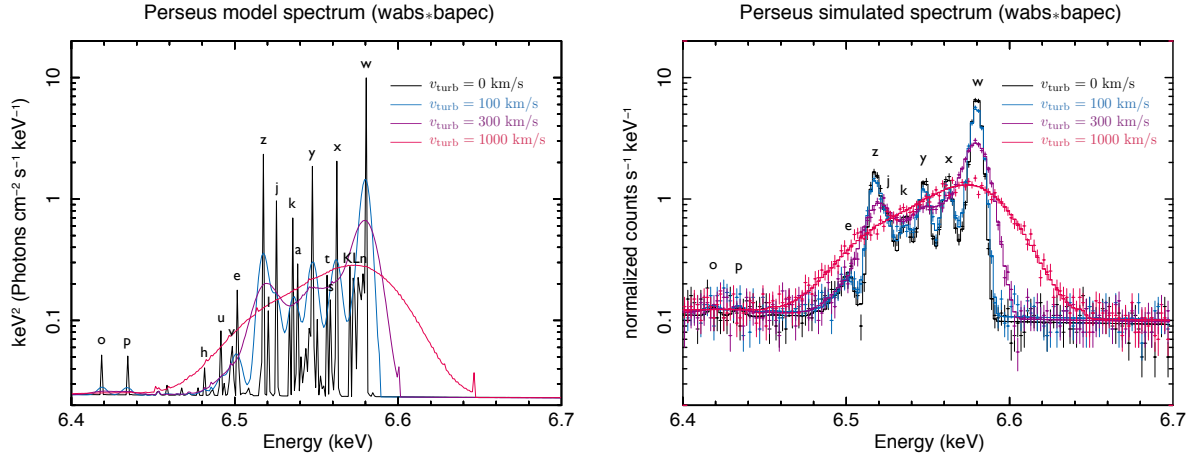


Figure 4: *Left:* Single temperature plasma model with parameters characteristic for the core of the Perseus Cluster at the redshifted He-like Fe-K line energies for different turbulent velocities. *Right:* Corresponding simulated *ASTRO-H*SXS spectra for a 100 ks observation. Representative lines are marked by letters as given in Gabriel (1972); e.g., the resonance line (w), the intercombination lines (x and y), and the forbidden line (z).

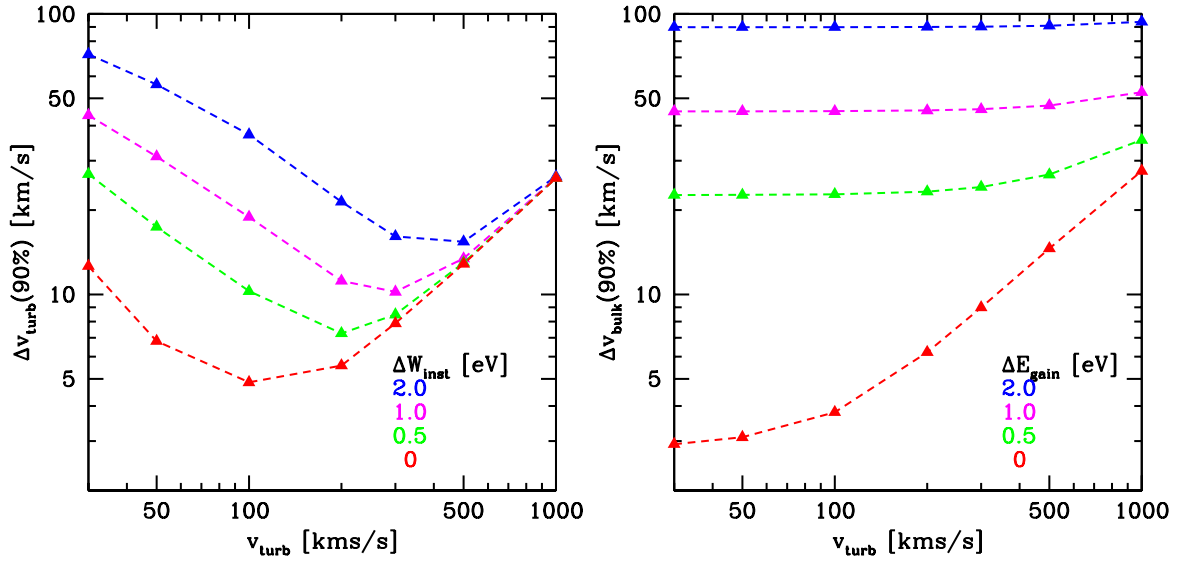


Figure 5: Uncertainties of the measured v_{turb} (left panel) and v_{bulk} (right panel) as a function of v_{turb} for different uncertainties in the FWHM of the line spread function and the gain. Note that the turbulent broadening adds to the observed line width in quadrature and its systematic error, to the first order approximation, is inversely proportional to the turbulent velocity. The simulation assumes 11,000 counts in the 6.7 keV Fe-K lines.

Table 1: Results of fits to simulated spectra assuming 5 eV resolution for *ASTRO-H* SXS. We assume spectra extracted from the full field-of view of the *ASTRO-H* SXS (dividing the field of view into four regions, the precision of our measurements will be a factor of ~ 2 lower) fitted in the 0.3–10 keV energy range. Y denotes the spectral normalization and kT_e the temperature of the thermal plasma model, v_{turb} and v_{bulk} are the turbulent and bulk velocities, respectively, the elemental abundances are given relative to the proto-Solar values by Lodders (2003), n_{POW} is the normalization and Γ is the index of the power-law like emission component of the central AGN. For the best fit bulk and turbulent velocities we also present the results obtained by fitting the 6.7 keV Fe-K lines alone. The number of continuum subtracted counts in the Fe-K lines was calculated assuming an effective area of 300 cm² at the observed line energy (6.47–6.62 keV). Statistical error bars are given at the $\Delta C=1$ level.

Pointing position	Center	$r = 50$ kpc	$r = 140$ kpc	$r = 240$ kpc	$r = 600$ kpc
Exposure time (ks)	100	50	50	80	300
Y (10^{65} cm ⁻³)	72.80 ± 0.09	64.00 ± 0.01	7.87 ± 0.04	2.63 ± 0.02	0.349 ± 0.003
kT_e (keV)	3.43 ± 0.01	4.04 ± 0.01	5.07 ± 0.05	5.54 ± 0.09	5.44 ± 0.12
v_{bulk} (km s ⁻¹)	± 3.7	± 5.4	± 19	± 32	± 54
v_{bulk} (km s ⁻¹) by Fe-K	± 6.2	± 7.9	± 23	± 37	± 66
v_{turb} (km s ⁻¹)	300 ± 3.9	300 ± 5.3	300 ± 15	300 ± 30	300^{+53}_{-45}
v_{turb} (km s ⁻¹) by Fe-K	300 ± 5.4	300 ± 6.8	300 ± 22	300 ± 35	300^{+61}_{-51}
numb. of phot. in Fe-K	14400	5800	600	250	100
O	0.65 ± 0.02	0.65 ± 0.02	0.5 ± 0.06	0.4 ± 0.10	0.3 ± 0.14
Ne	0.65 ± 0.02	0.65 ± 0.03	0.5 ± 0.07	0.4 ± 0.12	0.3 ± 0.16
Mg	0.65 ± 0.01	0.65 ± 0.02	0.5 ± 0.06	0.4 ± 0.09	0.3 ± 0.13
Si	0.65 ± 0.01	0.65 ± 0.01	0.5 ± 0.04	0.4 ± 0.06	0.3 ± 0.08
S	0.65 ± 0.01	0.65 ± 0.02	0.5 ± 0.05	0.4 ± 0.09	0.3 ± 0.11
Ar	0.65 ± 0.03	0.65 ± 0.04	0.5 ± 0.12	0.4 ± 0.20	0.3 ± 0.27
Ca	0.65 ± 0.03	0.65 ± 0.05	0.5 ± 0.13	0.4 ± 0.23	0.3 ± 0.30
Fe	0.65 ± 0.006	0.65 ± 0.007	0.5 ± 0.015	0.4 ± 0.02	0.3 ± 0.03
Ni	0.65 ± 0.03	0.65 ± 0.05	0.5 ± 0.14	0.4 ± 0.23	0.3 ± 0.30
$n_{\text{POW}} 10^7$	6.0 ± 0.02	-	-	-	-
Γ	1.72 ± 0.008	-	-	-	-

present the expected results for v_{bulk} and v_{turb} obtained by only fitting the Fe-K lines. The expected number of photons in the 6.7 keV Fe-K lines in the central pointing is ~ 14000 , allowing us to measure v_{bulk} and v_{turb} with statistical uncertainties of ~ 6 km s⁻¹ (for an illustration of the power of the Fe-K lines see Figure 4). For the off-center pointings (with the exception of the 300 ks pointing at r_{2500}), we aim to have at least 250 counts in the 6.7 keV Fe-K lines in each studied spatial region, and measure v_{bulk} and v_{turb} with statistical uncertainties smaller than 40 km s⁻¹. The 300 ks pointing at r_{2500} will yield ~ 100 counts in the 6.7 keV lines. As described in Section 4, observations of brightest, relaxed galaxy clusters, will provide accurate constraints on turbulent pressure near r_{2500} for each object. An ensemble of these observations will together provide a robust measurement of the average turbulent pressure support.

Degrading the energy resolution from 5 eV to 7eV, assuming $v_{\text{turb}} = 300$ km s⁻¹, the precision of the line broadening measurement decreases by about 10–20%. For smaller v_{turb} , the degradation of energy resolution will result in larger decrease in the precision of the line broadening measurements (e.g. for $v_{\text{turb}} = 140$ km s⁻¹ degrading the energy resolution from 5 eV to 7 eV will result in a $\sim 40\%$ increase in Δv_{turb}). Even though numerical simulations predict $v_{\text{turb}} \sim 300$ km s⁻¹, little is known about the actual turbulence in clusters. The existence of long filaments of cold/cool gas in the Perseus Cluster indicates that at certain locations the turbulent velocities may be as low as 100 km s⁻¹ (Fabian et al., 2011). With 250 counts in the 6.7 keV Fe-K lines, and 7eV energy resolution, we will still be able to measure $v_{\text{turb}} = 100 \pm 30$ km s⁻¹.

In deep observations, systematic errors due to uncertainties in the gain and line-spread-function calibration are also expected to be significant (for a more detailed discussion on the calculation and impact of systematics see Appendix A). Figure 5 shows the combined statistical + systematic uncertainties in v_{turb} (left panel) and

Table 2: Results for the same simulations as in Table 1, assuming 7 eV resolution for *ASTRO-H*SXS.

Pointing position	Center	$r = 50$ kpc	$r = 140$ kpc	$r = 240$ kpc	$r = 600$ kpc
Exposure time (ks)	100	50	50	80	300
Y (10^{65} cm $^{-3}$)	72.80 ± 0.09	64.00 ± 0.01	7.87 ± 0.04	2.63 ± 0.02	0.349 ± 0.003
kT_e (keV)	3.43 ± 0.01	4.04 ± 0.01	5.07 ± 0.05	5.54 ± 0.09	5.44 ± 0.12
v_{bulk} (km s $^{-1}$)	± 4.4	± 6.3	± 22	± 32	± 57
v_{bulk} (km s $^{-1}$) by Fe-K	± 6.6	± 8.5	± 31	± 40	± 65
v_{turb} (km s $^{-1}$)	300 ± 4.8	300 ± 6.3	300 ± 21	300 ± 33	300^{+59}_{-50}
v_{turb} (km s $^{-1}$) by Fe-K	300 ± 5.9	300 ± 7.5	300 ± 23	300 ± 37	300^{+66}_{-56}
numb. of phot. in Fe-K	14400	5800	600	250	100
O	0.65 ± 0.02	0.65 ± 0.02	0.5 ± 0.07	0.4 ± 0.10	0.3 ± 0.14
Ne	0.65 ± 0.02	0.65 ± 0.03	0.5 ± 0.09	0.4 ± 0.13	0.3 ± 0.17
Mg	0.65 ± 0.01	0.65 ± 0.02	0.5 ± 0.07	0.4 ± 0.10	0.3 ± 0.13
Si	0.65 ± 0.01	0.65 ± 0.01	0.5 ± 0.05	0.4 ± 0.07	0.3 ± 0.08
S	0.65 ± 0.01	0.65 ± 0.02	0.5 ± 0.06	0.4 ± 0.09	0.3 ± 0.11
Ar	0.65 ± 0.03	0.65 ± 0.04	0.5 ± 0.14	0.4 ± 0.21	0.3 ± 0.27
Ca	0.65 ± 0.03	0.65 ± 0.05	0.5 ± 0.16	0.4 ± 0.23	0.3 ± 0.31
Fe	0.65 ± 0.008	0.65 ± 0.007	0.5 ± 0.02	0.4 ± 0.02	0.3 ± 0.03
Ni	0.65 ± 0.04	0.65 ± 0.05	0.5 ± 0.17	0.4 ± 0.24	0.3 ± 0.31
$n_{\text{POW}} 10^7$	6.0 ± 0.02	-	-	-	-
Γ	1.72 ± 0.007	-	-	-	-

v_{bulk} (right panel) as a function of v_{turb} for different systematic uncertainties in the FWHM of the line-spread-function and the gain. The systematic uncertainties in the measured velocity broadening are sensitive to the line spread function calibration, which is expected to be better than 1.6 eV in FWHM. The uncertainties in the measured v_{bulk} will be sensitive to the gain calibration: for example a gain calibration systematic error of 1 eV, implies a systematic uncertainty $\Delta v_{\text{bulk}} \sim 50$ km s $^{-1}$. The uncertainty on the gain calibration is expected to be smaller than 2 eV.

The systematic errors above are assumed to be uncorrelated. This is a highly pessimistic assumption. In practice the different pixels are expected to have correlated systematic errors, and observations taken within a short period of time are expected to be affected by systematics in a similar way. Such correlations will decrease the impact of systematic uncertainties on some measurements (e.g. line broadening) and can be marginalized over using standard Monte Carlo methods.

Resonance scattering

In rich, massive, X-ray bright galaxy clusters resonance scattering is expected to be particularly important for the He-like Fe line (1s2p) at 6.7 keV. In the past, its effects were studied by comparing the flux from this line with the flux of the nearby He-like Fe line (1s3p) at 7.9 keV (Churazov et al., 2004). With the spectral resolution of CCD type detectors, however, the 7.9 keV Fe line is blended with the He-like Ni line at 7.8 keV, which made the interpretation of results difficult and ambiguous.

The much improved spectral resolution of the *ASTRO-H*SXS (30 times better than the energy resolution of the current X-ray CCDs around the 6.7 keV line), and new modeling and data analysis techniques that look for resonance scattering in all resonant lines simultaneously (e.g. Zhuravleva et al., 2013), will allow us to use resonance scattering in the Perseus Cluster to obtain meaningful constraints on turbulence.

Figure 6 shows the expected effects of resonance scattering on the 6.7 keV He-like Fe-K line in the ICM for the central *ASTRO-H* pointing, assuming isotropic turbulence with a characteristic line-of-sight velocity of $v_{\text{turb}} = 360$ km s $^{-1}$, corresponding to the Mach number $M_{1D} \equiv v_{\text{turb}}/c_s = 0.35$, where c_s is the sound speed.

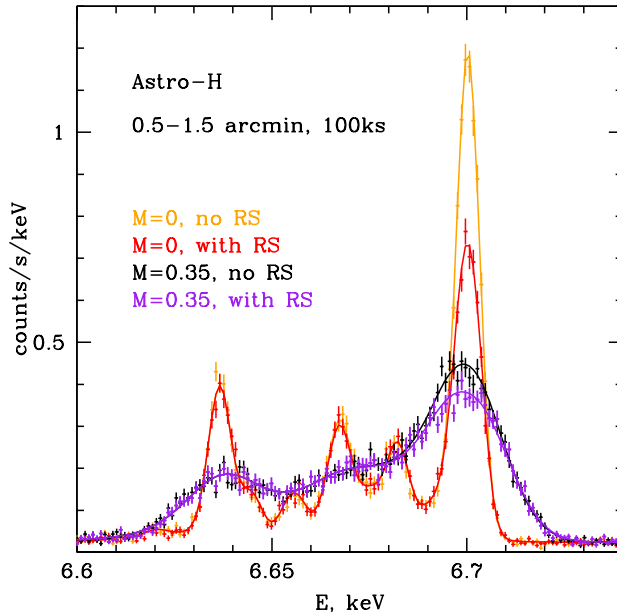


Figure 6: Simulated Fe lines from the Perseus core affected by resonance scattering (RS) for different turbulent velocities as a function of rest-frame energies. The spectrum from the 100 ks central pointing excludes the central 1×1 arcmin region, where the contribution of the central AGN is dominating the signal. Notice, that using a 100 ks *ASTRO-H* observation, we will be able to use the suppression of the resonance line to measure even relatively high line-of-sight turbulent velocity of $v_{\text{turb}} = 360 \text{ km s}^{-1}$, corresponding to the Mach number $M_{\text{ID}} = 0.35$ for $kT = 4 \text{ keV}$.

The effects of resonance scattering were calculated assuming a cluster atmosphere model (3D distributions of density, temperature, and metallicity) derived from spherically symmetric models fitted to *XMM-Newton* and *Chandra* data (Zhuravleva et al. 2013).

2.3.2 The temperature structure of the ICM

Ion kinetic temperature

Current X-ray detectors can only measure the temperature of the electrons in the ICM (from the bremsstrahlung continuum and line ratios). The electron ion thermal equilibration time-scales in the central regions of galaxy clusters are small, and we expect the ion temperatures to equal the electron temperatures. By measuring the thermal line broadening, deep observations of the core of the Perseus Cluster with the *ASTRO-H* SXIS may in principle verify this expectation and measure the ion temperature independently of the electron temperature of the plasma.

Based on a single line profile, however, thermal line broadening cannot be separated from broadening due to turbulence. Because $W_{\text{therm}} \propto E_0 \sqrt{kT_e/m_{\text{ion}}}$ (where E_0 is the line energy and m_{ion} is the ion mass), constraints on the ion temperature require simultaneous measurement of the broadening of lines from different ions with a large range of ion mass⁵. Under the simplifying assumptions of a single-temperature plasma of a single characteristic velocity of isotropic turbulence of $v_{\text{turb}} = 141 \text{ km s}^{-1}$, we simulated *ASTRO-H* SXIS spectra for a 100 ks observation of the core of the Perseus Cluster. Fitting for the ion temperature simultaneously with the other free parameters (see the parameters in Table 1 and 2) allows us to measure kT_{ion} with statistical uncertainties of $kT_{\text{ion}} = 3.43 \pm 0.49 \text{ keV}$. If the turbulence is stronger, with a characteristic velocity of $v_{\text{turb}} =$

⁵We note that the thermal broadening of low mass ions observed at lower energies is small. E.g. the thermal widths for O VIII (0.6 keV), Mg XII (1.47 keV), Si XIV (2.01 keV), and Fe XXV (6.70 keV) are 0.79 eV, 1.46 eV, 1.84 eV, and 4.35 eV, respectively.

300 km s^{-1} , the constraints on the ion temperature will be significantly weaker $kT_{\text{ion}} = 3.43_{-0.8}^{+1.7} \text{ keV}$.

We note, however, that because the plasma in the cluster core is not single-temperature, and the gas motions in the cluster core can most likely not be characterized by isotropic turbulence with a single characteristic velocity, the measurements of the ion kinetic temperature will have significant systematic uncertainties.

Multi-temperature structure and cooling

For central pointings we assume an absorbed multi-temperature plasma model, the input parameters for which were determined using 2D multi-temperature spectral maps produced by fitting deep *Chandra* data of the core of the Perseus Cluster (see Figure 7, Sanders & Fabian, 2007). Cooling X-ray emitting gas (with $kT \lesssim 0.9 \text{ keV}$) in the cluster center will be identified based on the spectral lines of Fe XVII and potentially by the presence of the O VII lines ($kT \lesssim 0.35 \text{ keV}$). While the Fe XVII lines have been detected in a number of cooling core clusters, including the Perseus Cluster, the O VII lines have never been seen in any individual system - O VII has only been detected in the stacked archival RGS data of the coolest groups, clusters, and giant elliptical galaxies (Sanders & Fabian, 2011).

Unfortunately, due to its decreased energy resolution ($\Delta E/E$) below 1 keV and a smaller effective area, *ASTRO-H* SX/S is not expected to be significantly better at detecting cooling in cluster cores than *XMM-Newton* RGS. The $\sim 0.5 \text{ keV}$ phase that has been detected in the core of the Perseus Cluster with *XMM-Newton* RGS and spatially mapped with *Chandra* will be detected with *ASTRO-H* SX/S at 6.1σ significance (assuming an exposure of 100 ks). An important advantage, however, with respect to *XMM-Newton* RGS is that *ASTRO-H* SX/S will be providing high resolution spectra in well defined regions, also outside of the bright cluster core.

Furthermore, deep *ASTRO-H* observations of the Perseus Cluster may be used to search for departures from simple thermal Maxwellian electron distributions in the ICM. Non-thermal electrons, producing high-energy tails to the thermal Maxwellian electron distributions, may be accelerated in weak MHD shocks. The presence of such non-Maxwellian tails may be revealed by looking at the di-electronic satellite lines in the Fe-K band (see Kaastra et al., 2009).

Multi-mission data analysis techniques

The combination of high resolution spectra from *ASTRO-H* SX/S and detailed 2D spectral information (with thousands of independent spatial bins in each of which we determine emission measure, temperature, metallicity, pressure, entropy) obtained in very deep observations with *Chandra* and *XMM-Newton*, will provide a powerful tool to study the 3D thermal properties of the ICM. While the detailed spatially resolved spectral maps provide key information on the projected 2D temperature distribution, fitting multi-temperature differential emission measure models to high quality *ASTRO-H* spectra will reveal the temperature structure along the line-of-sight.

2.3.3 Chemical abundance measurements

As shown in Table 1 and 2 we will be able to accurately measure the chemical abundances of O, Ne, Mg, Si, S, Ar, Ca, Fe, and Ni. The systematic uncertainties on the abundances will be reduced by the dramatically improved spectral resolution of *ASTRO-H* SX/S. Furthermore, the observations of this X-ray brightest galaxy cluster will also permit measurement of the abundances of rare elements such as Na, Cl, Al, Cr, and Mn. The 100 ks pointing on the cluster core will allow us to measure the abundances of Cr, Mn, and Al at a better than 5σ significance, and the abundance of Na and Cl with a significance better than 3σ (see Sec. 7 for details). We will not be able to measure the abundance of N.

2.3.4 The AGN emission

The AGN emission of NGC 1275 has been studied in detail at all wavelengths from radio to gamma rays all the way up to GeV energies. However, detailed information in hard X-rays is relatively scant. The data obtained

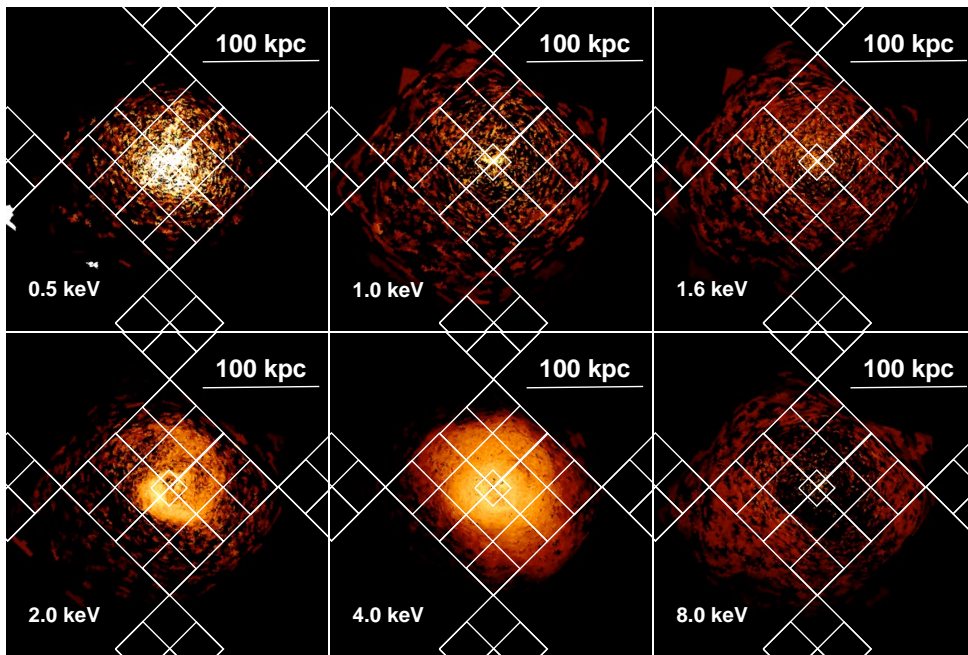


Figure 7: Results from a multi-temperature fit to the *Chandra* data of the core of the Perseus Cluster. The images show the emission measure per unit area of the different temperature components with the central *ASTRO-H* pointing over-plotted. From Sanders & Fabian (2007).

by the Hard X-ray Imager (HXI) on *ASTRO-H* will allow us to study the spectral properties of the AGN and its time variability up to energies of several tens of keV.

2.3.5 Diffuse non-thermal emission

The broad band X-ray data of the Perseus Cluster obtained with the wide array of instruments on board *ASTRO-H*, including the SXS, SXI, and the HXI will also be used to search for non-thermal and very hot thermal emission (e.g. Ota et al., 2008). The hard X-ray data obtained in the long exposures in combination with careful spectral modeling in the soft X-rays will provide good constraints on diffuse hard X-ray emission above the thermal emission (see Sec. 6 for more details).

2.4 Remarks on sources of systematic uncertainty

The Perseus Cluster, like all relaxed galaxy clusters, has a very peaked surface brightness distribution and the amount of light scattered from the bright cluster core into the off-center pointings will need to be carefully evaluated (though the proximity of the target minimizes these concerns to the fullest extent possible). Based on the currently available simple azimuthally symmetric point-spread-function (PSF) model, in the radial range of 10–40 arcmin the expected ratio of scattered light to signal is negligible. This means that our pointings planned at $r = 240$ kpc and at $r = 600$ kpc will not be affected by scattered light contamination. For the pointings at $r \sim 140$ kpc, however, the preliminary, azimuthally symmetric PSF model predicts that up to 20% of the photons will be scattered from the outside of the SXS field of view. However, according to our current understanding of the *ASTRO-H* mirrors, the amount of light scattered from certain directions will be minimal - just like with the *Suzaku* mirrors - and we may be able to reduce the contamination by observing with one of the detector corners pointing towards the bright cluster center (this is the configuration shown in Figs 1 and 2). The exact strategy for minimizing scattered light contamination when observing the vicinity of the bright cluster core will need to be further explored once the Soft X-ray Telescope calibration files for the ray tracing simulator become available.

The analysis of data from individual $1.5' \times 1.5'$ resolution elements will be challenging. With a half-power-diameter (HPD) for the PSF of $1.3'$, such square shaped regions will contain only about 60% of the flux from the corresponding region on the sky - the rest of the photons will be scattered out into the surrounding regions (this is an estimate assuming a point source and even more photons will be scattered out for a source with an extended surface brightness distribution). In the same time photons from the surrounding regions will be scattered into the region of interest. Spatially resolving the velocity structure of the gas in the five pointings spanning the central 130×130 kpc² or in the surrounding pointings at $r = 140$ kpc will therefore require an excellent understanding of the shape of the telescope PSF.

Finally, in order to take full advantage of the progress in X-ray instrumentation, innovation in the spectroscopic codes used for fitting the observed spectra will also be crucial. Updates in the ionization balance, implementation of a more extensive set of atomic parameters for Fe and Ni L-shell lines, and inclusion of rare elements that are currently not implemented in spectral fitting packages will be important. These updates will benefit the whole astrophysics community.

3 A Detailed View of AGN Feedback

Overview

Active galactic nuclei (AGN) are the heating engines responsible for preventing a cooling catastrophe in cluster cores. AGN inflate bubbles filled with relativistic plasma which displace the ICM, drive weak shocks, and drag filaments of cool gas out of cluster centers. One of the best targets for studying AGN-ICM interaction is M87, the central dominant galaxy of the Virgo Cluster. High-resolution SXS spectra for this target will reveal the dynamics and microphysics of AGN feedback, allowing us to map the line-of-sight velocity component

of the gas in the X-ray bright arms uplifted by the AGN, and measure the turbulence induced by the rise of the radio bubbles and by the outer shock front. We will place reliable constraints on the multi-phase structure and distribution of cool gas in the cluster core, and accurately measure the metallicity of the uplifted gas independently from that of the surrounding ICM, robustly determining how gas motions induced by the AGN spread out metals produced in the central galaxy. ⁶

3.1 Background and Previous Studies

3.1.1 The cooling flow problem and the necessity for AGN feedback

If the energy radiated away at the centers of so-called ‘cool-core’ clusters of galaxies, which show sharp X-ray surface brightness peaks and central temperature dips, came only from the thermal energy of the hot, diffuse ICM, the ICM would cool and form stars at rates orders of magnitude above what the observations suggest (see Peterson & Fabian, 2006, for a review). It is currently believed that the energy which offsets the cooling is provided primarily by interactions between active galactic nuclei (AGN) in the central dominant galaxies of these clusters and the surrounding ICM (e.g. Churazov et al., 2000, 2001; McNamara & Nulsen, 2007). Through a tight feedback loop, it is thought that the AGN can provide the right amount of energy to prevent catastrophic cooling and stem star formation.

Generally speaking, there are three main mechanisms by which the AGN-ICM interactions take place. Cluster AGN have been observed to: 1) drive weak shocks into the intracluster plasma, 2) inflate bubbles filled with relativistic plasma, which then rise buoyantly, and 3) drag filaments of cool gas out of cluster centers, in the wakes of the buoyantly rising bubbles. It is not yet clear what determines the fraction of the total energy imparted by the AGN that goes into each of these three processes (Vernaleo & Reynolds, 2007; Mendygral et al., 2011), nor do we understand in detail how the energy associated with AGN-injected bubbles and uplifted gas filaments eventually dissipates into heat.

While AGN-inflated bubbles and weak shocks are clearly seen in the innermost regions of the Perseus Cluster (e.g. Böhringer et al., 1993; Fabian et al., 2006), the cool gas filaments uplifted by the radio lobes in this system are very faint in comparison with the rest of the ICM (e.g. Sanders & Fabian, 2007), and the features related to the AGN feedback process will be difficult to resolve spatially with *ASTRO-H*. The core of M87 in the nearby Virgo Cluster therefore presents an ideal target for a more detailed look at the dynamics of AGN-ICM interaction.

3.1.2 Previous observations of AGN feedback in M87

The Virgo Cluster is the nearest galaxy cluster to us (~ 16.7 Mpc), which allows us to resolve phenomena with exceptional spatial resolution. Its central galaxy, M87 is among the brightest extragalactic X-ray sources in the sky, providing a guarantee of excellent photon statistics and accurate temperature and metal abundance determinations. M87 is one of the best studied galaxies in the Universe and its central region has been the target of very deep observations with *XMM-Newton*, *Chandra*, *Suzaku*, and an array of multiwavelength facilities.

The hot gas atmosphere of M87 shows striking signs of AGN-ICM interaction, including an AGN-driven classical shock (Forman et al., 2005, 2007; Simionescu et al., 2007; Million et al., 2010), X-ray cavities (Forman et al., 2005, 2007; Million et al., 2010), and clear enhancements in X-ray surface brightness associated with the main radio lobes to the east and southwest of the core (Feigelson et al., 1987; Böhringer et al., 1995; Belsole et al., 2001; Young et al., 2002; Forman et al., 2005, 2007; Werner et al., 2010). Initial *XMM-Newton* observations showed that multi-temperature models including cool gas components were needed to describe the spectra of these regions, known as the E and SW X-ray arms (Belsole et al., 2001; Molendi, 2002).

With deeper *XMM-Newton* data, a correlation was found between the amount of cool gas and the metallicity in different regions along the arms, leading to the indirect conclusion (Simionescu et al., 2008) that the cool, metal-rich gas is uplifted by the AGN from the central parts of the galaxy (following the scenario proposed by Churazov et al., 2001) where metals are being produced by supernova explosions and stellar winds. Werner et al.

⁶Coordinators of this section: A. Simionescu, K. Matsushita

(2010) showed that the mass of gas in the arms is comparable to the gas mass in the approximately spherically symmetric 3.8 kpc core, demonstrating that the AGN has a profound effect on its immediate surroundings, effectively removing gas from the cluster center that would otherwise cool and form stars.

The energetics and metal-transport mechanisms associated with the AGN activity in the central parts of M87 have therefore been the focus of much previous work, which has yielded important information about the physics of the AGN-ICM interaction.

3.2 Prospects and Strategy

As discussed above, the uplifted gas in the X-ray bright arms, as well as in the core of M87, is multi-phase. Modeling the exact distribution of the temperature phases with low-resolution CCD spectra is very difficult and possibly subject to fitting biases. *XMM-Newton* RGS data have proven extremely useful for understanding the thermal state of the X-ray gas in the core of the galaxy and constraining the rate at which gas may be cooling out of the X-ray band (below 0.5 keV, which is currently the lowest temperature detected in the M87 halo; Werner et al., 2006). However, the extended nature of the X-ray bright arms has so far prevented high spectral resolution measurements of the properties of the uplifted gas with slitless grating spectrometers. These measurements are now enabled by the *ASTRO-H* SXS, and will be pivotal for furthering our understanding of AGN feedback physics.

3.2.1 Dynamics of gas uplift

From several arguments based on *Hubble Space Telescope* observations of the superluminal motion in the jet of M87 (Biretta et al., 1999) as well as the geometry and degree of polarization of the large-scale radio lobes, it is likely that the arms are oriented at a relatively small angle with respect to the line of sight (Werner et al., 2010, estimate this angle to be at most 35°), and therefore the *ASTRO-H* SXS should allow us for the first time to measure the line-of-sight velocity of the low-entropy gas in the arms. Detecting this outward motion of the cool X-ray gas will provide the first direct proof for the scenario that the X-ray bright arms indeed originate from gas uplift by the AGN. These observations will moreover provide an estimate for the kinetic energy of the uplift, which remains one of the main uncertainties in determining the total energy associated with the AGN feedback.

3.2.2 AGN-induced metal transport

With lower-resolution spectra, it has so far not been possible to directly measure the metallicity of the uplifted gas independently of that of the hot ambient gas. When multi-temperature fits were performed, usually the abundances of the several phases had to be coupled to each other in order for the fit to be constrained. However, Simionescu et al. (2008) found a correlation between the amount of cool gas in a given spectral extraction region and the average metallicity of that region, which lead to the conclusion that the abundance of the cool gas must be roughly twice higher than that of the hot 2 keV phase. This is expected if the uplifted cool gas was dragged by the buoyantly rising radio lobes of the AGN from the cluster center, which is more metal-rich due to contributions from stellar winds and supernovae in M87.

The abundance of the cool gas is a very important quantity for several reasons. Firstly, the emission from this cool 1 keV gas consists mainly of line emission; therefore, the metallicity and spectral normalization typically anticorrelate in low-resolution spectra, and in order to obtain an accurate estimate of the true emission measure, density, and mass of the uplifted cool gas, it is important to measure its metallicity and break this degeneracy. Secondly, the metallicity of the cool gas is important in order to understand the effect of the AGN on transporting metals produced by stars and supernovae in the central galaxy into the ICM. The distribution of metals in the centers of cool-core clusters of galaxies is much more broadly peaked than the distribution of optical light; if the stars produce the metals, then we must understand how the metals are spread out. Rebusco et al. (2006) propose that AGN-ICM interaction plays a dominant role in this process, a role which can be quantitatively investigated for the first time using the proposed observations.

As we show in the next section, *ASTRO-H* will enable us to make the first accurate direct determination of the metallicity of the cool uplifted gas, and therefore measure the total gas mass and the mass of each metal that is being transported by the AGN in M87, and potentially test whether the chemical composition of the uplifted gas is different from that of the ambient gas at larger radii.

While M87 is the best system to study AGN-induced metal transport in detail, this phenomenon is widespread in cluster cores. Columns of relatively cool, metal-enriched gas lying along the edges of radio sources and X-ray cavities have been identified at the centers of other clusters and groups (e.g. Hydra A, Simionescu et al., 2009; Kirkpatrick et al., 2011), and the radial ranges of the metal-enriched outflows are found to correlate well with the jet power (Kirkpatrick et al., 2011). Therefore our study of M87 will answer questions that are relevant to understanding AGN feedback in general, and will serve as a pathfinder for future observations of AGN-induced metal transport in other systems.

3.2.3 Turbulent motions in the hot ICM

With the observing strategy considered here, we will spatially map the turbulence in the hot gas. With the excellent statistics offered by this nearby, bright target, we will be able to take advantage of the *spatial* resolution of the SXS, and measure the turbulent line broadening in 4–9 independent resolution elements, or “spaxels”,⁷ per pointing (see Section 3.4 for the discussion of PSF scattering affecting the independence of such neighboring regions). This will allow us to compare, with high precision, the turbulent velocities:

- in the cluster core, in the immediate vicinity of the AGN which is constantly injecting turbulence into the ICM;
- within and immediately adjacent to the X-ray bright arms, where the gas uplift by the buoyant radio lobes is driving the turbulence;
- in a separate offset pointing targeting a more relaxed region far away from the direction of the uplift;
- immediately inside and outside the AGN-driven shock at a radius of 3 arcmin. While classical shocks are not expected to induce turbulence in the ICM, the SW arm appears very narrow inside the 3 arcmin shock front and suddenly broadens beyond this radius (e.g. Werner et al., 2010). These observations will therefore help to elucidate the interplay between AGN uplift and shock dynamics in this region.

This will help us to understand the mechanisms which drive the turbulence and to infer important details about the microphysics of the ICM, which have so far remained elusive. In particular, we may get a handle on the effective viscosity of the ICM, which is also linked to the strength and geometry of the magnetic fields which pervade the cluster.

In addition, as detailed in Section 7, these observations will place important constraints on types of supernova explosions that have contributed to the chemical enrichment of the ICM over the life-time of the cluster.

3.3 Targets and Feasibility

The goals stated above can be achieved with four pointings, each 100 ks long (for a total of 400 ks). The locations of these pointings are shown in Figure 8. One pointing will be centered on the cluster core, while three others will be offset by approximately 3 arcminutes towards the E, SW, and NW. The E and SW pointings will sample the two X-ray bright arms, which are believed to have been produced as the AGN in M 87 inflated bubbles filled with relativistic plasma which rose buoyantly through the cluster atmosphere, dragging filaments of cool gas out of the cluster center in their wake. The NW pointing, in turn, will probe a relatively undisturbed off-axis region. Because the target is bright and nearby, the systematic uncertainties due to the cosmic and instrumental backgrounds are minimal, and we will obtain excellent statistics as demonstrated here.

⁷The term “spaxel” refers to a $1' \times 1'$ spatial resolution element of SXS.

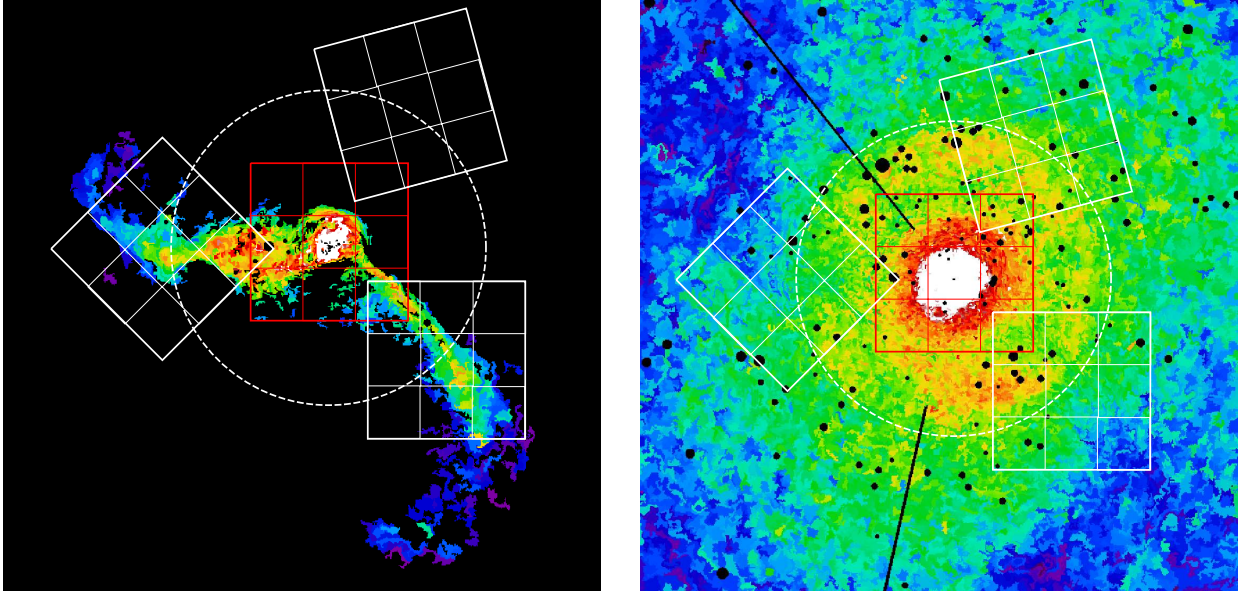


Figure 8: *Left:* Spectral normalization of the uplifted cool gas from *Chandra* spectral fitting (Werner et al., 2010). The proposed pointings (shown as boxes, each divided into nine spaxels) will probe the center, the E and SW arms, as well as one off-arm pointing where no (or significantly less) disturbance is expected due to the uplift. *Right:* Average pressure map from *Chandra* spectral fitting (Million et al., 2010), showing evidence for a weak shock front with a radius of 3 arcmin (marked with a dashed white circle). The proposed pointings will probe the turbulence in the hot gas both inside and outside this shock front. At the distance of M87, each $3 \times 3'$ box corresponds to a 14×14 kpc field of view.

3.3.1 The central pointing

The central pointing will allow us to measure accurately the properties of the cool gas in the approximately spherically symmetric 3.8 kpc core (Werner et al., 2010, and Figure 8), and determine the level of turbulent motions in the hot, 2 keV gas, in the immediate vicinity of the AGN that is generating this turbulence.

For a feasibility study, we extracted *XMM-Newton* MOS spectra of three annular regions ($0.0' - 0.5'$, $0.5' - 1.5'$, and $1.5' - 2.5'$) centered on M 87, and fitted each spectrum with a two-temperature *vAPEC* model. We then used *simx-1.3.1* to simulate the SXS spectra for the central pointing with a 5 eV response file, assuming exposure times of 50 and 100 ks.

As shown in the left panel of Figure 9, the 6.7 keV Fe line is dominated by the hotter component. Therefore, using this line alone to determine the turbulent velocity of the ~ 2 keV gas provides an alternative method which is entirely independent of the properties of the cool component. For example, assuming a $v_{\text{turb}} = 200$ km/s turbulence, fits of the simulated SXS spectrum around the 6.7 keV line (6.0–7.5 keV) give turbulent velocities of 170 ± 20 km/s and 200 ± 13 km/s with 50 ks and 100 ks exposures, respectively, considering only 1σ statistical errors.

The study of the effect of the resonant line scattering of the 6.7 keV line is complementary with direct measurements of the turbulence using line broadening. In the absence of turbulent motions, the expected optical depth of the 6.7 keV line of the core of M 87 is 1.4 (Churazov et al., 2010), and therefore we would expect this line to be suppressed. This suppression is reduced by the presence of random gas motions. Just as in the case of Perseus discussed in Section 2, the ratio of the 6.7 keV (1s2p) line strength to that of the 7.9 keV (1s3p) He-like Fe line, the latter of which is expected to be optically thin, can be used as an indicator of the effect of scattering, which in turn depends on the level of turbulence in the ICM.

However, with CCD detectors, the He-like Ni line at 7.8 keV and the He-like Fe line at 7.9 keV are blended into a single bump, and thus the inferred level of the resonant scattering in the 6.7 keV line couples with the Ni/Fe ratio. The improved spectral resolution of the *ASTRO-H* SXS will refine such measurements of the

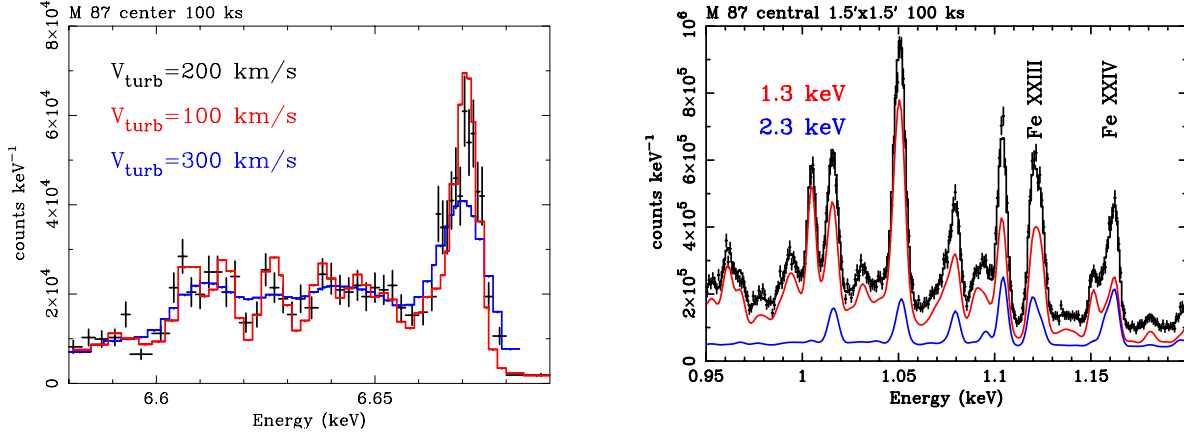


Figure 9: (left) The simulated SXS spectrum for the central $3' \times 3'$ of M 87 around the 6.7 keV Fe-K lines with a 100 ks exposure. (right) The same as the left panel but for the central $1.5' \times 1.5'$ of M 87 around the Fe L lines. The Fe L lines with optical depth ~ 1 are labeled. The red and blue lines show the contributions of the two temperature components.

resonant line scattering.

Unfortunately, because of the low average temperature of the ICM in M87, the number of photons in the He-like Fe line at 7.9 keV over the central SXS field of view is expected to be only 60 counts with a 100 ks exposure, therefore we must use either a significantly longer observation, or use other pairs of lines in order to measure the effects of resonant scattering. One possibility is to compare the line strengths of the resonance line at 6.7 keV to other lines within the 6.7 keV line complex. With a 100 ks exposure, the expected total counts in the 6.7 keV line complex and the resonance line at the center of M 87 with SXS are about 1700 and 460 counts, respectively, which provides sufficient statistics for constraining the optical depth of the resonance line. However, the flux ratios of lines in the complex depend also on the ICM temperature, and there may be systematic uncertainties due to the atomic data. The temperature structure in the ICM can be constrained accurately, using the bremsstrahlung continuum as well as other line ratios (Si, S, Ar and Ca). To constrain the systematic uncertainties in the plasma codes, we can use the spatial variation of the contribution of the resonance line to the other lines in the 6.7 keV line complex. In the cluster core, the optical depth of the resonance line is expected to be the highest, while this line should be practically optically thin at larger radii. In the central $1.5' \times 1.5'$ region, we can use 40% of the total counts for the central $3' \times 3'$ region, and test for this spatial trend (though this measurement will be affected by PSF scattering and require accurate modeling).

Moreover, the expected optical depths of two Fe-L lines (Fe XXIII at 1.129 keV and Fe XXIV at 1.168 keV) are about unity (Churazov et al., 2010). As shown in the right panel in Figure 9, these two lines mostly come from the 1 keV component. Therefore, we can use these two lines to constrain the turbulent motions of the cool 1 keV component in the cluster core. Because the lines from this cool component are seen at low energies, where the spectral resolution $\Delta E/E$ is not as high as at 6.7 keV, resonant line scattering may offer the only viable method to measure the turbulent velocities in the cool gas. Again, this will require systematic uncertainties in the atomic data to be taken into account.

3.3.2 The offset pointings

We have extracted spectra of the off-center regions shown in Figure 8 using a deep *Chandra* observation and applying the latest calibration. Using the SPEX spectral analysis package, the spectra for the E and SW arms were fit with a two-temperature model, while the spectra for the NW offset pointing were fit with a single temperature model. Following the conclusions of Simionescu et al. (2008), we fixed the abundance of the cool 1 keV gas to be twice that of the hot 2 keV ambient phase. The best-fit abundances of Si, S, Ar, Ca, and Fe

Table 3: Simulation of the offset pointings. Statistical error bars are given at the $\Delta C=1$ level. Detections below the 4σ level are not reported.

Pointing position	E	SW	SW	SW	NW
	entire pointing	entire pointing	central spaxel	central spaxel	central spaxel
Exposure time (ks)	100	100	100	50	100
kT cool (keV)	$1.14^{+0.01}_{-0.01}$	$1.05^{+0.01}_{-0.01}$	$1.13^{+0.01}_{-0.02}$	$1.09^{+0.03}_{-0.01}$	-
Y cool (10^{64} cm $^{-3}$)	$0.31^{+0.02}_{-0.03}$	$0.18^{+0.005}_{-0.01}$	$0.086^{+0.008}_{-0.004}$	$0.073^{+0.006}_{-0.003}$	-
kT hot (keV)	$2.11^{+0.01}_{-0.01}$	$2.14^{+0.01}_{-0.01}$	$1.94^{+0.02}_{-0.03}$	$1.92^{+0.05}_{-0.02}$	$2.40^{+0.03}_{-0.03}$
Y hot (10^{64} cm $^{-3}$)	$4.51^{+0.04}_{-0.03}$	$5.27^{+0.03}_{-0.03}$	$0.61^{+0.01}_{-0.02}$	$0.63^{+0.01}_{-0.02}$	$0.503^{+0.006}_{-0.006}$
v_{bulk} cool (km/s)	311^{+33}_{-23}	303^{+14}_{-18}	280^{+13}_{-33}	256^{+60}_{-28}	-
v_{turb} hot (km/s)	135^{+8}_{-8}	153^{+7}_{-8}	142^{+7}_{-27}	134^{+30}_{-30}	138^{+24}_{-26}
O cool	$0.98^{+0.14}_{-0.13} \ddagger$	$0.82^{+0.26}_{-0.22} \ddagger$	$0.96^{+0.22}_{-0.22} \ddagger$	-	-
Si cool	$1.97^{+0.22}_{-0.17}$	$2.85^{+0.44}_{-0.40}$	$2.02^{+0.50}_{-0.47}$	-	-
S cool	$2.17^{+0.53}_{-0.30}$	$3.13^{+0.76}_{-0.53}$	$1.94^{+0.54}_{-0.37}$	-	-
Fe cool	$2.08^{+0.09}_{-0.10}$	$2.28^{+0.14}_{-0.11}$	$1.93^{+0.08}_{-0.16}$	$1.72^{+0.19}_{-0.15}$	-
O hot	-	-	-	-	$0.52^{+0.07}_{-0.06}$
Ne hot	$0.82^{+0.02}_{-0.03}$	$0.83^{+0.02}_{-0.02}$	$0.76^{+0.08}_{-0.07}$	$0.89^{+0.10}_{-0.08}$	$0.89^{+0.08}_{-0.08}$
Mg hot	$0.61^{+0.02}_{-0.02}$	$0.58^{+0.02}_{-0.02}$	$0.52^{+0.06}_{-0.06}$	$0.66^{+0.08}_{-0.08}$	$0.63^{+0.07}_{-0.07}$
Si hot	$0.97^{+0.02}_{-0.03}$	$0.98^{+0.02}_{-0.02}$	$0.96^{+0.08}_{-0.08}$	$0.83^{+0.10}_{-0.09}$	$0.94^{+0.07}_{-0.06}$
S hot	$0.95^{+0.03}_{-0.03}$	$0.96^{+0.03}_{-0.03}$	$0.98^{+0.08}_{-0.09}$	$1.01^{+0.14}_{-0.16}$	$0.93^{+0.08}_{-0.08}$
Ar hot	$0.98^{+0.07}_{-0.07}$	$0.96^{+0.07}_{-0.06}$	$1.12^{+0.21}_{-0.20}$	$1.27^{+0.35}_{-0.27}$	$1.18^{+0.25}_{-0.23}$
Ca hot	$1.05^{+0.08}_{-0.08}$	$0.96^{+0.07}_{-0.07}$	$1.33^{+0.27}_{-0.24}$	-	$0.83^{+0.25}_{-0.20}$
Fe hot	$0.98^{+0.01}_{-0.01}$	$1.01^{+0.01}_{-0.01}$	$0.94^{+0.04}_{-0.05}$	$0.99^{+0.06}_{-0.06}$	$1.03^{+0.04}_{-0.04}$
Ni hot	$0.95^{+0.06}_{-0.05}$	$1.00^{+0.05}_{-0.05}$	$1.02^{+0.14}_{-0.15}$	$0.92^{+0.19}_{-0.22}$	$1.22^{+0.19}_{-0.18}$

\ddagger O^{hot} fixed with respect to Fe^{hot} by the ratio measured in the relaxed off-center pointing.

for the hot gas were consistent with 1 solar in the units of Grevesse & Sauval (1998), and were therefore fixed to this value. For O, Mg, and Ne, where *Chandra* spectra do not allow an accurate determination of the metal abundance, we have assumed their ratios with respect to Fe to be 0.5, 0.6, and 0.8, respectively, as determined with RGS (Werner et al., 2006) and converted to the solar units assumed here.

Using the best-fit parameters from the *Chandra* fits, we then assumed a line-of-sight velocity of the cool gas of $v_{\text{bulk}}^{\text{cool}} = 300$ km/s (roughly half of the sound speed in the ambient gas) and a turbulent velocity in hot gas of $v_{\text{turb}}^{\text{hot}} = 141$ km/s, and simulated the expected spectra for a 100 ks observation with the SXS, using the predicted 5eV response files. We have included the cosmic and instrumental background models, however we find these to be an insignificant contribution to the expected emission from the source.

We find that, ignoring systematic uncertainties and using a full band fit in the 0.3–10 keV range, we can measure parameters of interest with the statistical precisions shown in Table 3. We show simulations of the full field of view for the E and SW pointings, as well as one simulation of a typical 1x1 arcmin spaxel in a two-temperature region (the center of the SW arm) and a typical 1x1 arcmin spaxel in a single temperature region (the center of the NW pointing). We note that the C-stat space in our simulations is complex, with more than one local minimum. This is reflected by several highly asymmetric formal $\Delta C = 1$ error bars in Table 3. Monte Carlo simulations will be needed to assess the error bars more robustly.

Our simulations use exposure times that provide robust measurements of the Fe abundance and line-of-sight velocity of the uplifted gas, Fe^{cool} and $v_{\text{bulk}}^{\text{cool}}$, as well as the level of turbulence in the ambient 2 keV gas. These are the quantities which could not be constrained before *ASTRO-H*. These exposure times will allow us to spatially map the gas motions by determining $v_{\text{bulk}}^{\text{cool}}$ with a 10% precision and obtaining a $> 5\sigma$ detection of the turbulent velocity broadening in each 1x1 arcmin spaxel. Using the full field of view of each offset pointing, we will obtain Fe^{cool} with an exquisite statistical precision of 5%, while $v_{\text{bulk}}^{\text{cool}}$ can be measured to within ± 20 km/s and $v_{\text{turb}}^{\text{hot}}$ to within ± 10 km/s. Assuming a 7 eV response instead, we can measure Fe^{cool} to 7.5% precision per full field of view and $v_{\text{turb}}^{\text{hot}}$ to within ± 15 km/s (a 50% increase of the error bars compared to 5 eV), while the uncertainty on $v_{\text{bulk}}^{\text{cool}}$ remains unchanged.

The statistical errors given in Table 3 can be considered as a lower limit on the precision that we expect to

achieve in our observations. Most of our results will likely be systematics dominated, as explained in more detail in Section 3.4. The exposure times that we have used for these simulations are designed such that, per full field of view, we will still obtain significant detections of the three quantities of interest discussed above, even with a lower spectral resolution or if a possibly significant fraction of counts is scattered outside the detector footprint due to the PSF. Moreover, we have required a sufficient number of counts in order to measure the centroid of at least three Fe-L lines with a statistical precision of around 0.1 eV (30 km/s at 1 keV). A zoom-in on the expected spectrum of the Fe-L complex for the E arm is shown in Figure 10. We clearly detect lines emitted only by the cool gas, only by the hot gas, and by both phases. The *relative* velocity shift between the lines from the cool and the hot gas should be much less subject to systematic biases than an absolute measurement of the bulk velocity of the gas, which is limited by the nominal 1–2 eV gain calibration uncertainty.

The metal abundances of O, Ne, Mg, Si, S, Ar, Ca, Fe, Ni in the hot gas are all determined with statistical errors of less than 10%. The errors on the abundances of other metals in the cool gas, e.g. Si and S, are relatively large. To measure the chemical composition of the uplifted gas, therefore, we can hope to combine the SW and E pointings for an improved accuracy. Because only one line from O is seen in the spectrum, the abundances of O in the hot and cold gas can not be fit independently. We can estimate the O abundance in the cool gas by fixing the ratio of O/Fe in the hot gas to the value determined in the single-temperature regions. We obtain in that case a similar accuracy for O as that for Si and S (15–30%).

3.4 Remarks on sources of systematic uncertainty

Of potential concern in terms of the systematic uncertainties for these measurements are PSF scattering from the bright center of M87 outwards and scattering between the neighboring 1'–1.5' regions, and gain calibration. We have modeled the spectra from $r < 0.5'$ and 0.5–1.5' from the center of M87 obtained with *XMM-Newton* and, using a radially symmetric model for the PSF, predicted the amount of PSF scattering expected at 3 arcmin off axis towards the north, for the same distance from the center where our offset pointings are located. The result is shown in Figure 11 and demonstrates that the scattered light contribution from the center of M87 should be small.

Moreover, it will be important to understand how many counts are lost from a given spatial extraction region due to the PSF and, in turn, how many photons from immediately outside the footprint of the detector are scattered into the field of view, as well as how many photons are scattered from spaxel to spaxel. Million et al. (2010) show that the M87 atmosphere outside the arms is well stratified, and isothermal within a given radial bin, such that scattering in and out of the field of view in the tangential direction should not influence the results on the cool gas or the temperature of the hot ICM; however, the metallicity and turbulent velocity of the hot gas may be subject to an increased systematic uncertainty. In terms of the measurements per spaxel, with a 1.3' HPD PSF, a $1 \times 1'$ spaxel is only expected to contain about 44% of the flux of a point source located at its center - therefore, mixing between different spatial regions will be very important, and understanding its effects will require a precise calibration of the PSF and detailed modeling using the existing high-spatial resolution *Chandra* data.

Gain calibration uncertainties can be mitigated by measuring the relative redshifts between lines emitted (primarily) by the cool vs. hot gas, and which are close in energy (see Figure 10). With a 100 ks observation, we expect to be able to measure the centroid of most of the Fe-L lines in Figure 10 with a statistical precision of around 0.1 eV, and therefore determine the relative velocity of the cool gas with respect to the hot gas with a precision much exceeding the nominal 1 eV gain calibration uncertainty.

3.5 Beyond Feasibility

The expected optical depths of two Fe-L lines which originate mostly from the 1 keV component are approximately unity in the core of M87. Provided that the atomic physics of these transitions is calibrated accurately enough, we may be able to constrain the turbulent motions of the cool gas in the cluster center, and compare this result to the turbulence in the hot gas. Because the lines from this cool component are seen at low energies,

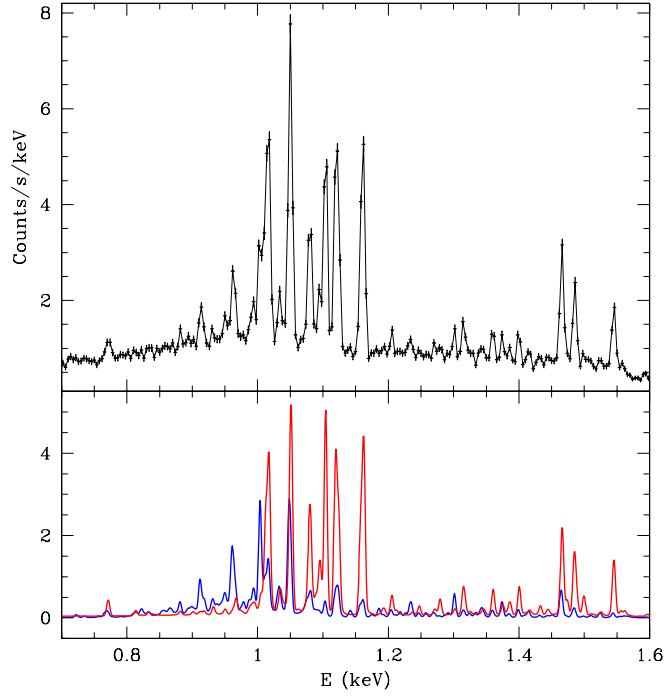


Figure 10: Zoom in on the Fe-L complex in the X-ray bright arms. The top panel shows the expected spectrum for the E pointing with *ASTRO-H*, while the bottom panel shows the line contributions to the model from the cool 1 keV component (in blue) and the hot 2 keV component (in red).

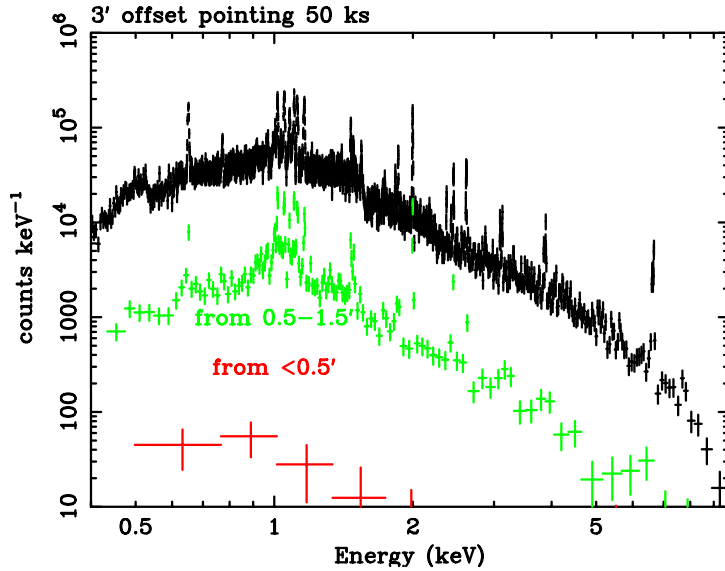


Figure 11: Expected PSF scattering contribution from the central $r < 0.5'$ (in red) and 0.5-1.5' (in green) at our proposed offset pointings centered 3' off axis, compared to the expected source spectrum (shown in black). We assumed a radially symmetric PSF.

where the spectral resolution $\Delta E/E$ is not as high as at 6.7 keV, resonant line scattering offers the only viable method to measure the turbulent velocities in the cool gas.

With deeper exposures, we will be able to measure any potential differences in chemical composition between the different gas phases. Currently, only the Fe abundance of the gas uplifted by the AGN can be measured accurately, independently from the Fe abundance of the hot gas. The Si and S abundances of the cold gas are measured with a relatively large statistical error of 30%, which probably will not be sufficient for drawing any statistically significant conclusions regarding differences in Si/Fe and S/Fe between the uplifted and ambient gas.

4 Plasma Kinematics and Cluster Masses

Overview

One of the most significant unanswered questions in both cluster astrophysics and cluster cosmology concerns the role of bulk motions and turbulence in supporting the intracluster medium (ICM) against gravity. Simulations predict that, even in relaxed clusters, bulk velocities will vary with radius and reach an appreciable fraction of the sound speed, thus providing significant non-thermal pressure support. *ASTRO-H* is the first X-ray observatory capable of testing these predictions and quantifying this support. In this section we consider how best to use spatially resolved measurements of Fe K line centroids and widths as a function of radius to constrain non-thermal pressure support in bright, relaxed clusters. These observations will improve our understanding of cluster masses, and, ultimately, of cluster cosmology. The most promising targets are Abell 2029, 2199, 1795, 478, 496, 426 (Perseus) and PKS0745. We simulate observations of the first four of these objects, which span the redshift range $0.03 < z < 0.10$, to explore the cluster distance and flux limits at which such measurements are feasible with the SXS (Perseus is considered in detail in Sec. 2). We find that interesting constraints can be placed on the run of intra-cluster plasma motion with radius in each of these objects, with a precision of $\sim 100 \text{ km s}^{-1}$ for the mean line-of-sight velocity and $\sim 100\text{--}150 \text{ km}^{-1}$ for the RMS velocity dispersion. A most compelling observation would be a set of pointings at $0.8 \times r_{2500}$ in Abell 2029, apparently the most relaxed cluster in the local Universe. These must be supplemented by short pointings at smaller radii, to bound systematic errors due to scattering from the bright cluster core. If ICM motion is not detected, these observations will provide a systematics-limited upper bound on random motions of $v_{\text{turb}} < 100 \text{ km s}^{-1}$ and an upper limit on the non-thermal pressure fraction $< 1\%$ at a radius of interest for cosmological studies. Our second goal is to extend similar but somewhat less precise measurements to a small sample of nearby, relaxed clusters to constrain the scatter in non-thermal pressure support and mass.⁸

4.1 Background and Previous Studies

Galaxy clusters mark a cross-roads of astrophysics and cosmology. Other sections of this white paper discuss a variety of ways in which *ASTRO-H* will advance our understanding of astrophysical processes shaping individual clusters. The cluster population comprises the largest and therefore the youngest virialized structures in the Universe, and its evolution has already provided significant constraints on cosmological parameters. Here we discuss that *ASTRO-H* observations that will open a new path to profound advances in the power of cluster cosmology.

Cluster studies can constrain cosmology in two independent ways. One method relies on the direct connection between the growth rate of cosmic density inhomogeneities and the cosmic expansion history. Since clusters are just such density inhomogeneities, the evolution of the cluster mass function (the number of clusters per unit volume and per unit cluster mass, as a function of cluster mass) can be related to the cosmic expansion history (Vikhlinin et al., 2009b). Moreover, the mass we infer for a cluster in general depends on the cluster distance, which in turn must be inferred from an assumed redshift distance relation; the latter also depends on

⁸Coordinators of this section: N. Ota, M. Bautz

the cosmological model. Taken together, these dependencies allow us to infer the cosmic expansion history (and in particular, the role of dark energy in the cosmic expansion) from the evolution of the cluster mass function. Vikhlinin et al. (2009b) also point out that, since the local cluster mass function can be directly related to the current amplitude of the power spectrum of density inhomogeneities, one can derive an independent cosmological constraint by comparing the local power spectrum measurement from clusters to the high-redshift power spectrum derived from the anisotropies of the cosmic microwave background (CMB). This approach is often termed the “growth-of-structure” technique.

A second approach to cluster cosmology is based on the (very reasonable) assumption that the most massive clusters are large enough to be “fair samples” of the cosmic matter distribution (White et al., 1993; Sasaki, 1996; Allen et al., 2008). In this case, the fraction of cluster mass which is baryonic can be expected to be independent of redshift. Because X-ray measurements of the cluster baryon fraction depend sensitively on the angular diameter distance to a cluster, it is possible to obtain independent, geometrical constraints on the cosmic expansion history by measuring the apparent baryon fraction as a function of redshift. In recent years both this “baryon-fraction” technique and the growth-of-structure method described above have yielded significant cosmological constraints (Allen et al., 2011; Vikhlinin et al., 2009b, and references therein).

Both of these techniques require that cluster masses can be accurately characterized for substantial numbers of clusters. In practice, modern cosmological studies rely on scaling relations between cluster mass and observable “mass proxies” which can more readily be measured than cluster masses themselves. Of course, these scaling relations must ultimately be calibrated by means of direct cluster mass measurements. In fact, accurate cosmological constraints require that both the mean mass-observable relation and the scatter in mass about that relation are known as functions of the observable.

In principle, X-ray measurements can yield accurate masses provided that the X-ray emitting cluster plasma is in hydrostatic equilibrium (HSE), and that thermal pressure alone supports the plasma against the cluster’s gravity. If these assumptions are correct, and if the three-dimensional shape of the cluster is known, then X-ray measurements of the spatial distribution of plasma density and temperature provide direct measurements of the cluster mass profile. If, on the other hand, significant non-thermal pressure supports the plasma, then HSE measurements will, in general, underestimate the true cluster mass. To date it has not been possible to test the HSE assumption directly. For this reason, significant uncertainties must be associated with HSE masses, uncertainties which limit their power in constraining cosmology.

Theoretically, it has been recognized for some time (Evrard, 1990; Norman & Bryan, 1999) that macroscopic motions of the intra-cluster plasma may indeed provide significant non-thermal pressure support. Subsonic plasma flows may be produced by infalling material, including dark matter, subclusters and galaxies, and could be manifest as organized or random motions on a variety of spatial scales. Modern N-body-hydrodynamic simulations (e.g., Lau et al., 2009; Rasia et al., 2012) present a reasonably consistent picture of these motions with the following characteristics. The magnitude of the typical mean bulk velocity, \bar{v} , and of the random motions about the mean, σ_v , each vary systematically with radius within a cluster, in the sense that the motions are smallest near cluster core and rise with radius. The motions are found to be larger in unrelaxed clusters than in relaxed clusters. The magnitudes of these motions, after scaling by a characteristic velocity (e.g. $v_{500} \equiv \sqrt{GM_{500}/r_{500}}$; see Table 4 below) seem to be nearly independent of cluster mass, at least for massive ($M_{500} \gtrsim 3 \times 10^{14} M_{\odot}$) objects including both relaxed and unrelaxed systems (Lau et al., 2009).⁹

The motions are expected to be large enough to be significant for cosmological studies. For example, Lau et al. (2009) predict, for the relaxed clusters used to calibrate scaling relations, bulk motions of $\bar{v}/v_{500} \approx 0.2$ and one-dimensional velocity dispersions of $\sigma_v/v_{500} \approx 0.10$ at $r = r_{2500}$, so the velocities are typically 100–200 km s⁻¹. Such motions should bias hydrostatic mass estimates for relaxed clusters low by typically < 10% at r_{2500} and < 15% at r_{500} . This is a significant fraction of the expected systematic uncertainty in the normalization of state-of-the-art mass scaling relations (e.g., Benson et al., 2013). Indeed, recent results from the Planck satellite, which imply some tension between the cosmological parameters determined from the growth of structure method and the CMB data, have suggested that biases in HSE masses may be even larger

⁹ M_{500} and r_{500} are the mass and radius associated with the volume within which the mean cluster density is 500× the critical cosmological matter density.

(Planck Collaboration XX, 2014; von der Linden et al., 2014).

Some observational efforts have been made to detect cluster plasma motions. Although Tamura et al. (2011) used the *Suzaku* XIS to measure the 1500 km s^{-1} infall speed of a subcluster in the well-known merging system Abell 2256, for cosmologically important relaxed clusters only upper limits have been established to date. CCD spectrometers do not have the resolution required to detect motions at the level expected in these systems. For example, Ota et al. (2007) used the *Suzaku* XIS to place an upper limit of $\sim 1400 \text{ km s}^{-1}$ on bulk motions in the Centaurus cluster. Sanders et al. (2011) used the *XMM-Newton* RGS to place upper limits on velocity broadening, generally $< 1000 \text{ km s}^{-1}$, in a number of clusters. These results pertain only to the cores (with $r \lesssim 0.5'$) of cool-core clusters, and are somewhat dependent on the unknown spatial variation of the spectra. Model-dependent upper limits on broadening of $100\text{--}300 \text{ km s}^{-1}$ are claimed for the cores of Abell 496 and Abell 1795 (Sanders et al., 2011), for example. These limits are consistent with the predictions noted above.

We show here that *ASTRO-H* SXS spectroscopy can reveal the expected motions and the associated non-thermal pressure support. An empirical constraint on the resulting bias in scaling relations between X-ray observables and 'true' masses determined from weak lensing, would clearly be an important contribution to cluster cosmology. We note also that simulations are frequently relied on for estimates of the scatter in scaling relations (e.g., Kravtsov et al., 2006), so any empirical test of the validity of the simulations could provide an indirect assessment of the assumed scatter. Finally, if measurements of non-thermal pressure support could eventually be performed on a sufficiently large sample of objects, it might be possible to use this information to discover selection criteria with which to assemble a sub-sample of objects (presumably those with the least non-thermal support) for which especially low-scatter mass estimates can be made. Such a sub-sample would in turn permit exceptionally precise cosmological constraints.

Such measurements would also improve our understanding of cluster astrophysics. For example, the simulations referred to above all require assumptions about transport processes (e.g., viscosity and thermal conduction) in the intracluster plasma, about which little is known. Direct measurements of the plasma velocities could test some of these assumptions, and perhaps even improve our knowledge of the allowed range for the transport coefficients. More fundamentally, there is evidence that the two approaches to hydrodynamical simulation (smoothed-particle hydrodynamics, or SPH, and Eulerian) may not produce consistent results in detail (Rasia et al., 2012), so tests of their basic predictions may be helpful in judging the reliability these techniques.

4.2 Prospects and Strategy

The *ASTRO-H* SXS, with its superior spectral resolution, will enable accurate measurements of line broadening and shifts for the He-like iron-K emission. For some objects, measurements of the H-like iron-K line may also be useful. We aim at revealing the dynamical states of the cluster gas and improving the cluster mass model by incorporating the pressure support due to gas motions. Our strategy is to observe the most relaxed clusters for which SXS observations are practical, and to map them to a radius as close to $\sim r_{2500}$ as possible. Relaxed clusters are the most useful for cosmological work because they are expected to obey the most accurate (least biased) and lowest-scatter mass-observable relations. Several factors motivate us to map to radii approaching $\sim r_{2500}$. As noted above, the magnitude of non-thermal pressure support is expected to increase with radius. Moreover, as discussed below, the contaminating effects of scattering from the bright cores of these relaxed objects should generally decrease with increasing radius. Finally, since the most accurate mass measurements are ultimately expected to be obtained from weak lensing observations of an ensemble of clusters, we wish to measure the non-thermal pressure support to a radius at which weak lensing measurements can be made. At present weak lensing mass measurements can be made to radii as small as $\sim r_{2500}$; at smaller radii, confusion between cluster galaxies and (lensed) background objects becomes problematic. As weak lensing techniques improve, we expect that the reliable mass measurements may be made at radii as small as $0.75r_{2500}$.

Measurements of line broadening will yield the line-of-sight velocity dispersion that can arise from turbulence in the ICM. If the turbulence is isotropic, it will provide the pressure support $p_{\text{turb}} = \rho_{\text{gas}} v_{\text{turb}}^2$ of the

amount

$$\frac{p_{\text{turb}}}{p_{\text{therm}}} \simeq 1.3 \times 10^{-2} \left(\frac{v_{\text{turb}}}{100 \text{ km s}^{-1}} \right)^2 \left(\frac{\mu}{0.6} \right) \left(\frac{kT}{5 \text{ keV}} \right)^{-1}. \quad (1)$$

where v_{turb}^2 is the one-dimensional velocity dispersion of turbulence, ρ_{gas} is the gas mass density, $p_{\text{therm}} = \rho_{\text{gas}} kT / \mu m_{\text{p}}$ is the thermal pressure, μ is the mean molecular weight, and m_{p} is the proton mass. These pressure terms contribute to the hydrostatic mass via

$$M(< r) = - \frac{r^2}{G \rho_{\text{gas}}} \frac{d(p_{\text{therm}} + p_{\text{turb}})}{dr}. \quad (2)$$

Our primary goal is hence to measure for the first time the contribution of turbulence to the total pressure support with a percent order accuracy and to infer its impact on the mass estimates of galaxy clusters. The measurements around the bright cluster center will be limited by systematic errors on the width of the line spread function and thermal broadening for which a conservative estimation gives the sum of $\Delta v_{\text{turb}} \sim 100 \text{ km s}^{-1}$ (90%), whereas the extent to which the measurements can be done within feasible observing time is controlled by photon statistics. This level of accuracy is also necessary for unveiling or giving meaningful constraints on relatively mild gas motions inferred from numerical simulations near the cluster core (e.g., Lau et al., 2009). Equation (2) further implies that an accurate measurement of the radial gradient of v_{turb}^2 is crucial for mass reconstruction.

In addition, measuring the shifts of a line centroid will directly yield the line-of-sight bulk velocity v_{bulk} of the amount

$$\frac{v_{\text{bulk}}}{v_{\text{sound}}} = 8.7 \times 10^{-2} \left(\frac{v_{\text{bulk}}}{100 \text{ km s}^{-1}} \right) \left(\frac{\mu}{0.6} \right)^{1/2} \left(\frac{kT}{5 \text{ keV}} \right)^{-1/2}, \quad (3)$$

where $v_{\text{sound}} = \sqrt{5kT/3\mu m_{\text{p}}}$ is the sound speed. By mapping v_{bulk} over an appreciable range of radius, we can also perform a direct test on the validity of hydrostatic equilibrium and explore the nature of any coherent motions such as rotation of the ICM. The measurements will also be limited by systematic errors on the energy scale near the center and by statistical errors at the outermost observable regions. It is expected that an accuracy of $\Delta v_{\text{bulk}} < 100 \text{ km s}^{-1}$ is achievable including systematics, which improves the current accuracy by more than a factor of ~ 5 (Tamura et al., 2011, for the merging cluster A2256) and allows the first measurements of the gas bulk motion in relaxed clusters.

Another important and nontrivial systematic effect on this study arises from scattering of photons by relatively broad wings of the Point Spread Function (PSF); the sharply peaked X-ray emission toward the cluster center may contaminate the velocity measurements at fainter off-center regions. Further exacerbating this problem are the centrally peaked abundance profiles in relaxed, cool core clusters, which result in even greater contamination of the Fe line flux in the outer regions compared to the continuum flux. As demonstrated by our detailed simulations presented in the following sections, this effect can be adequately accounted for by performing a series of pointings along the radius from the center of a cluster and solving for intrinsic distributions of the line width and shifts (plus temperature and metallicity if necessary). Existing high spatial resolution data from *Chandra* and *XMM-Newton* will play a crucial role in modeling accurately the scattered contributions of the continuum emission.

4.3 Targets and Feasibility

The foregoing considerations imply that viable targets for our study are bright, relaxed clusters with sufficient radial extent to minimize the PSF scattering effect, the electron temperature above $\sim 4 \text{ keV}$ to produce prominent Fe-K line emission, and existing high quality *Chandra* and *XMM-Newton* data. The best targets include Abell 2029, 2199, 1795, 478, 496, and PKS0745; the parameters of these clusters are listed in Table 4, and temperature, metal abundance, and surface brightness profiles are shown in Figure 12. In the following, we present

Table 4: Summary of parameters for a sample of relaxed clusters.

Cluster	z^a	kT^a [keV]	r_{2500}^b [Mpc, arcmin]	r_{500}^b [Mpc, arcmin]	v_{500} [km s ⁻¹]	ref. ^b
A2029	0.077	8.5	0.66, 7.6	1.36, 15.7	1510	V
A2199	0.030	4.0	0.41, 11.5	1.02, 28.7	1130	R
A1795	0.062	6.1	0.50, 7.0	1.24, 17.5	1370	V
A478	0.088	7.3	0.65, 6.6	1.34, 14.6	1480	V
A496	0.033	4.1	0.36, 10.1	0.89, 25.2	990	R
PKS0745	0.103	8.0	0.52, 4.8	1.31, 12.0	1450	R

^a From the X-ray Galaxy Clusters Database (<http://bax.ast.obs-mip.fr>).

^b Scale radii are from Reiprich et al. (2002, ‘R’) and Vikhlinin et al. (2006, ‘V’).

Table 5: Radial positions of simulated regions in A2029, A2199, A1795, and A478.

Region number	Center [arcmin]	Range between boundaries [arcmin]
1	0	-1.5 – 1.5
2	3	1.5 – 4.5
3	6	4.5 – 7.5
4	9	7.5 – 10.5
5	12	10.5 – 13.5

our simulation results for the first four clusters, which cover a range of redshifts, mass (mean temperature), and different levels of the impact of the PSF effect mentioned above.

Abell 2029, though relatively distant, appears to be the most relaxed cluster in the redshift range we consider (Mantz et al., in preparation), and thus the best choice for contributing to cluster cosmology. Abell 2199 at $z = 0.030$ serves as an ideal example of a very extended cluster with a relatively mild central emission peak for which the PSF effect is likely to be minimal. A1795 at $z = 0.062$ is a more representative case of a larger sample of clusters that can be resolved by *ASTRO-H* with the stronger PSF effect. Finally, A478 at $z = 0.088$ has the higher mass but is amongst the most distant clusters resolvable by *ASTRO-H*.

In order to constrain the contribution of non-thermal pressure to the hydrostatic condition, we aim to measure the line broadening and shift of He-like Fe-K line at 6.7 keV with an accuracy better than $\sim 100 \text{ km s}^{-1}$ in these nearby relaxed clusters. We consider one-dimensional SXS mapping of bright clusters and perform feasibility studies to estimate the necessary exposure time based on detailed spectral simulations including the PSF scattering effect. The simulations are performed for a series of pointings on annuli shown in Figure 13 with boundaries given in Table 5. To take into account large uncertainties in the radial distribution of turbulence, we investigate the following three cases; (a) v_{turb} is constant over radius, (b) v_{turb} increases with radius, and (c) v_{turb} decreases sharply as $v_{\text{turb}} = 500 \text{ km s}^{-1}$ inside the core and $v_{\text{turb}} = 0 \text{ km s}^{-1}$ elsewhere. Cases (a) and (b) are consistent with the current upper limits on turbulence in the cluster cores (Sanders et al., 2011), whereas case (c) is intended to exhibit a limit in which the PSF scattering from the bright core has the largest impact on velocity measurements at larger radii.

4.3.1 Abell 2029

We simulate SXS observations of Abell 2029 for the pointing regions $j = 1-4$; region 3 is centered at about $0.8 \times r_{2500}$ (540 kpc, 6.5 arcmin), and its outer boundary is very close to r_{2500} . The assumed spectral parameters are listed in Table 6. The effect of PSF scattering is estimated by convolving the *XMM-Newton* surface brightness

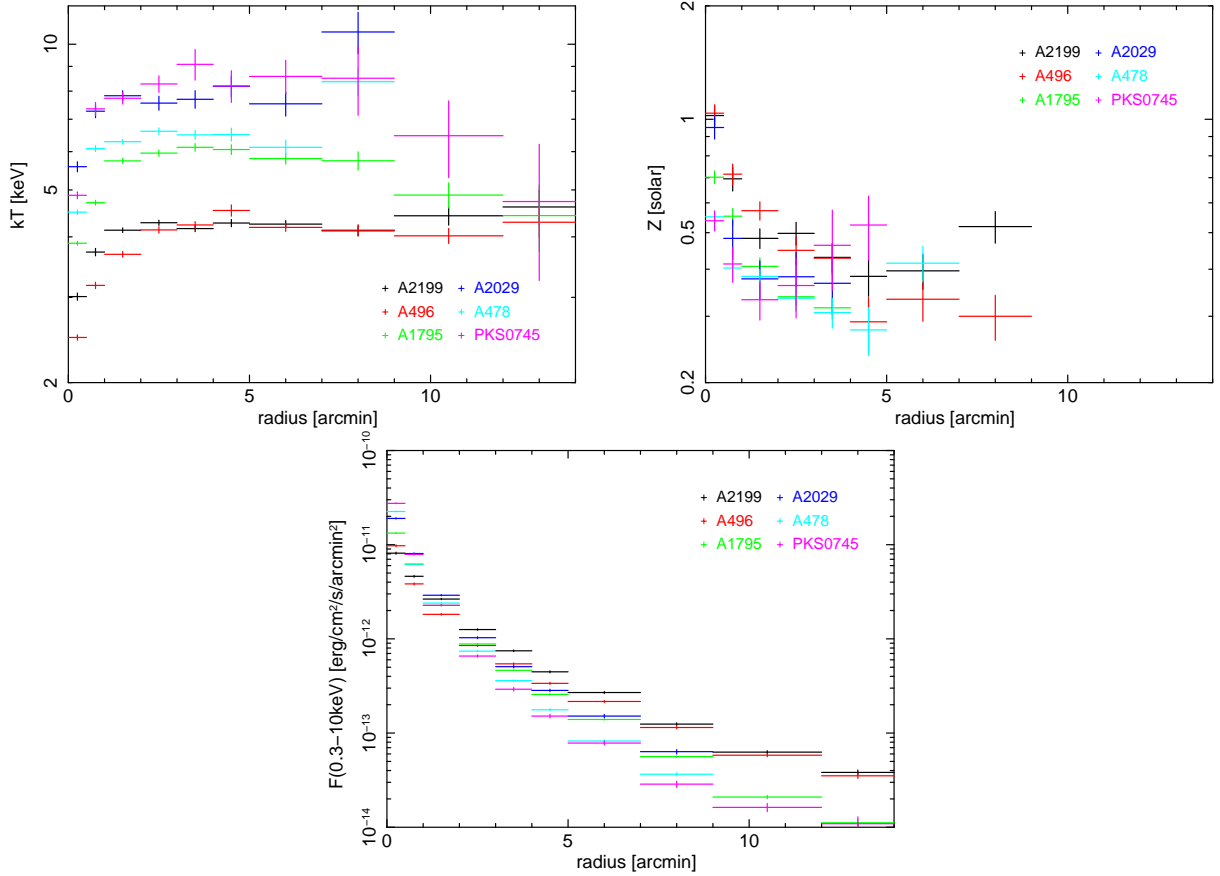


Figure 12: Temperature, metal abundance, and surface brightness profiles for the cluster sample, from Snowden et al. (2008).

distribution in the 0.3–10 keV band (Table 5 in Snowden et al. , 2008) with the SXT PSF model of January 2013. Table 7 gives the fraction of photons in the j -th SXS pointing region, originating from the i -th annular image. Here the vignetting factor is taken into account by referring to “SXT_VIG_to110119.fits”. Using the calculated photon distributions and the SXS response file with FWHM = 5 eV¹⁰, we have created the SXS mock spectra for four pointing regions, $j = 1-4$, in the cluster (Figure 14). The parameters, kT , Z , z , v_{turb} , and the spectral normalization are allowed to vary and fitted in each annulus simultaneously, while the fractions of scattered photons (both continuum and the 6.7 keV Fe line) are fixed at the values given in Table 7. The four spectra are fitted simultaneously and Figures 15–17 show the results for the cases (a)–(c), respectively. The quoted errors are at the 90% confidence.¹¹

With the total exposure of about 400 ks, the turbulent velocity can be measured with a statistical accuracy of $\lesssim 100 \text{ km s}^{-1}$ out to region $j = 3$, corresponding to about $0.8 r_{2500}$ for this cluster. As expected, the PSF effect has the largest impact in case (c) and can bias the measured values of v_{turb} outside the cluster core.

4.3.2 Abell 2199

We simulate SXS observations of Abell 2199 for the five SXS pointing regions $j = 1 - 5$, assuming the spectral parameters in Table 8, and the scattered light contribution given in Table 9. These pointings cover the cluster to a maximum radius of about 450 kpc, with the outermost pointing centered just beyond r_{2500} (see Table 4). Using the SXS response files noted in the previous subsection, we have created mock SXS spectra for the five

¹⁰The detector response: ah_sxs_5ev_basefilt_20100712.rmf (the baseline version) and the telescope arf: sxt-s_120210-ts02um_intallpxl.arf are used in the spectral simulation.

¹¹Calibration errors of the PSF shape lead to the systematic uncertainty in measuring line profiles particularly in the outer regions of clusters. Our earlier analysis suggested that a PSF calibration accuracy of 10% or better would be sufficient for mapping nearby clusters.

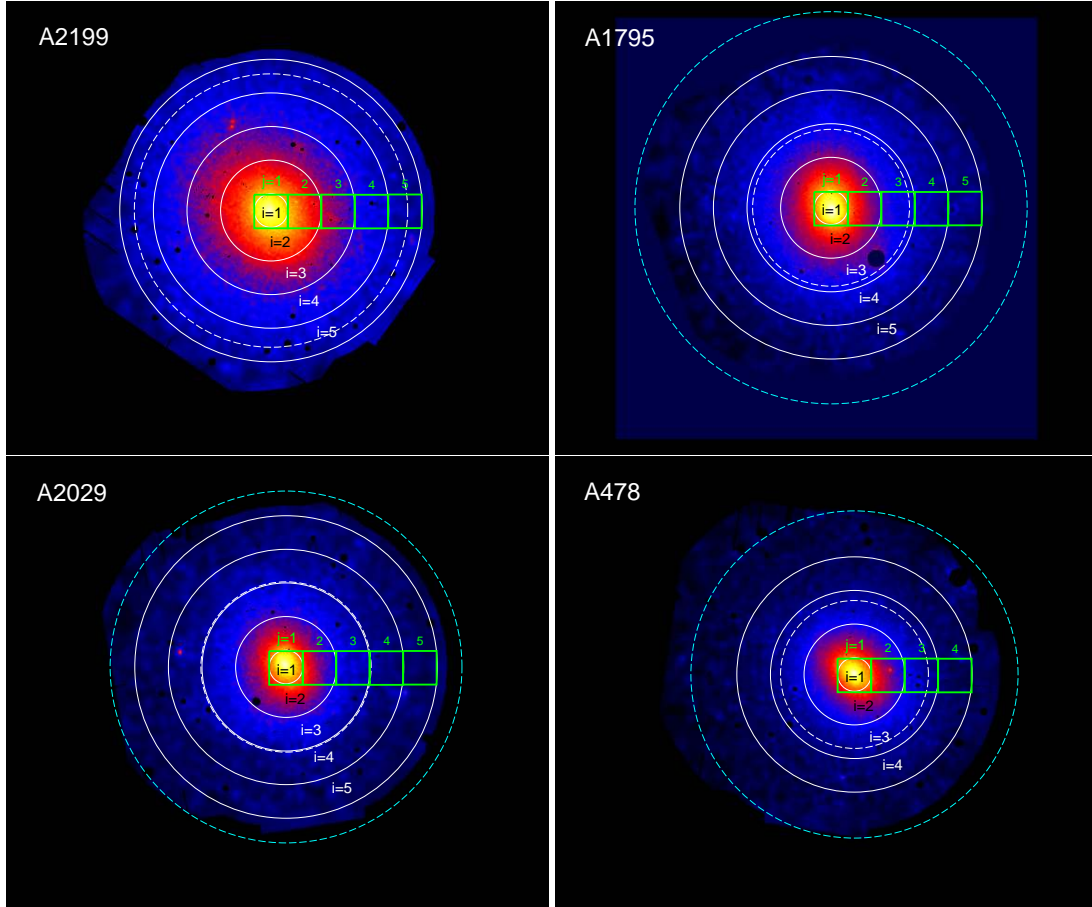


Figure 13: *XMM-Newton* images of A2199 ($z = 0.030$; top left), A1795 ($z = 0.062$; top right), A2029 ($z = 0.077$; bottom left) and A478 ($z = 0.088$; bottom right). The annuli ($i = 1, 2, \dots$) and the $3' \times 3'$ pointing regions ($j = 1, 2, \dots$) used in our simulations are indicated by white circles and green boxes, respectively. The scale radii of r_{2500} and r_{500} are shown with the inner and outer dashed circles. For A2199, r_{500} is outside the image.

regions. The five spectra are fitted simultaneously over the 0.3 – 10 keV band. Figures 18–20 show the results for the cases (a)–(c), respectively.

With the total exposure time of about 550 ks (1 Ms), the turbulent velocity can be measured to the statistical accuracy of $\lesssim 100 \text{ km s}^{-1}$ out to region $j = 4$ ($j = 5$), corresponding to about $0.85 r_{2500}$ ($1.1 r_{2500}$) in this cluster.

4.3.3 Abell 1795

We simulate observations of Abell 1795 in a similar way to Abell 2029 and Abell 2199, for the input parameters listed in Table 10. We use the PSF model to estimate the scattered light contribution from each annulus into each SXS field, as shown in Table 11. In this case, we simulate four SXS pointings, extending to 10.5 arcmin. The outer edge of Region 3 reaches just past r_{2500} (500kpc, 7.0 arcmin). We simulate case (a): a constant v_{turb} , case (b): a rising v_{turb} profile, and case (c): v_{turb} decreases sharply. As with Abell 2199, the parameters kT , Z , z , the turbulent velocity v_{turb} , and normalization are allowed to vary, while the fractions of scattered photons are fixed to those given by the image simulations. The best-fit parameter constraints are shown in Figures 21–23 for three cases. The quoted and plotted errors are at 90% confidence.

With a total exposure time of 400 ks, the turbulent velocity can be measured to a statistical accuracy of $\lesssim 100 \text{ km s}^{-1}$ out to region $j = 3$, corresponding to about r_{2500} . The additional pointing for region $j = 4$ ($0.6 r_{500}$) requires a large amount of time; 400 ks will enable interesting constraints only if v_{turb} is quite large,

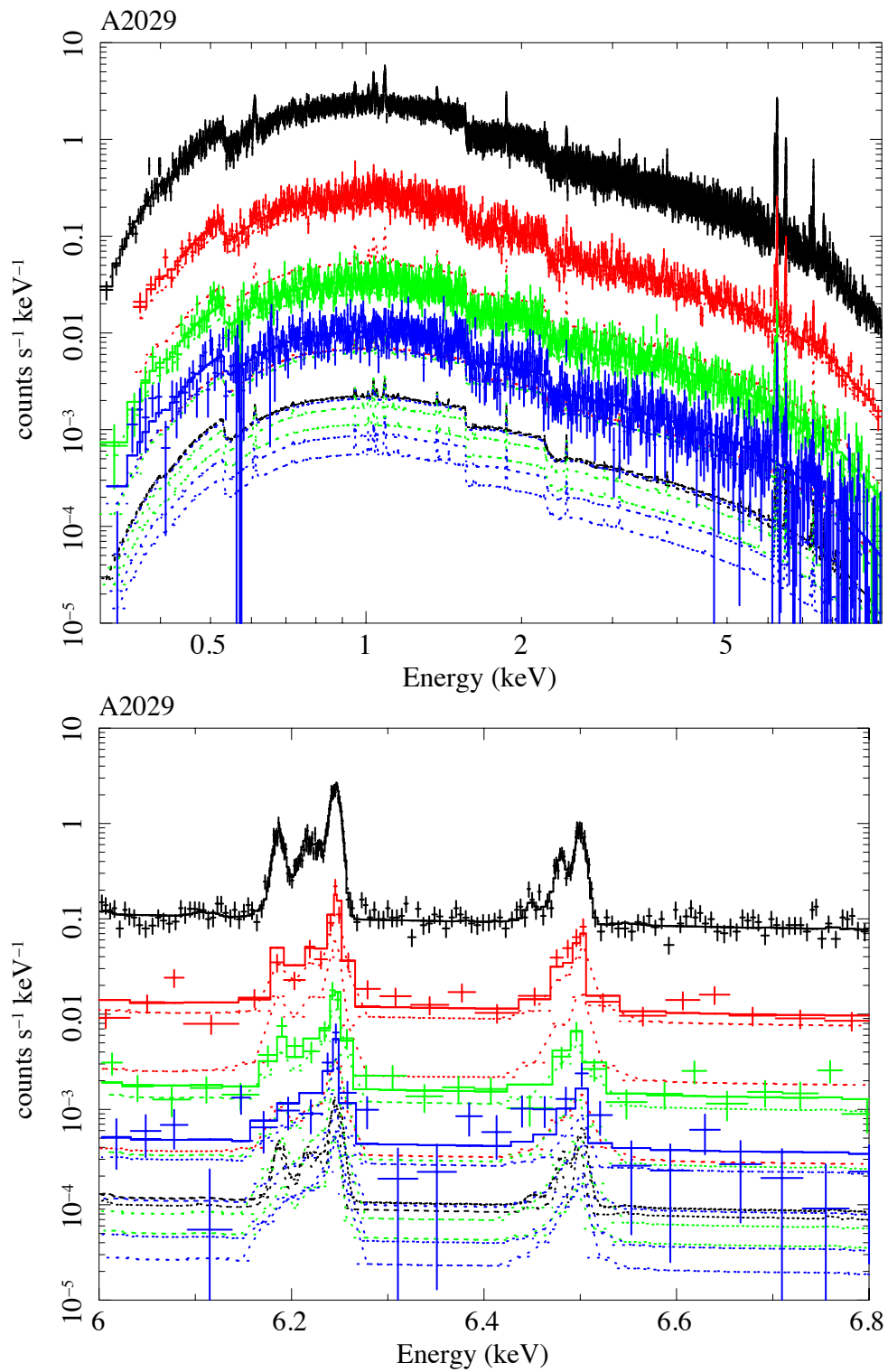


Figure 14: Top: Simulated SXS spectra of A2029 for case (a). The data for the regions $j = 1/2/3/4$ are shown with the black/red/green/blue crosses, respectively and the scattered components are indicated with the dotted lines. Bottom: Blow-up of the top panel.

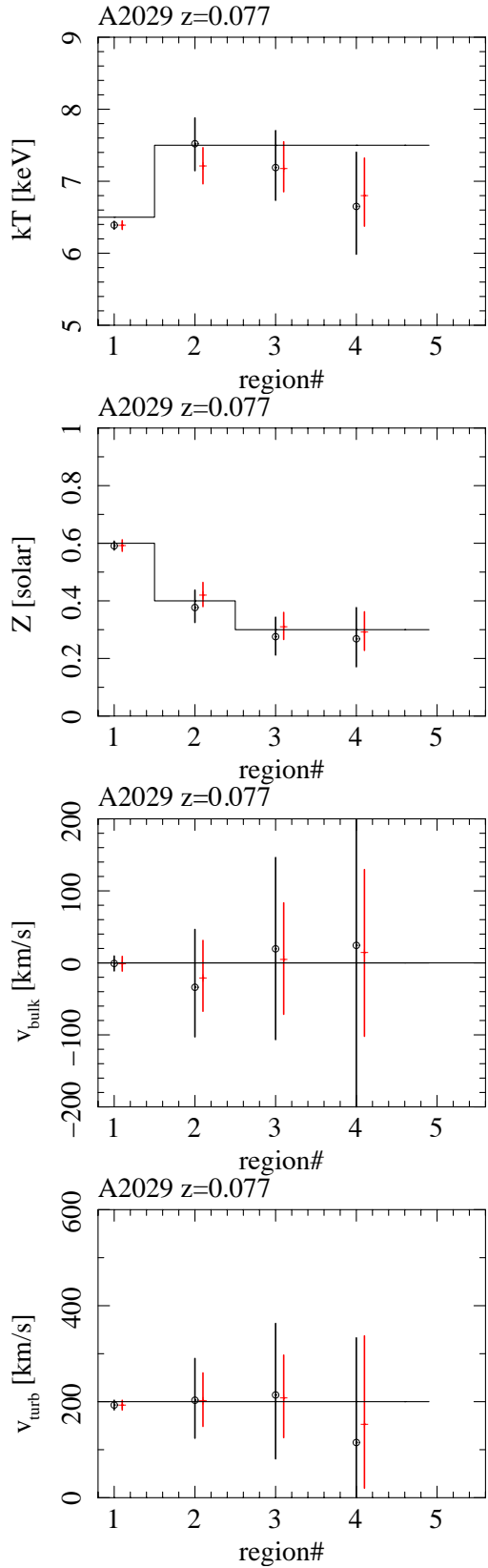


Figure 15: Results of simultaneously fitting the spectra of all annuli (black circles) or separately fitting the spectrum of each annulus (red crosses) in A2029 for case (a): v_{turb} is constant over radius. The solid line indicates the input parameter values of the simulations. Errors are at the 90% confidence.

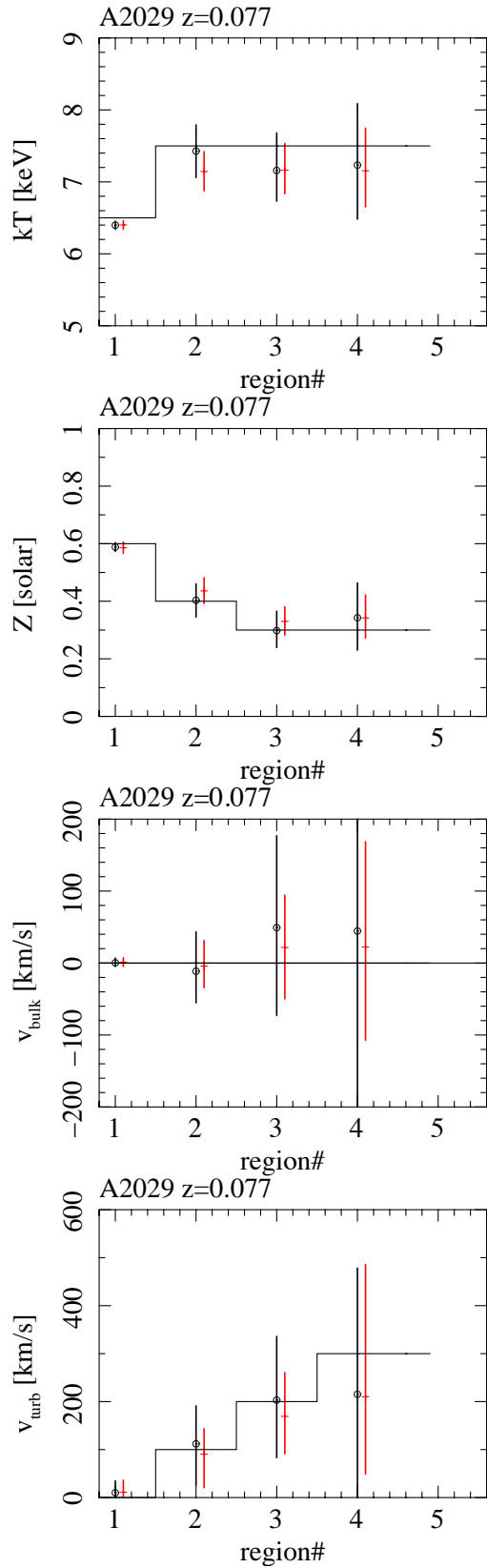


Figure 16: Same as Figure 15, but for case (b): v_{turb} increases with radius.

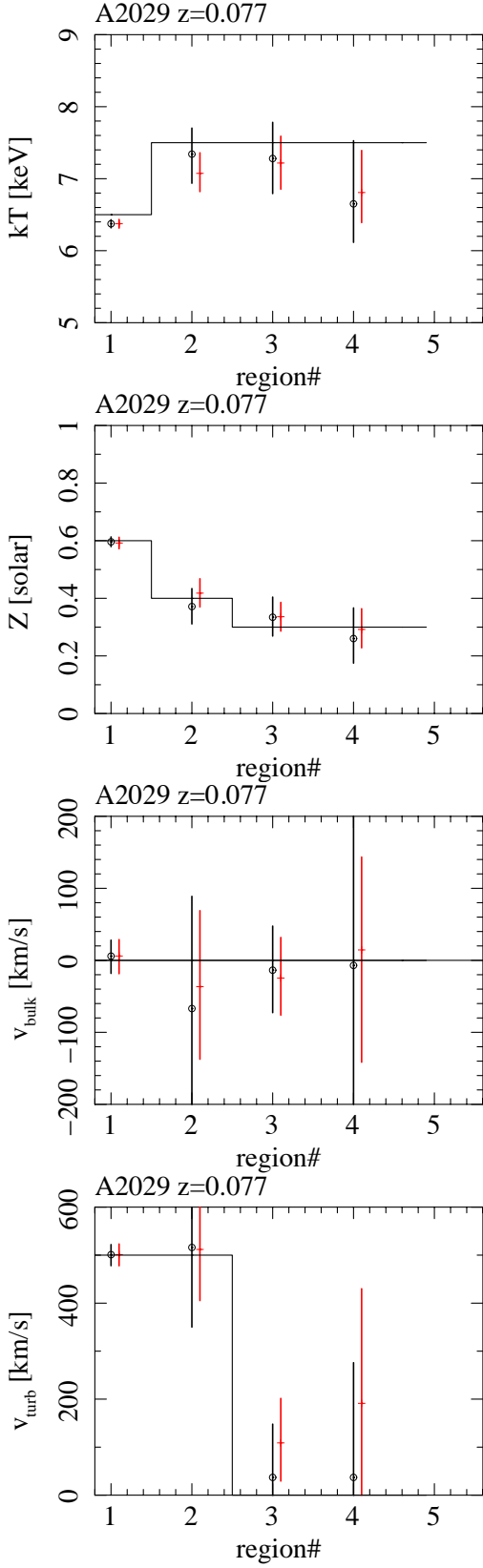


Figure 17: Same as Figure 15, but for case (c): v_{turb} decreases with radius.

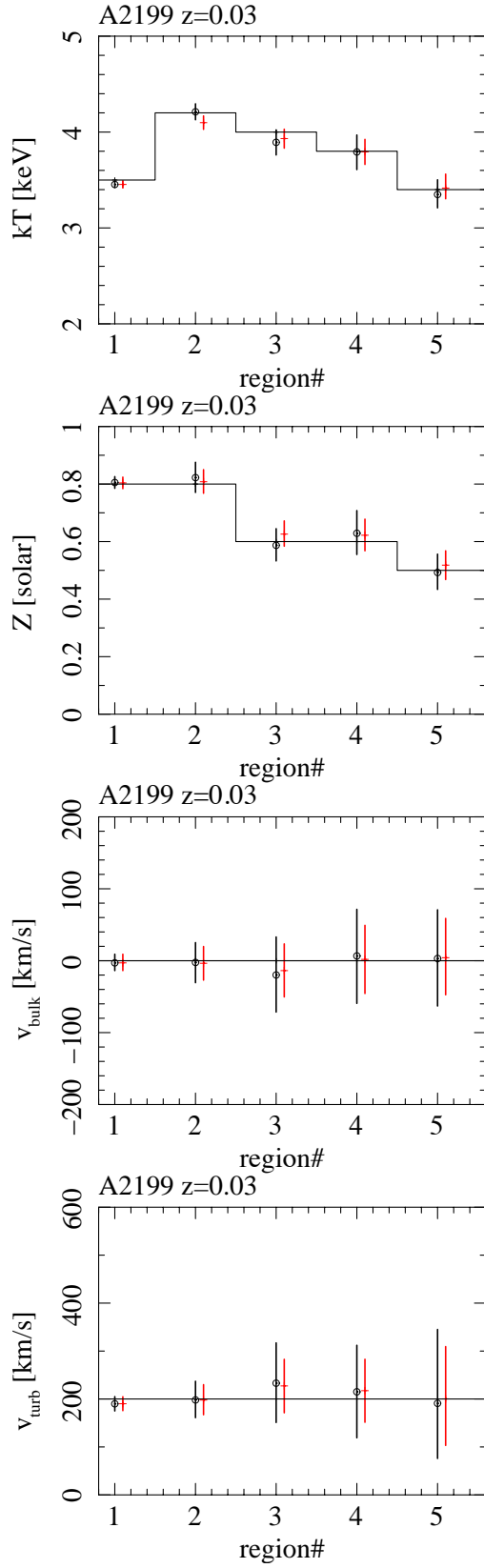


Figure 18: Same as Figure 15, but for A2199 and case (a).

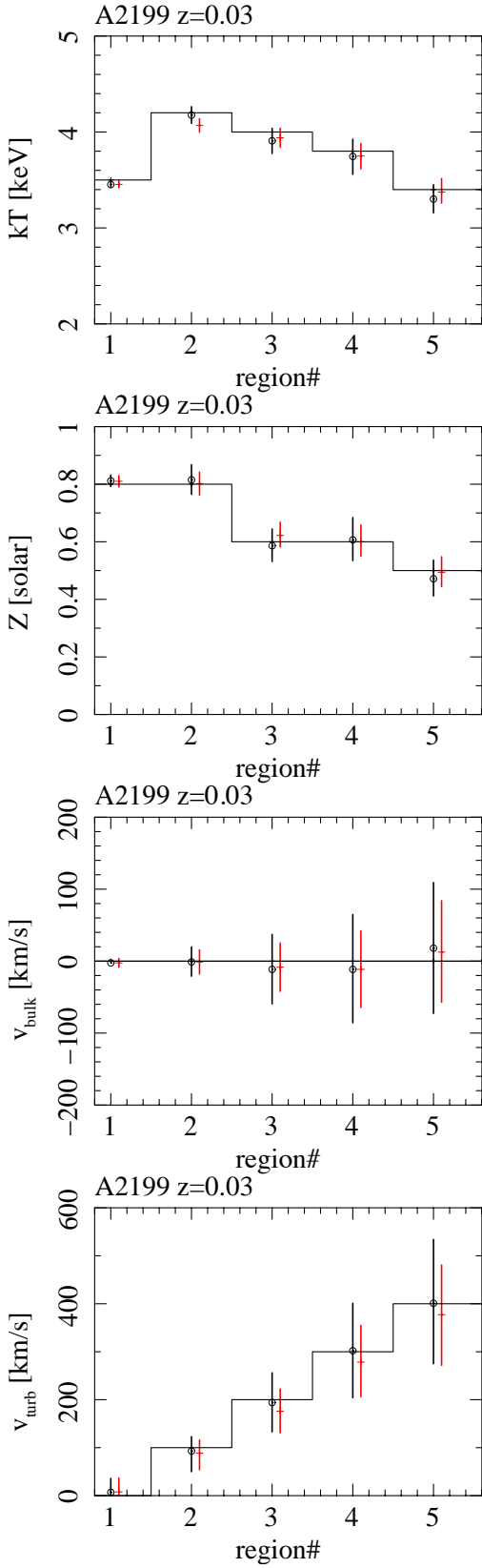


Figure 19: Same as Figure 15, but for A2199 and case (b).

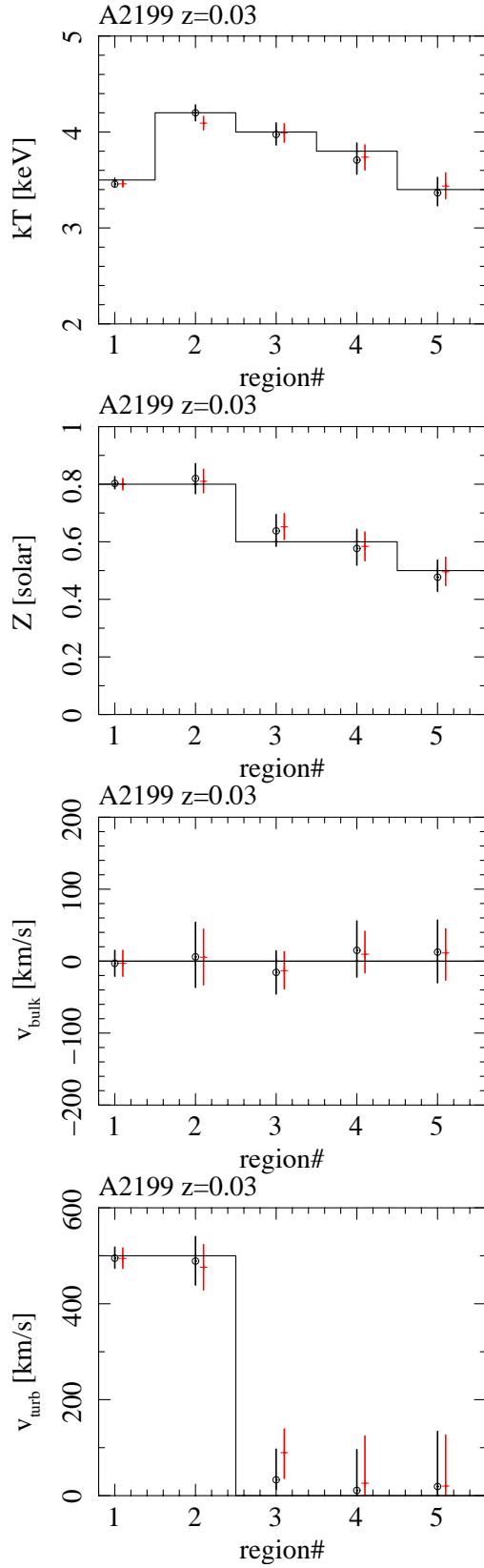


Figure 20: Same as Figure 15, but for A2199 and case (c).

Table 6: Input parameters assumed in the spectral simulations for A2029. Three models are considered for the radial distribution of turbulence: (a) v_{turb} is constant over radius, (b) v_{turb} increases with radius, and (c) v_{turb} decreases sharply outside the core. The hydrogen column density is fixed at $N_{\text{H}} = 3.0 \times 10^{20} \text{ cm}^{-2}$.

Reg	kT [keV]	Z [solar]	Flux [$\text{erg s}^{-1} \text{ cm}^{-2}$] (0.3–10 keV)	v_{turb} [km s^{-1}]			Exposure [ks]
				(a)	(b)	(c)	
1	6.5	0.6	6.5×10^{-11}	200	0	500	50
2	7.5	0.4	7.5×10^{-12}	200	100	500	50
3	7.5	0.3	1.0×10^{-12}	200	200	0	300
4	7.5	0.3	3.0×10^{-13}	200	300	0	600

Table 7: Fraction of photons at 0.3–10 keV in the j -th simulated regions originating from the i -th annuli for A2029 (note the scattering fractions of the Fe line flux are greater, because of the peaked abundance profile given in Table 6).

	$i = 1$	$i = 2$	$i = 3$	$i = 4$
$j = 1$	1.000	0.000	0.000	0.000
$j = 2$	0.201	0.772	0.027	0.000
$j = 3$	0.048	0.185	0.734	0.033
$j = 4$	0.053	0.086	0.203	0.658

as in case (b).

4.3.4 Abell 478

Simulated SXS spectra for A478 are created assuming the spectral parameters given in Table 12, using the methods described above for the previous three clusters. The scattered fractions of the photons are shown in Table 13. Region 3 is centered just beyond r_{2500} (5.8 arcmin). Given large fractions of scattered photons in this cluster, we fix the temperature of each region to the input value and fit simultaneously the spectra of regions $j = 1$ –3 to constrain v_{turb} , v_{bulk} , and Z ($j = 4$ is not used due to large statistical errors). The errors are at the 90% confidence. Figures 24–26 show the fitting results for the cases (a)–(c), respectively.

Abell 478 is the most challenging cluster among those discussed in detail here. With a total of 250 ks exposure, one obtains useful constraints on the bulk velocity in three innermost bins, but the turbulent velocity dispersion (v_{turb}) is well-constrained only in the central two pointings, and this result is achieved only if the plasma temperature is known a priori. We have not yet determined whether temperature information from CCD-resolution spectra is adequate to allow the turbulent velocities to be constrained in the manner we have simulated here. We note that, if so, the two central pointings, requiring a total of 100 ks, can constrain v_{turb} at $r < r_{2500}$ in this cluster.

4.4 Discussion

The tradeoff between cluster distance, measurement radius, and detected iron-line flux for our sample is summarized in Table 14. The table compares the iron-line counting rates, for both He-like and H-like ionization states, for Abell 2199, our nearest and least massive cluster, and Abell 2029, one of our most distant and most massive objects, at several radii. The Perseus cluster is also included for reference. The tabulated line counting rates are obtained assuming zero line broadening. The values in the table do not account for vignetting, which will reduce the line counting rates by about 15%.

Table 14 shows that reducing the measurement radius from r_{2500} to $0.8 r_{2500}$ can raise the counting rate by a factor of 1.5 – 2. It also shows that the hotter ICM in A2029 provides an additional bonus of 40% more counts from the H-like line, compared to that in A2199. The photons from the H-like line not only provide statistically stronger constraints on line broadening; they also provide a valuable consistency check, and allow

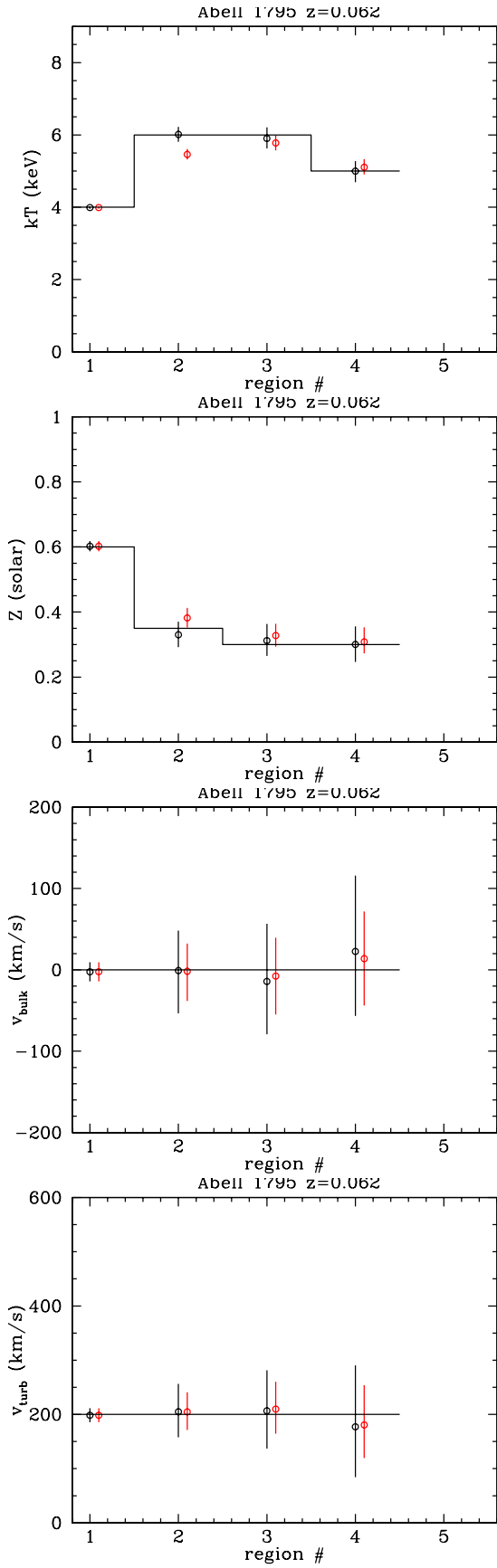


Figure 21: Same as Figure 21, but for A1795 and case (a).

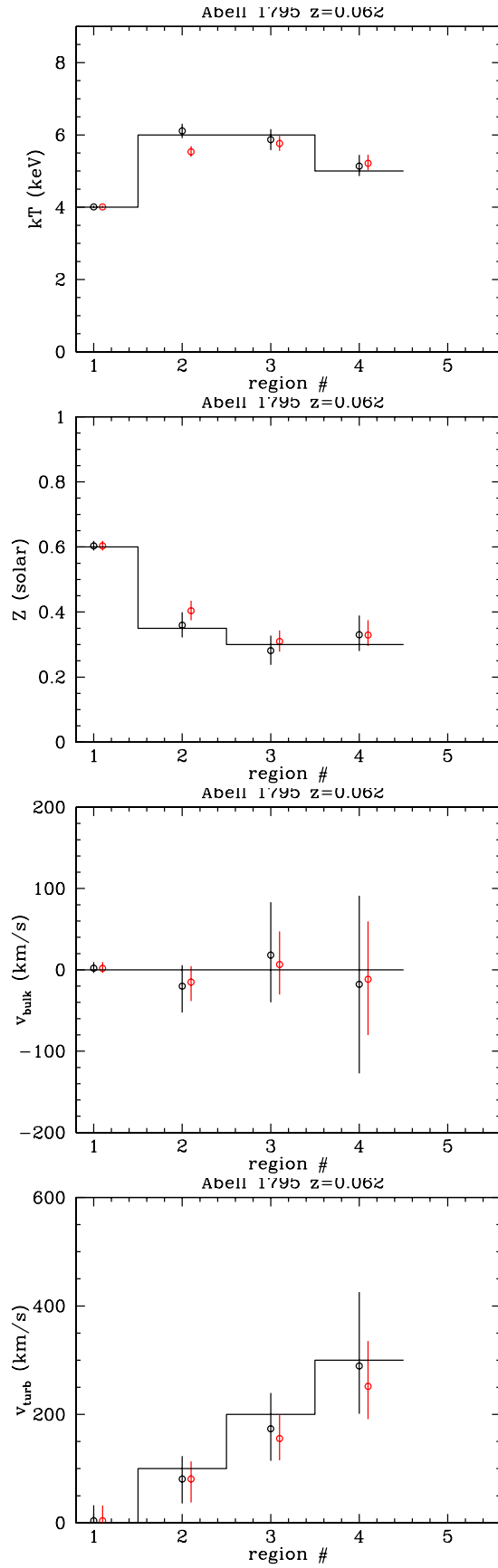


Figure 22: Same as Figure 15, but for A1795 and case (b).

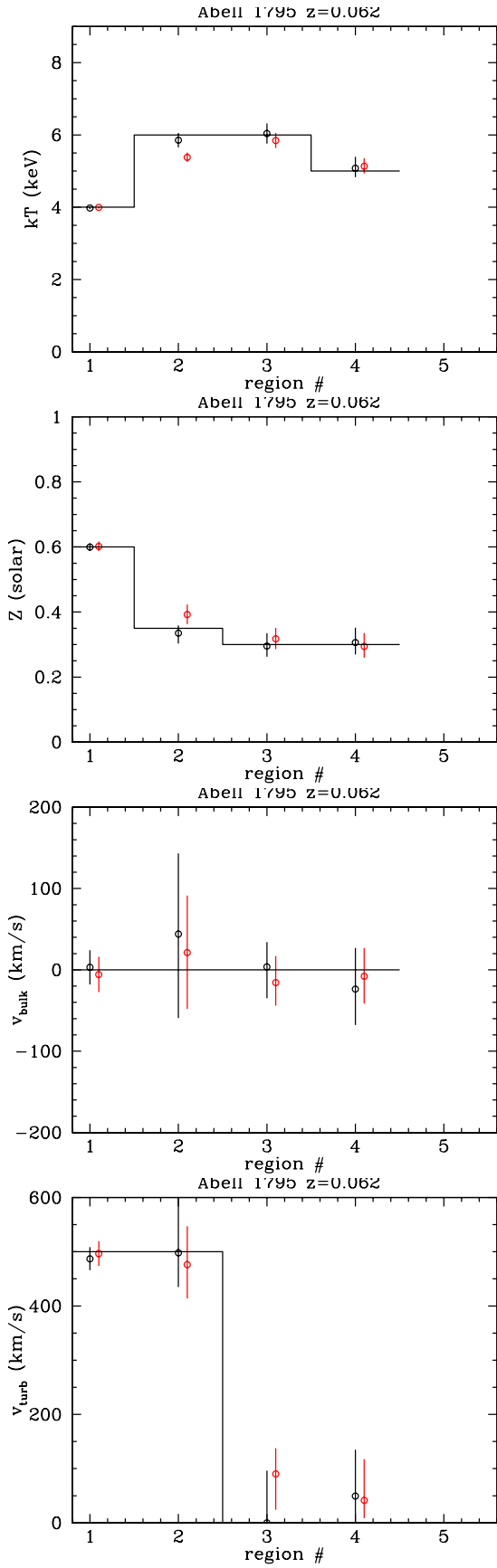


Figure 23: Same as Figure 15, but for A1795 and case (c).

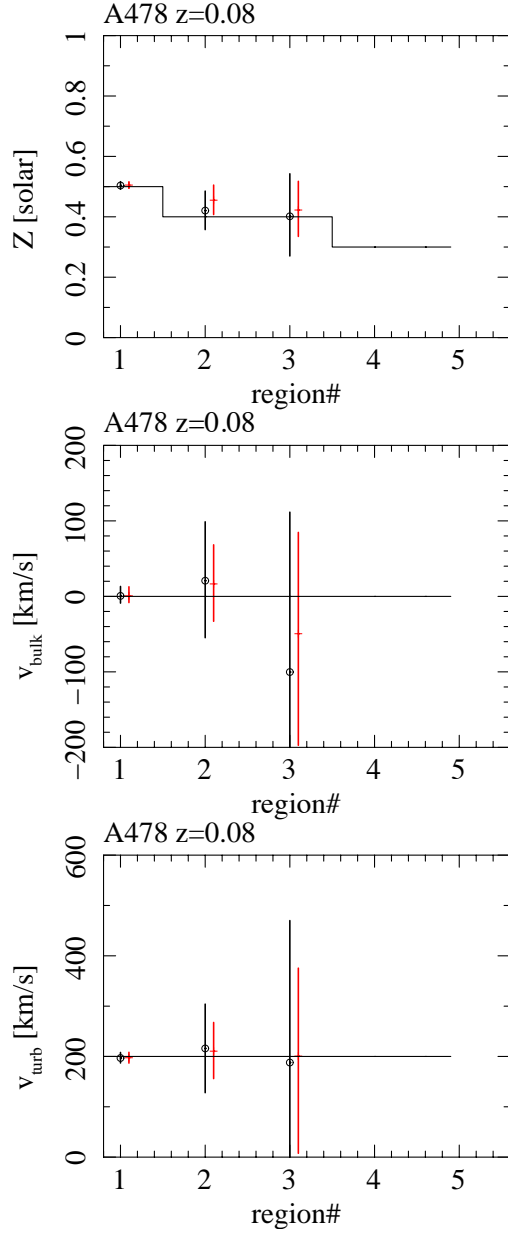


Figure 24: Same as Figure 15, but for A478 and case (a). As described in the main text, temperature is fixed at the input values listed in Table 12 for this cluster.

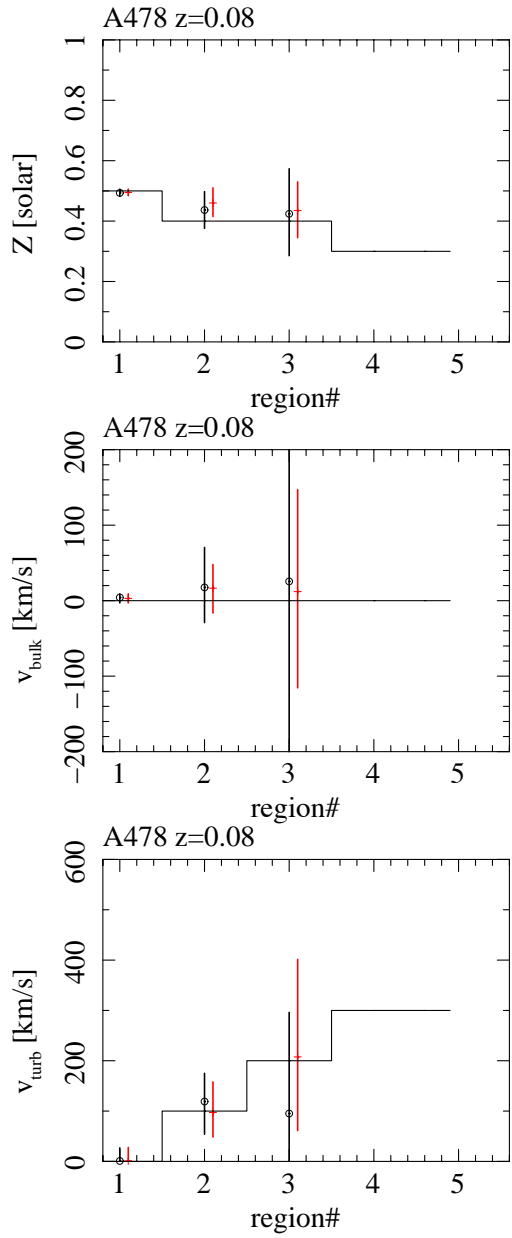


Figure 25: Same as Figure 15, but for A478 and case (b).

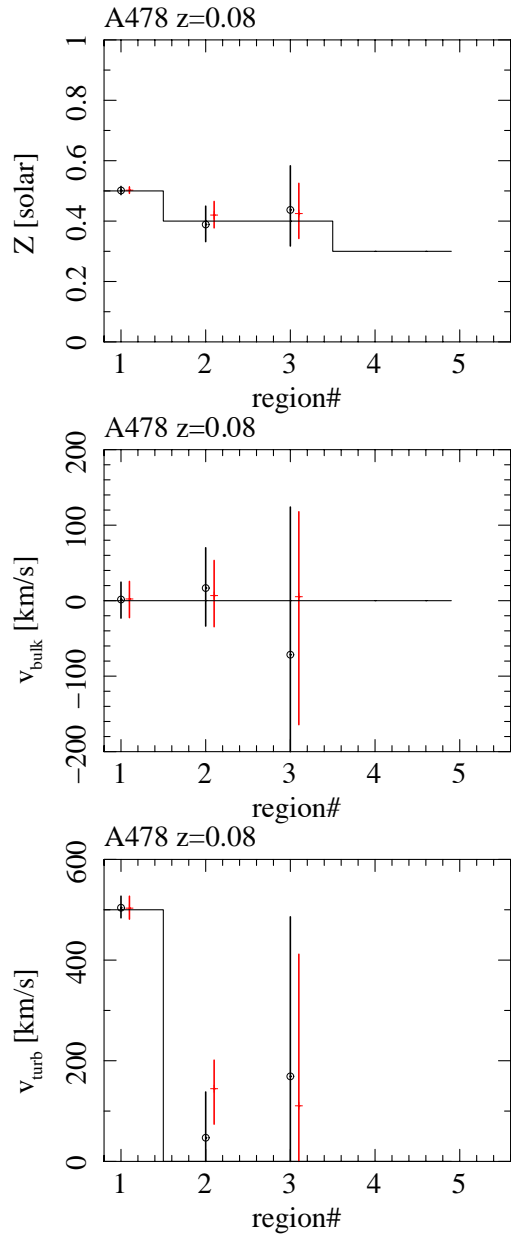


Figure 26: Same as Figure 15, but for A478 and case (c).

Table 8: Same as Table 6, but for A2199 and $N_{\text{H}} = 0.88 \times 10^{20} \text{ cm}^{-2}$.

Reg	kT [keV]	Z [solar]	Flux [$\text{erg s}^{-1} \text{ cm}^{-2}$] (0.3–10 keV)	v_{turb} [km s^{-1}]			Exposure [ks]
				(a)	(b)	(c)	
1	3.5	0.8	3×10^{-11}	200	0	500	50
2	4.2	0.8	9×10^{-12}	200	100	500	50
3	4.0	0.6	2×10^{-12}	200	200	0	150
4	3.8	0.6	7×10^{-13}	200	300	0	300
5	3.4	0.5	4×10^{-13}	200	400	0	450

Table 9: Same as Table 7, but for A2199.

	$i = 1$	$i = 2$	$i = 3$	$i = 4$	$i = 5$
$j = 1$	1.000	0.000	0.000	0.000	0.000
$j = 2$	0.125	0.834	0.040	0.000	0.000
$j = 3$	0.016	0.156	0.784	0.044	0.000
$j = 4$	0.012	0.040	0.141	0.747	0.059
$j = 5$	0.008	0.025	0.028	0.110	0.829

an independent measurement of the plasma temperature as well. These results, taken together with other data that indicate no cluster closer than Abell 2029 is more relaxed (Mantz et al., in preparation), imply that an observation of Abell 2029 at an emission-weighted radius of $0.8 \times r_{2500}$ is the optimal choice.

Of course, it is ultimately necessary to investigate non-thermal pressure support in more than one relaxed cluster. Besides testing whether or not A2029 is representative, observations of a set of such objects would constrain the scatter in non-thermal pressure support, mass and apparent baryon fraction to be expected amongst relaxed clusters. It would also give some indication of the variation of non-thermal pressure support with cluster mass. Having already established a (nearly) systematics-limited constraint with A2029, we would observe other objects with shorter exposure times that are sufficient to provide an interesting upper limit on scatter in non-thermal support. With current upper limits at about 5% (Allen et al., 2011), exposures of 250 ks (or less) per object, with formal limits on non-thermal pressure support of 1-2% per object, would be adequate for this purpose. Specific candidates for these observations include Abell 2199, which is relatively nearby and somewhat less massive than A2029, and Abell 1795, which may be more typical of objects used for cosmology than the extremely relaxed Abell 2029. Perseus, PKS0745, A478, and A496 are also plausible candidates.

4.5 Beyond Feasibility

The observations outlined above will provide sensitive first searches for dynamically important motions in the intracluster medium. As the *ASTRO-H* mission progresses, with sufficiently long exposures, we may be able to address scientific questions not discussed above. For example, simulations predict that plasma motions near the cluster core may be largely tangential (Lau et al., 2009), with systematic motions dominating random ones. This prediction could be tested by measuring velocity characteristics along multiple directions from the cluster center. Another possibility is that, with sufficiently deep observations one may be able to distinguish multiple temperature components in the plasma outside the complicated, cooling cluster cores. This could be important for understanding thermal conduction, and might also have significance for cluster mass estimates, since temperature (and therefore mass) measurements of multiphase gas with low-resolution (CCD) may be biased low (Rasia et al., 2012). Finally, a sufficiently deep and spatially dense sampling of the velocity fields in relaxed clusters like those discussed here could extend our knowledge of turbulent dissipation beyond that obtained from larger, brighter, but perhaps unique objects (Perseus, Virgo, and Coma) discussed elsewhere in this whitepaper.

Table 10: Same as Table 6, but for A1795 and $N_{\text{H}} = 1.2 \times 10^{20} \text{ cm}^{-2}$.

Reg	kT [keV]	Z [solar]	Flux [erg s ⁻¹ cm ⁻²]	v_{turb} [km s ⁻¹]			Exposure [ks]
			(0.3–10 keV)	(a)	(b)	(c)	
1	4.0	0.60	3.7×10^{-11}	200	0	500	50
2	6.0	0.35	8.4×10^{-12}	200	100	500	50
3	6.0	0.30	1.3×10^{-12}	200	300	0	200
4	5.0	0.30	4.3×10^{-13}	200	400	0	400

Table 11: Same as Table 7, but for A1795.

	$i = 1$	$i = 2$	$i = 3$	$i = 4$
$j = 1$	1.000	0.000	0.000	0.000
$j = 2$	0.184	0.790	0.026	0.000
$j = 3$	0.040	0.184	0.741	0.035
$j = 4$	0.034	0.065	0.158	0.701

Table 12: Same as Table 6, but for A478 and $N_{\text{H}} = 1.35 \times 10^{21} \text{ cm}^{-2}$.

Reg	kT [keV]	Z [solar]	Flux [erg s ⁻¹ cm ⁻²]	v_{turb} [km s ⁻¹]			Exposure [ks]
			(0.3–10 keV)	(a)	(b)	(c)	
1	5.0	0.5	5.8×10^{-11}	200	0	500	50
2	6.5	0.4	5.8×10^{-12}	200	100	0	50
3	7.5	0.4	8.0×10^{-13}	200	200	0	150
4	8.0	0.3	2.5×10^{-13}	200	300	0	300

Table 13: Same as Table 7, but for A478.

	$i = 1$	$i = 2$	$i = 3$	$i = 4$
$j = 1$	1.000	0.000	0.000	0.000
$j = 2$	0.230	0.748	0.021	0.000
$j = 3$	0.072	0.211	0.684	0.032
$j = 4$	0.078	0.107	0.189	0.626

5 Mapping Gas Flows and Turbulence in Merging Galaxy Clusters

Overview

Mergers of galaxy clusters are the most energetic events in the Universe since the Big Bang. They dissipate the vast kinetic energy of a cluster collision into thermal energy of the ICM via shocks and turbulence, while channeling some of it into magnetic fields and ultrarelativistic particles. While we do observe cluster collisions and their end result — heated ICM and synchrotron emission from cosmic-ray electrons — and have even imaged shock fronts in a handful of clusters, so far it has not been possible to study probably the most prevalent energy conversion mechanism in the ICM, which consists in the bulk flows and turbulence that they generate. The SXS will provide the first opportunity to detect and map the bulk and turbulent velocities in the ICM of nearby merging systems. The generation and dissipation of turbulence depends on a number of unknown microphysical properties of the ICM (e.g., viscosity and magnetic field structure). Mapping the bulk and turbulent velocities in well-resolved nearby mergers at different stages of unrest (e.g., Coma, A754) and across the prominent “cold fronts” in some merging clusters (A3667, A2319), combined with radio observations and numerical MHD simulations, will help to devise a detailed physical model of the ICM. This is a critically

Table 14: Summary of parameters for A2029, A2199, and Perseus.

Cluster	z	Region number	$r_{\text{reg}}/r_{2500}^{\text{a}}$	kT [keV]	Z [solar]	Flux ^b [erg s ⁻¹ cm ⁻²]	Fe-K (He,H) line ^c [cts/100ks/SXS]
A2029	0.077	1	0	6.5	0.6	6.5×10^{-11}	5107, 2049
A2029	0.077	2	0.39	7.5	0.4	7.5×10^{-12}	413, 165
A2029	0.077	3	0.79	7.5	0.3	1×10^{-12}	40, 16
A2029	0.077	“3.5” ^d	1.0	7.5	0.3	5.8×10^{-13}	25, 9
A2199	0.030	4	0.78	3.8	0.3	7×10^{-13}	35, 2
A2199	0.030	5	0.96	3.4	0.3	4×10^{-13}	19, < 1
Perseus	0.018	--	1.0	5.0	0.3	8×10^{-13}	47, 7

^a Geometrical center (not emission weighted) of simulated regions.

^b Flux at 0.3–10 keV within the SXS field of view.

^c Photon counts per 100 ks at $(6.59 - 6.74)/(1+z)$ keV and $(6.9 - 7.0)/(1+z)$ keV for the He-like and H-like Fe-K lines, respectively. No turbulent broadening is assumed. To take into account vignetting, the flux and line counts shown here should be multiplied by ~ 0.85 .

^d Midpoint between regions 3 and 4, which lies at r_{2500} .

important piece for cluster precision cosmology, one to which *ASTRO-H* can contribute.¹²

5.1 Background and Previous Studies

Clusters of galaxies form and grow via gravitational infall and accretion of surrounding matter — including smaller clusters. Cluster mergers are the most energetic events in the Universe since the Big Bang, with the total kinetic energy of the colliding subclusters reaching 10^{65} ergs. In the course of a merger, a significant portion of this energy, that carried by the gas, is dissipated (on a Gyr timescale) via shocks and turbulence in the intracluster medium (ICM). Eventually, the gas heats to a temperature that approximately corresponds to the depth of the newly formed gravitational potential well. The exact details of energy dissipation are not well understood, because they depend on complex microphysics of the intracluster plasma. This plasma is permeated by weak, tangled magnetic fields; although the magnetic pressure is of order a percent of thermal pressure and thus unlikely to be dynamically important in most of the cluster volume, such a field is more than sufficient to make the plasma collisionless and qualitatively alter its physics.

To complicate the picture, many merging clusters host giant diffuse radio halos, produced by synchrotron radiation of ultra-relativistic electrons (the Lorentz factor of $\gamma \sim 10^4$) in the cluster magnetic field (e.g., Feretti et al. 2012). These rapidly cooling (the radiative cooling time of $t_{\text{cool}} \sim 10^{7-8}$ yr) relativistic particles are mixed with thermal plasma and have to be constantly accelerated in-situ to explain the extent of the radio halos. The current thinking is that they are accelerated by scattering on magnetosonic waves generated by turbulence (e.g., Brunetti & Jones 2014). The turbulence also reorders and amplifies the intracluster magnetic field. Some MHD simulations suggest that during the violent stage of a merger, energy densities in turbulence, magnetic field and relativistic electrons may reach the same order of magnitude (e.g., ZuHone et al. 2013). Thus, complex non-hydrodynamic phenomena arising from the nature of the ICM as collisionless, magnetized plasma may have significant effects on the cluster physics and energy budget, and thus on relating the various ICM observables to the cluster total masses. The cluster masses must be known to high accuracy in order to fully realize the potential of clusters for precision cosmology (see also Sec. 4 for details).

Temperatures and densities of the thermal ICM component are readily derived from the X-ray spectro-imaging. With the existing and past X-ray instruments, we’ve observed many cluster collisions and their end result — the irregularly distributed, nonuniformly heated intracluster medium. With recent high-resolution

¹²Coordinators of this section: M. Markevitch, H. Akamatsu

X-ray imaging, we even caught sight of a few shock fronts that quickly pass across the cluster collision site (e.g., in the Bullet cluster, A520, A754, A2146 and a few others). Detailed studies of shock fronts provide a merger velocity in the plane of the sky, and for well-studied shocks, constrained the electron-proton equilibration timescale (Markevitch 2006; Russell et al. 2012). In many mergers, we’ve also observed “cold fronts,” or sharp contact discontinuities. They are unresolved even with *Chandra*, providing proof that the intracluster plasma is indeed collisionless. They also appear stable, potentially indirectly constraining the effective ICM viscosity (Markevitch & Vikhlinin 2007).

A critical piece of the puzzle that has been missing so far is direct observations of the gas motions, both streaming and turbulent. Both types of motions are expected to exist (and often coexist) at various stages of cluster mergers. The line-of-sight bulk (or streaming) gas velocity would provide the missing “third dimension” for understanding the geometry and velocity of a cluster merger. Turbulence should cascade from the large linear scales of the merger down to the unknown damping scale, which is determined by the ICM microphysics. This is where *ASTRO-H* can make some of its most important scientific contributions.

5.2 Prospects and Strategy

By characterizing the bulk velocities and turbulence in merging clusters and using these measurements, in combination with the X-ray imaging and radio data, as input for detailed numerical MHD simulations, we hope to greatly improve our understanding of the various physical processes in the ICM. The superb energy resolution of SXS, and its moderate angular resolution, will enable accurate, spatially resolved measurements of line broadening and shifts for the 6.7 keV Fe-K line for many nearby clusters. Line shifts reveal variations of the line-of-sight bulk velocities of the ICM, while line broadening measures turbulence on linear scales smaller than the beam size. Strictly speaking, lines can be broadened by any line-of-sight velocity difference within the beam size. “True” turbulence, with random motions on all linear scales following a certain power spectrum, can be distinguished from, e.g., a superposition of oppositely directed streams by the shape of the broadened line. When this distinction is not clear-cut, we will have to rely on reasonable assumptions and hydrodynamic simulations. For example, if we *don’t* detect turbulence (or random motions) on small scales in clusters, but do detect line-of-sight (LOS) velocity gradients on larger scales, this would immediately tell us that plasma viscosity should be high. For another example, the strength of turbulence in the area of the cluster radio halos will constrain theories of cosmic-ray acceleration. If high levels of turbulence (e.g., prevalent near-sonic velocity dispersions) are detected, it would mean that mechanical energy is a significant fraction of the total energy budget. This would provide important input for cosmological (as well as idealized) cluster simulations.

These measurements will be expensive in terms of the exposures required. Merging clusters usually do not have cool cores, and their surface brightness is relatively low even at their centers, typically requiring over 100 ks per pointing to accumulate enough photons for interesting line constraints (as we will see below). Furthermore, given the 1.1’–1.3’ HPD angular resolution, the 3’×3’ SXS FOV contains only ~ 2–4 independent imaging pixels, requiring mosaics to cover an interesting range of angular scales for velocity mapping.

These observations have two broad goals. The easier one is to map the line-of-sight (LOS) gas velocities in a merger, which is critical for the reconstruction of the geometry and dynamical stage of a particular merger, in combination with all other existing data (X-ray, optical, radio) and hydro simulations. A more difficult task is to characterize the power spectrum of turbulence, which could be used as input for high-precision MHD simulations to constrain the ICM microphysics. For the latter goal, one may prefer clusters without cool cores, despite their lower surface brightness, because cool cores always come with physical complications such as steep entropy gradients (which are very convectively stable and thus make the turbulence develop preferentially in radial shells instead of isotropically), and moving bubbles from the central AGN activity. Because the range of scales between the size of the PSF and the size of the bright cluster region accessible for measurements is small even for the nearest systems, it may be best to select the least contaminated examples; Coma may be the best candidate.

For mergers at a more violent stage, it would be extremely interesting to observe A3667, A754, and possibly A2256. All three are famous mergers with many past attempts to reconstruct their merger geometry — on

which we will build using the SXS velocity data. These clusters are expected to have large gradients of LOS velocity as well as high levels of turbulence.

In addition, A3667 has a spectacularly sharp “cold front” (Vikhlinin et al. 2001), a contact discontinuity in the gas that enables some unique ICM physics tests on its own (Markevitch & Vikhlinin 2007). The gas density jump is unresolved even with the *Chandra* $1'' \approx 1$ kpc resolution, while the shape of the front hints at the onset of hydrodynamic instabilities. Another such high-contrast cold front is found in A2319. Cold fronts arise either from subcluster stripping by ram pressure, or from “sloshing” of the low-entropy gas in a disturbed gravitational potential well (Markevitch & Vikhlinin 2007). The fronts in A3667 and A2319 can be of either origin, although the initial interpretation for A3667 was stripping. In the stripping scenario, bulk motions of the subclusters are mostly in the plane of the sky, while in the sloshing case, we may see a near-sonic flow along the LOS inside the front. SXS measurements would resolve this ambiguity, providing solid basis for the derivation of physical constraints from these cold fronts.

Among the clusters that we consider, Coma, A754 and A2319 have giant radio halos (while A2256 has a faint halo and a bright “relic” near its core, and A3667 has a pair of bright peripheral relics). Simultaneous observations with HXI may yield interesting constraints on the cluster nonthermal matter components. The relativistic electrons responsible for the synchrotron radio halos are also expected to produce inverse Compton emission at high X-ray energies (upscattering the CMB photons); their detection at both wavebands would allow one to disentangle the magnetic field strength and the density of the relativistic electrons (the radio observations only give a product of the electron density and B^2 , where B is the highly uncertain magnetic field strength; for more details, see Sec. 6).

Table 15: Cluster Sample

Name	z	kT [keV]	kpc/3' ($h = 0.7$)
Coma	0.023	8	84
A3667	0.053	7	185
A754	0.054	9	190
A2319	0.056	9	194
A2256	0.058	7	202

5.3 Targets and Feasibility

For mapping the LOS velocity and turbulent broadening, we will mosaic the clusters and derive spectra in $2' \times 2'$ or $3' \times 3'$ regions. For a relatively flat brightness distribution such as that in the proposed clusters (except for cold fronts in A3667 and A2319 and the shock front in A754, see below), such a pixel size allows us to disregard PSF scattering – the spectra will be largely uncorrelated.

We aim at a minimum of 500 counts in the 6.7 keV Fe-K line for each spectrum. The statistical accuracies of the line shift and turbulent broadening strongly depend on the line width (Figure 5). For the expected high values of turbulence with the LOS velocity dispersion of $v_{\text{turb}} \sim 300 - 1000$ km s $^{-1}$ (corresponding to the turbulence Mach number $M_{\text{ID}} \equiv v_{\text{turb}}/c_s \sim 0.2 - 0.6$, where c_s is the sound speed), we will obtain 90% statistical uncertainties on line position of 50 (160) km s $^{-1}$, and uncertainties on v_{turb} of 60 (170) km s $^{-1}$, for $v_{\text{turb}} = 300$ (1000) km s $^{-1}$, respectively, by fitting both parameters and the line normalization simultaneously. These constraints conservatively come from the He-like line alone, while in these hot clusters the H-like line will slightly improve the accuracy. With such statistical accuracy, the line shift measurement will be dominated by the systematic uncertainty of SXS gain stability (2.0 eV or 100 km s $^{-1}$ at 90%; see also Figure 5) at $v_{\text{turb}} \lesssim 500$ km s $^{-1}$. At these levels of turbulence, the line broadening measurement will be governed by statistics — the expected uncertainty on the line response is negligible at $v_{\text{turb}} \gtrsim 100$ km s $^{-1}$ (Appendix A).

The parameters of clusters that we find promising for the velocity and turbulent mapping are given in Table

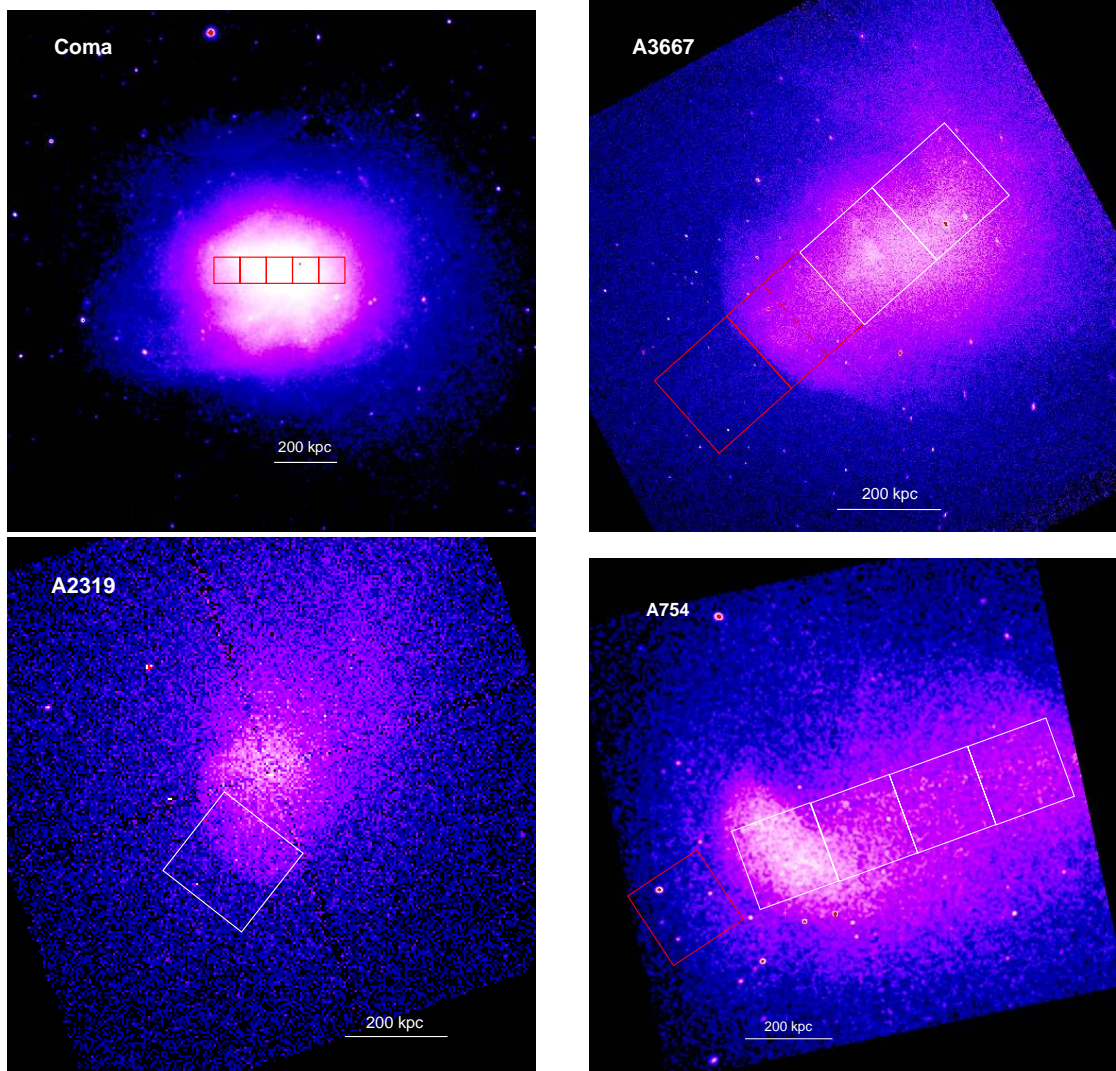


Figure 27: X-ray images of Coma, A754, A3667 and A2319 with the proposed $3' \times 3'$ regions overlaid. The Coma image is from *XMM-Newton* and the rest is from *Chandra*. Red squares in the A3667 panel show the pointings inside and outside the prominent cold front, which are higher-priority than the rest for this cluster (white regions). Red square in A754 panel shows a post-shock region, which is the only one that can be resolved with SXS, but requires an unrealistically long exposure. White regions are higher-priority pointings for each cluster.

5.3.1 Coma

Coma is the nearest bright cluster that appears to have undergone a merger fairly recently. It offers the best chance to characterize the turbulence on a range of scales, free of complications related to AGN activity. Coma has a large, near-constant density core free of strong entropy gradients and stratification, where turbulence should develop in 3D in an isotropic, qualitatively simple way. On the other hand, the constant core also unavoidably means strong LOS projection effects, which will have to be addressed in a statistical manner using hydro simulations. One possible observational setup is a “transect” of 5 contiguous pointings (Figure 27) spanning the cluster core. It will allow measurements of velocities, line broadening, and their spatial correlations on scales $2' - 15'$ (50 – 400 kpc). The largest offsets will constrain the cluster-scale rotation, which is a very interesting quantity. The differences in velocities as a function of distance may be quantified by a “structure function”, $SF(r) \equiv \langle (v(x+r) - v(x))^2 \rangle$, where the brackets denote averaging over pairs of directions separated by r in the sky (e.g., Zhuravleva et al. 2012). The structure function has a one-to-one correspondence to a 3D power spectrum of turbulence.

A simulation that includes the statistical and systematic errors on velocities from the expected 500 line counts per $3' \times 3'$ pointing is shown in Figure 28 (ZuHone & Markevitch 2014, in prep.). The simulation assumed an adiabatic, beta-model cluster gas distribution, and considered several values of the turbulence Mach number as well as various deviations of the turbulent power spectrum from the pure Kolmogorov power law. In particular, we considered an exponential cutoff at various small linear scales (representing a dissipation scale of the turbulent cascade) and a cutoff at various large scales (representing a “driving scale” of the cascade). The SF curves in Figure 28 are normalized by the average velocity dispersion, in order to show what extra information can be extracted from the Coma offset pointings once the central pointing is observed and the presence of the turbulence and its strength are established.

In the core of a typical hot, non-cool-core cluster such as Coma, the ICM collisional mean free path is of order 10 kpc; if turbulence dissipates at this scale, its power spectrum will start turning over on scales several times that, which for Coma is resolvable with *ASTRO-H*. However, the upper-left panel of Figure 28 shows that we do not expect to be able to detect the presence of a dissipation scale (unless it is implausibly big). Without the inclusion of the random velocity measurement errors, the SF curves for different dissipation cutoffs do differ significantly (ZuHone & Markevitch 2014, in prep.), but once those errors are included, they dominate the small-scale power and overwhelm the intrinsic power spectrum differences. However, the SF curves for different large-scale cutoffs (the turbulence driving scales) can easily be distinguished, even for moderate $M_{1D} \approx 0.2$. The lower-right panel (labeled “big cross”) shows the measured SF curves for a different pointing setup, where the two $3'$ offsets were replaced with two extra $6'$ offsets to form a cross. The accuracy of the large-scale variations is improved (at the expense of the intermediate scales; the smallest-scale data points come from the differences measured within each $3' \times 3'$ FOV); this may be a better setup for studying the shape of the power spectrum on large scales.

Exposure times required to collect 500 line counts from each $3' \times 3'$ pointing in the “strip” setup are (left to right) 150, 110, 100, 100, 150 ks, for a total of 610 ks. These early measurements, depending on their results, will provide a pilot dataset of a possible future “key project” to map the whole Coma core, because the accuracy of the power spectrum constraints increases proportionally to the number of pairs of pointings at a given angular separation.

5.3.2 A3667

A3667 is a classic cold front cluster. Large-scale velocity mapping in regions shown in Figure 27 will require 200, 180, 100, and 120 ks, for a total of 600 ks. The two pointings shown in red will allow a detailed study of the cold front (a strikingly sharp edge in X-ray brightness shown in Figure 29), which we simulated in detail.

For a high-contrast feature such as this cold front, PSF scattering will have a significant effect. Based on the *Chandra* image (and using the PSF version from January 2013), we estimated the scattered contribution from

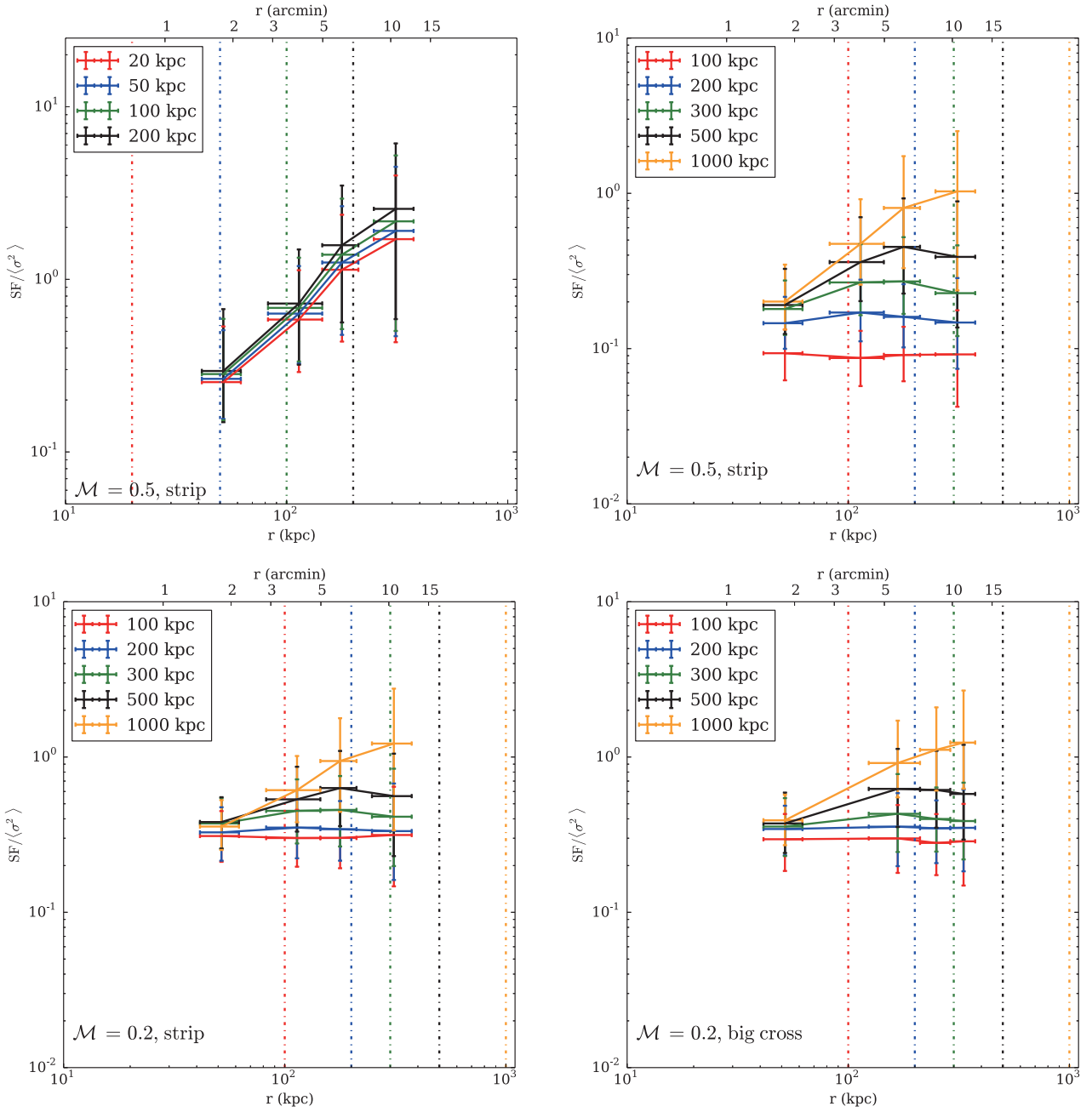


Figure 28: Simulated structure functions for Coma, normalized to the average velocity dispersion. The measurement errors on velocities (statistical and systematic) are included. Panels labeled “Strip” are for the pointing setup shown in the Coma panel of Figure 27, while that marked “Big cross” is for a setup in which the small offsets are replaced with $6'$ offsets in the perpendicular direction. Errors are 68%. The turbulence Mach number ($M_{\text{ID}} = 0.2$ or 0.5) is given in labels. The upper-left panel is for a Kolmogorov power spectrum with an exponential cutoff at small linear scales (different scales are shown by different colors), while other panels are for the cutoff at large linear scales. A small-scale cutoff is not detectable because of the dominance of the statistical uncertainties of the velocities, while the presence or absence of large-scale turbulent eddies can be detected.

Table 16: A3667. Gas properties for the cold front based on *Chandra* and *XMM-Newton*.

Region	kT [keV]	Abundance [solar]	Flux ^a [erg cm ⁻² s ⁻¹]	Fe line photons ^b
Inside	4.5	0.55	2.50×10^{-13}	600
Outside	7.7	0.30	0.45×10^{-13}	180

^a 0.5–2.0 keV

^b 6.25 – 6.4 keV counts in $1.5' \times 3'$ inside region and $3' \times 3'$ outside region; 200 ks exposure; not including PSF scattering

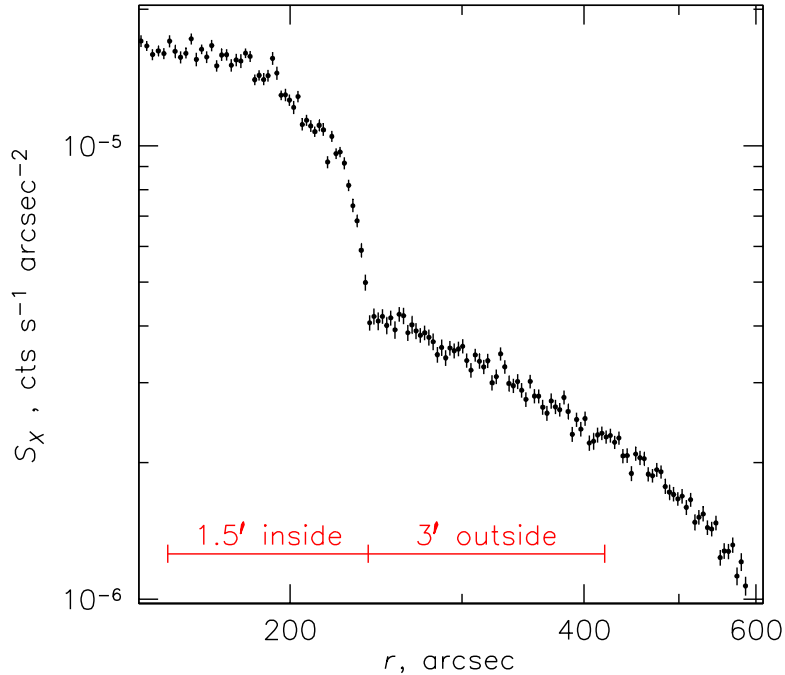


Figure 29: *Chandra* X-ray brightness profile across the sharp cold front in A3667. The proposed observations will probe the gas properties across the front. Simulated spectra discussed in Tables 16 and 17 correspond to the radial ranges shown in red.

the bright $1.5' \times 3'$ region inside the cold front (half of the red square shown in Figure 27 adjacent to the front; see also Figure 29) into the $3' \times 3'$ region outside the front (the leftmost red square in Figure 27) to be 30% of the total line photons in that spectrum. For error estimates, it was included as an additional thermal component in the fit for the outside region.

Table 16 summarizes the X-ray quantities around the cold front, for the “inside” and “outside” regions described above. For the gas outside the front, we have assumed (reasonably conservatively) a turbulent broadening of $v_{\text{turb}} = 500 \text{ km s}^{-1}$. For the gas *inside* the front, we tried two scenarios — (a) that gas has no LOS velocity difference from the gas outside the front, but it does have a velocity dispersion (hereafter called “turbulence” for simplicity) of $v_{\text{turb}} = 1000 \text{ km s}^{-1}$. This scenario represents a “stripping” cold front, where this broadening is due to the gas inside the front flowing in opposite directions along the LOS. Scenario (b) is for the gas on the inside to have no turbulence, but to move along the LOS with $v = 1000 \text{ km s}^{-1}$ – this represents a “sloshing” front geometry. (In reality, the latter scenario can also have turbulence inside the front; as long as we can detect the LOS velocity difference for the two regions, this would still point to a “sloshing” geometry.)

Figure 30 shows the simulated spectra for the *outside* region for these two scenarios, illustrating the PSF-scattered contribution from the brighter side of the front. Table 17 shows the resulting LOS velocity and broadening accuracies from two 200 ks exposures straddling the front, for the above two assumptions. For these fits, the whole spectrum was used, that is, both the He and H-like lines contributed to the constraints; all

Table 17: A3667. Statistical accuracy (1σ) for velocities and velocity dispersions from two 200 ks front pointings, for scenarios (a) and (b) for the state of gas inside the front. In both cases, the gas outside has turbulent broadening with $v_{\text{turb}} = 500 \text{ km s}^{-1}$.

Region	$v_{\text{bulk}} [\text{km s}^{-1}]$	$v_{\text{turb}} [\text{km s}^{-1}]$
Constraints for gas inside:		
(a) $v_{\text{bulk}} = 0, v_{\text{turb}}^{\text{inside}} = 1000 \text{ km s}^{-1}$...	1005 ± 23
(b) $v_{\text{bulk}} = 1000 \text{ km s}^{-1}, v_{\text{turb}}^{\text{inside}} = 0$	± 43	...
Constraints for gas outside:		
(a) $v_{\text{bulk}} = 0, v_{\text{turb}}^{\text{inside}} = 1000 \text{ km s}^{-1}$	± 100	420 ± 150
(b) $v_{\text{bulk}} = 1000 \text{ km s}^{-1}, v_{\text{turb}}^{\text{inside}} = 0$	± 136	571 ± 143

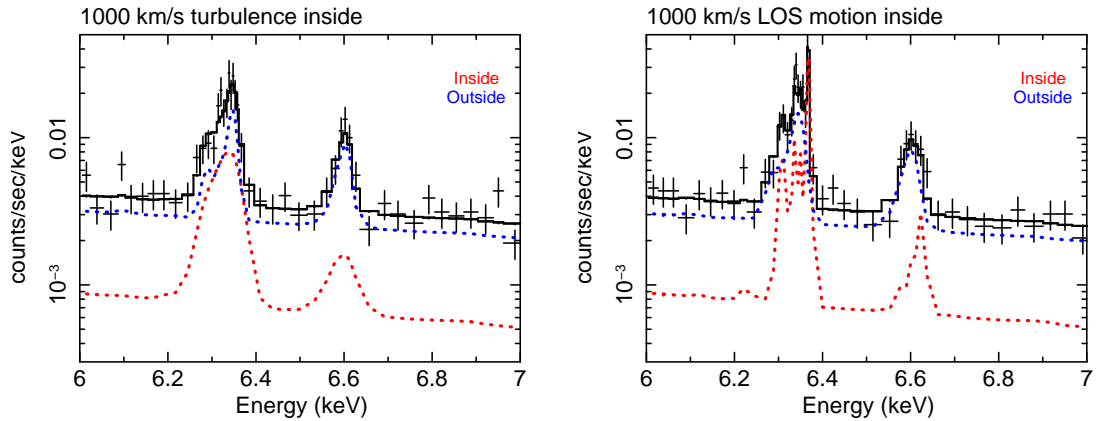


Figure 30: Simulated spectra from the $3' \times 3'$ region *outside* the cold front in A3667 (see Figure 27), for a 200 ks exposure. Red lines show contamination from the gas inside the front due to PSF scattering; blue line shows the contribution from the underlying region in the sky. Two panes correspond to two assumptions about the gas inside the front (see text).

parameters, including both temperatures and abundances, were free. Systematic uncertainties on gain accuracy are similar to the statistical uncertainties for LOS velocities for both regions; for line broadening, the statistical uncertainties dominate over both the systematic resolution uncertainty and the T_{ion} uncertainty. With two 200 ks exposures, we can obtain interesting constraints on velocities and even constrain turbulence outside the front.

5.3.3 A2319

A2319 features a prominent cold front with as high a gas density jump as in A3667, but located in a brighter region of the cluster. We simulated the velocity and line broadening constraints that can be obtained from one 150 ks exposure straddling the front (see Figure 27). PSF scattering was included based on *Chandra* image. The contaminant was included in the fit for the outside region as an additional thermal component; it contributes 35% of the total emission in the outside spectrum. Parameters for both components were varied to determine the uncertainties for the outside region. For this simulation, we assumed a sonic relative LOS velocity between the two components (1650 km s^{-1}) and a rather extreme, $M_{\text{1D}} \approx 1$ turbulent broadening for the gas inside the front in scenario (a) or outside the front in scenario (b). The resulting constraints are given in Table 18, and simulated spectra for scenario (b) are shown in Figure 31. The constraints are interesting and can clearly distinguish these two extreme cases, though, as expected from such small numbers of line photons (Table 18), the errors are large and less-extreme motions will not be easy to constrain. This underscores the need to expose well to collect at least ~ 500 line counts for robust measurements of gas dynamics.

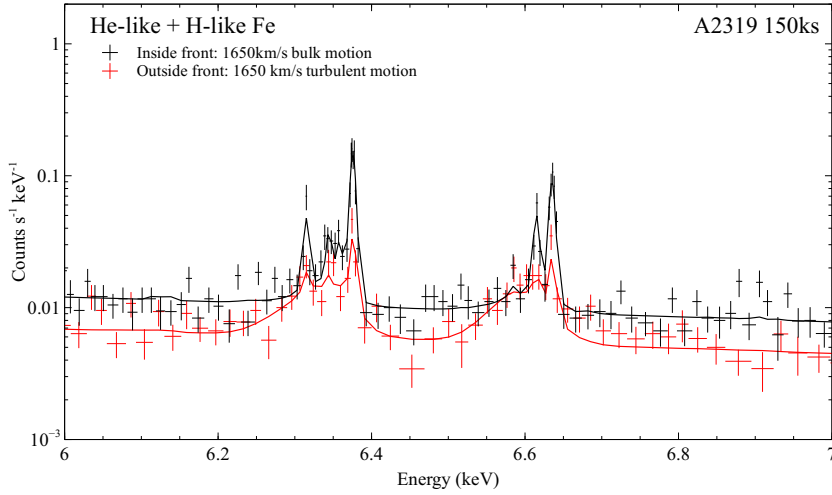


Figure 31: Simulated spectra from the $1.5' \times 3'$ regions inside and outside the cold front in A2319 (two halves of the SXS FOV shown in Figure 27), for a 150 ks exposure and scenario (b) with turbulent broadening outside the cold front. Black and red lines show the inside and outside regions, respectively, and include both the intrinsic and PSF-scattered components.

Table 18: A2319. Constraints on velocities for $1.5' \times 3'$ regions and exposure time 150 ks. Errors are 1σ . Gain stability for systematic uncertainty is 1 eV. Line counts (6.3 – 6.4 keV) include continuum but exclude PSF scattered component. Scenario (a) assumes turbulence inside the cold front and none outside, whereas (b) assumes turbulence outside. In both models, there is a LOS velocity difference of the gas inside the front in the reference frame of the gas outside.

	scenario (a)		scenario (b)	
	Inside	Outside	Inside	Outside
v_{bulk} [km s $^{-1}$]	1640^{+24}_{-21}	28 ± 160	1635 ± 10	140^{+320}_{-290}
$v_{\text{bulk sys. err.}}$ [km s $^{-1}$]	45	45	45	45
v_{turb} [km s $^{-1}$]	1320^{+140}_{-180}	< 47	< 29	1500^{+280}_{-240}
$v_{\text{turb sys. err.}}$ [km s $^{-1}$]	1	60	60	1
He-like Fe counts	325	160	400	120

5.3.4 A754

This is a well-studied merger with a $M = 1.6$ shock front (Macario et al. 2010). Our estimate shows that it is not feasible to study the post-shock gas (see §5.4). From detailed examination of the available X-ray data, one may expect the bright, cool elongated “core” to have a different LOS velocity from the rest of the cluster (it appears to be a “sloshing” core disrupted by a violent cluster collision). A transect shown by white squares in Figure 27 will require the following exposures: 100, 170, 220, 240 ks, for a total of 730 ks.

5.3.5 A2256

A2256 is another famous merger studied by all the X-ray missions. Tamura et al. (2011) reported a LOS velocity gradient so large that it was detectable with *Suzaku* even with a CCD resolution. A2256 would thus be a very promising target for velocity mapping. However, its peak surface brightness is half that of Coma, so exposures will have to be very long (~ 200 ks in the center and several times longer in the region of the large velocity differences).

5.4 Beyond Feasibility

Shock fronts are unique tools for studying the ICM microphysics. However, none of the known shocks will be resolved by *ASTRO-H*. The most prominent one in the Bullet cluster is only 30'' away from the bright cool bullet; A520 and A2146 have similarly small separations from their bright driver subclusters.

A754 has a shock front observed by *ROSAT* and *Chandra* (Krivonos et al. 2003; Macario et al. 2011), which is better separated from the bright core than the more famous ones. However, our estimate showed that even in this nearby cluster, PSF scattering from the bright cluster core 2 – 3' away will dominate the flux in the post-shock region. For example, in a 150 ks exposure shown by red square in Figure 27, we will collect a total of 190 line counts, of which only 50 counts originate in the underlying post-shock region and the rest is scattered from the outside. Such a large scattered contribution combined with low brightness makes it impossible to derive any constraints for that region.

6 High-energy Processes

Overview

The Hard X-ray Imager (HXI) on board *ASTRO-H*, together with the foregoing *NuSTAR* mission, will comprise the first generation of hard X-ray instruments with imaging capability in the 5–80 keV energy band. The prime targets of HXI include the inverse-Compton radiation by non-thermal electrons in galaxy clusters and the thermal emission from very hot ($kT \gg 10$ keV) intracluster gas. The former is of particular importance for revealing the origin of the ultrarelativistic particles, which are presently observed only in the radio bands; it will also provide information on the strength and structure of the intracluster magnetic fields. The latter is critical for detailed understanding of the heating mechanism of the intracluster plasma as well as assessing correctly the total pressure support in clusters. A major advantage of *ASTRO-H* will be its wide spectral coverage, which plays a key role in disentangling a number of emission components including backgrounds; the HXI data will be obtained simultaneously with those of the Soft X-ray Spectrometer (SXS) and the Soft X-ray Imager (SXI) at 0.3 – 12 keV. We also address meaningful lessons from early operations of *NuSTAR*.¹³

6.1 Background and Previous Studies

Besides being luminous sources of thermal X-ray emission, galaxy clusters often harbor faint diffuse radio sources. "Giant radio halos" and "minihalos" are unpolarized sources found in merging clusters and in cluster cool cores, respectively. Some clusters also exhibit "radio relics" – elongated, strongly polarized sources in the periphery (for a review see Feretti et al. 2012). This strongly suggests that there is a substantial population of relativistic particles. However, the details of the energy distribution of such particles are not fully understood, since there is an inherent degeneracy with the strength of the magnetic fields and their distribution, when made on the basis of the radio data alone. Furthermore, the process of electrons being accelerated to the relativistic energies required to account for the radio emission is far from clear. Peripheral relics can plausibly be produced by Fermi acceleration on merger shocks, but the mechanism responsible for the giant halos and minihalos has to act simultaneously throughout the cluster, because the radiative cooling time of such energetic electrons (10^{7-8} yr) is much shorter than their diffusion or advection time across the halo (e.g., Petrosian 2001), so they have to be produced in-situ. Several physical mechanisms have been proposed (for a review see Brunetti & Jones 2014).

The very same electrons that generate the radio emission must also inverse-Compton scatter any ambient radiation. This provides an interesting opportunity to determine the magnetic field strength and the number density of relativistic electrons separately (Harris & Romanishin 1974), taking advantage of the fact that the radio synchrotron emission is proportional to the cosmic ray density times the energy density of the magnetic field, while inverse Compton emission is independent on the magnetic field and is instead proportional to the

¹³Coordinators of this section: M. Kawaharada, G. Madejski

energy density of the background radiation. There are two, possibly three sources of such ambient photons with significant energy density. One is the Cosmic Microwave Background, with well-determined energy density. Another is the cluster's own thermal X-ray emission, which is well-measured in clusters from sensitive soft X-ray data, with temperatures of a few up to ~ 15 keV (and possibly even more; e.g., Markevitch et al. 2006). These two photon fields should be Compton-upscattered by the ultrarelativistic electrons to the hard X-ray and γ -ray bands, respectively. (The third source is starlight from the member galaxies, but while within the member galaxies it might be appreciable, its energy density in clusters is significantly lower.)

Since these two sources of photon fields in clusters are reasonably well determined (both the co-moving CMB intensity, and cluster X-ray luminosity are robustly measured), the detection of inverse Compton radiation should break the degeneracy between the distribution of relativistic electrons and the strength of the magnetic field, allowing the determination of both quantities separately, and possibly even measuring the spatial structure of the field. It is important to note that even a sensitive *non-detection* has a profound impact on cluster studies, since at the sensitivity of the current imaging hard X-ray instruments (*ASTRO-H* HXI, but also *NuSTAR*), those upper limits on non-thermal flux correspond to *lower* limits on the strength of magnetic field (e.g. Nakazawa et al. 2009). Furthermore, the robust determination of the distribution of relativistic particles is important in determining the cluster masses, which are essential when one wishes to use clusters as tools for precision cosmology. This is because the non-thermal particles provide an additional source of pressure, which needs to be considered in derivation of cluster masses, traditionally relying on an assumption of hydrostatic equilibrium. In fact, a deviation from hydrostatic equilibrium has been reported in some clusters (e.g. Kawaharada et al. 2010; Ichikawa et al. 2013; van der Linden et al. 2014), by comparing the thermal pressure and the total pressure derived from lensing analysis; the relativistic components, including the magnetic fields and cosmic rays, are possible reasons, along with turbulence and the effects of asphericity.

Gamma-ray measurements so far have not revealed any emission from clusters. This is possibly due to a limited sensitivity of instruments, but also due to the fact that the inverse Compton scattering of soft X-rays operates at least partially in the Klein-Nishina regime. The best limits so far were from the *Fermi* LAT instrument (Ackermann et al. 2010). The hard X-rays offer a promising probe of the inverse-Compton radiation by relativistic electrons. The non-thermal emission is expected to have a power-law shape, as inferred from the radio spectra. However, the *thermal* cluster emission is so dominant that the *non-thermal* emission is very difficult to disentangle (e.g., Million & Allen 2009; Wik et al. 2014). Further complication arises from the fact that the clusters' X-ray emission cannot be described by a single temperature (see, e.g., Peterson and Fabian 2006; Anderson et al. 2009). Such multi-temperature structure can very easily mask the power-law component potentially present in addition to the thermal emission *within* the soft X-ray band.

The presence of very hot ($kT \gg 10$ keV) gas has in fact been inferred in some merging clusters such as RX J1347.5–1145 (Kitayama et al. 2004; Ota et al. 2008) and A3667 (Nakazawa et al. 2009), whereas definite distinction from the non-thermal emission is yet to be made. Its emission measure and spatial distribution are uncertain, and it may significantly contribute to the total ICM pressure, while largely evading detection by previous X-ray instruments that only cover energies below 10 keV. A wider spectral coverage is crucial for disentangling this component from the non-thermal emission and various background components. Hard X-ray imaging should also play a complementary role in revealing the nature of the hot gas to spatially resolved Sunyaev-Zel'dovich effect observations (for a review see Kitayama 2014).

6.2 Prospects and Strategy

The hard X-ray band is suitable for detecting the inverse-Compton radiation as well as the thermal emission from gas with $kT \gg 10$ keV. The caveats are much higher levels of contamination from the cosmic X-ray background (CXB) and non-X-ray (or particle) background (NXB) than the soft X-ray band. In fact, some of the previous claims of detection of the cluster nonthermal emission from collimated hard X-ray instruments (workhorses for the hard X-ray astronomy before the advent of focusing hard X-ray telescopes) have been controversial (e.g., Fusco-Femiano et al. 2000; Rephaeli et al. 2006; Petrosian et al. 2006; Ajello et al. 2010). Convincing and conclusive hard X-ray measurements require both imaging capability and an improved control

of the backgrounds.

ASTRO-H is one of the very first observatories featuring such focusing hard X-ray instruments. The Hard X-ray Imager (HXI) is sensitive up to ~ 80 keV, well beyond the tail of clusters' thermal spectrum. Since the HXI is co-aligned with the SXS, the data will be taken by both instruments and, fortuitously, there is a strong synergy between the SXS, SXI and HXI regarding cluster observations. One of the key requirements is accurate cross-calibration between the soft and hard X-ray instruments, as is also the case for many other joint soft and hard X-ray observations.

There are a few important cases where the non-thermal emission in a cluster arises in regions with relatively weak thermal soft X-ray emission. The striking radio relic at the northwestern periphery of A3667 shows relatively strong radio emission, but weak soft X-ray emission. Its radio emission exhibits a sharp linear edge, which would make the detection of the accompanying nonthermal X-ray emission easier, since it allows for the search via positional coincidence. In the central regions of A3667, the very hot gas could be detected with the combined analysis of HXI and SXI. The radio halo in the Coma cluster is another major object from which non-thermal emission is expected. These would be observations for which the HXI science provides the main driver in the early phase of *ASTRO-H* observations.

The scientific goals addressed via the HXI observations are also complementary to those discussed in Section 4. There, the main tool used for studies of the non-thermal pressure is the high resolution X-ray spectroscopy with the SXS, while here, the expected impact of the HXI observations is discussed. However, ultimately, it is the joint evidence from both instruments that will be most valuable in studying the departure from a simple thermal picture of clusters. One example regards the effect of the population of non-thermal electrons on the line emission in the soft X-ray band (e.g. Kaastra et al. 2009). Those joint studies should address one important and overarching goal: how the non-thermal / high energy processes in clusters affect the reliability of determination of cluster mass, and thus applicability of X-ray observations of clusters to cosmology.

6.3 Targets and Feasibility

6.3.1 The NW relic of Abell 3667

The North West (NW) radio relic of A3667 (Röttgering et al. 1997; see Figure 2 of Finoguenov et al. 2010) is the brightest such object in the sky, which makes it one of the best targets for the detection of inverse Compton radiation in hard X-rays. Its angular size also perfectly matches the HXI FOV and resolution. From soft X-ray observations by *XMM-Newton* (Finoguenov et al. 2010), it is difficult to determine if the X-ray emission associated with this relic is thermal or nonthermal. Using *Suzaku* data, Nakazawa et al. (2009) reported an upper limit on the non-thermal flux from the *entire* cluster region as 7.3×10^{-13} erg s $^{-1}$ cm $^{-2}$ at 10–40 keV and the corresponding lower limit on the magnetic field of $1.6 \mu\text{G}$. The upper limit on the surface brightness is about 1.8×10^{-15} erg s $^{-1}$ cm $^{-2}$ arcmin $^{-2}$ (10–40 keV) in the NW relic region.

In our simulations for HXI, we extrapolate the soft X-ray emission observed by *XMM-Newton* to hard X-rays assuming a power-law spectrum with the photon index $\Gamma = 2.0$, yielding the relic surface brightness of 1.7×10^{-15} erg s $^{-1}$ cm $^{-2}$ arcmin $^{-2}$ in the 10–40 keV band. Note that this value lies just below the *Suzaku* upper limit mentioned above. We also assume that the X-ray brightness traces the spatial distribution of the radio synchrotron emission. Figure 32 shows that, with an exposure time of 200 ks, the assumed brightness edge can be detected and HXI plays a crucial role in identifying the nonthermal spectrum. For clarity, we also plot the projected emission profile onto the Y-axis in Figure 33, exhibiting that the non-thermal emission exceeds the background inside the radio edge.

Accurate prediction of the sensitivity of HXI before launch is challenging since it depends largely on various systematic effects including the background levels in orbit. Current estimates are that the sensitivity will be better than that of *Suzaku* by about a factor of ~ 6 (see Sec. 6.3.3 for details). If we do not detect the inverse Compton signal from this radio relic with such sensitivity, a combination of its radio brightness and our X-ray upper limit will yield a lower limit on the strength of the magnetic field $B \gtrsim 4 \mu\text{G}$. Such a strong magnetic field would be very unexpected so far away from the cluster center.

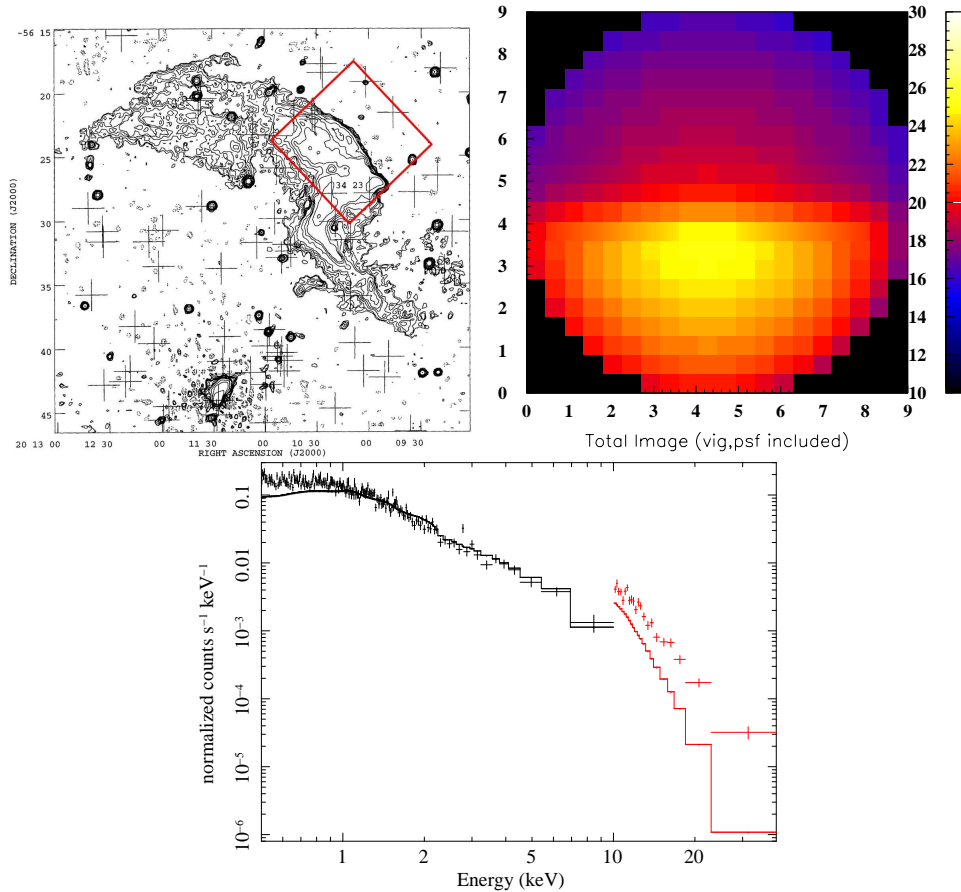


Figure 32: Simulated observations of A3667 North West relic for a 200 ks exposure, including the non-thermal emission with $\Gamma = 2.0$ as described in the text. *Top left:* The HXI field of view ($9' \times 9'$) which covers the NW relic and its edge (red box), overlaid on the 20-cm ATCA image (Röttgering et al. 1997). *Top right:* Simulated HXI raw image (NXB and CXB are included) of the potential sharp edge in hard X-ray band. The image is binned to 20×20 pixels. The color scale is in counts per pixel and indicated in the legend on the right. The PSF and vignetting effects are taken into account. *Bottom:* Background (NXB+CXB) subtracted SXI (black cross) and HXI (red cross) spectra. For reference, solid lines show the thermal spectra with $kT = 5$ keV.

6.3.2 Very hot gas at the center of Abell 3667

Suzaku revealed the presence of very hot thermal gas in the central region of A3667, with temperature higher than 13 keV (Nakazawa et al. 2009). With the improved sensitivity and imaging capability of *ASTRO-H*, we will be able to determine the temperature and map the location of this ICM component.

To simulate HXI and SXI spectra from the center of A3667, we extract the parameters from Nakazawa et. al. (2009) assuming a two-temperature thermal emission (2kT) model with temperatures of 4.7 keV and 19.2 keV (the most probable temperature of the very hot gas inferred in this paper). We also simulate the spectra toward an adjacent region $9'$ away from the cluster center, assuming an azimuthally averaged brightness profile, to examine if the fainter emission from this region is still detectable. The simulated spectra are fitted either with a 2kT model or a single-temperature (1kT) model; the temperature, abundance and normalization are free parameters, whereas the neutral hydrogen column density ($N_{\text{H}} = 4.7 \times 10^{20} \text{ cm}^{-2}$) and the redshift are fixed. Figure 34 shows that the broad-band HXI and SXI data will enable us to clearly disentangle the two temperature components not only from the cluster center but also from the fainter adjacent region.

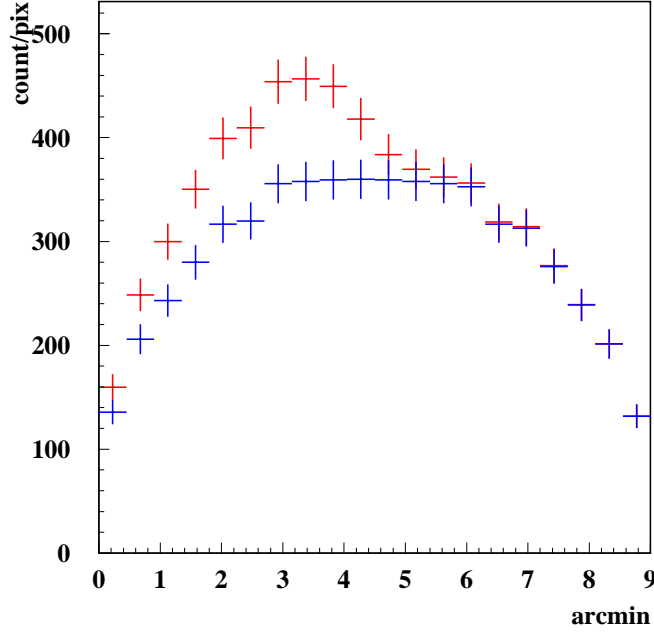


Figure 33: Projection to Y-axis of Figure 32. Profiles of the total count and background count are shown in red and blue, respectively. Error bars indicate statistical 1σ errors.

6.3.3 Coma cluster

We further explore the detectability of inverse-Compton radiation from the radio halo of the Coma cluster. To quantify the impacts of systematics that dominate the error budget, we first create simulated spectra of SXI and HXI for an extremely long (500 Ms) exposure taking into account the NXB, the CXB, and the thermal ICM component with $kT = 8.62$ keV. The CXB is modeled in the same manner as Nakazawa et al. (2009). Figure 35 illustrates the simulated HXI spectra of each component together with the 90% upper limit that can be placed on the non-thermal component with $\Gamma = 2.0$. Table 19 further shows how the expected sensitivity from the HXI and SXI data varies with uncertainties of the backgrounds and the cross normalization between the SXI and HXI. We also performed simulations for 500 ks (which is close to the exposure discussed in Section 5.3.1 for an SXS investigation of the ICM turbulence) and checked that statistical errors will increase the upper limits listed in this Table only by $\sim 0.2 \times 10^{-16}$ erg s $^{-1}$ cm $^{-2}$ arcmin $^{-2}$.

In the most conservative case with 7%, 5%, and 7% uncertainties in the NXB, the CXB, and the cross normalization between the SXI and HXI, respectively, the expected upper-limit (90%) on the non-thermal intensity is 8.9×10^{-16} erg s $^{-1}$ cm $^{-2}$ arcmin $^{-2}$ at 20–80 keV for a 500 ks exposure. This will be a factor of ~ 6 improvement over the previous limit by *Suzaku* for the same energy band, 5.3×10^{-15} erg s $^{-1}$ cm $^{-2}$ arcmin $^{-2}$ (Wik et al. 2009), and will correspond to the lower bound on the magnetic field of $B \sim 0.4$ μ G for $\Gamma = 2.0$. Using Faraday rotation measurements, Bonafede et al. (2010) estimate the magnetic field strength at the center of the Coma cluster to be $B \sim 5$ μ G, which would suggest that, given the sensitivity limit of *ASTRO-H* presented above, inverse-Compton radiation is unlikely to be detected from the giant halo in Coma. Estimates for other clusters with radio halos suggest that the expected inverse Compton signal is similarly below the HXI sensitivity, if the current Faraday rotation estimates of B are representative of the volume-averaged field. However, the X-ray signal may be considerably higher if, for example, the magnetic field and the cosmic ray population are distributed differently in the cluster volume, which is not an improbable scenario. Since merging clusters with giant radio halos (such as Coma, A754, A2319, Bullet) are likely to be the targets of long SXS observations, with time we should accumulate enough HXI data to test such scenarios.

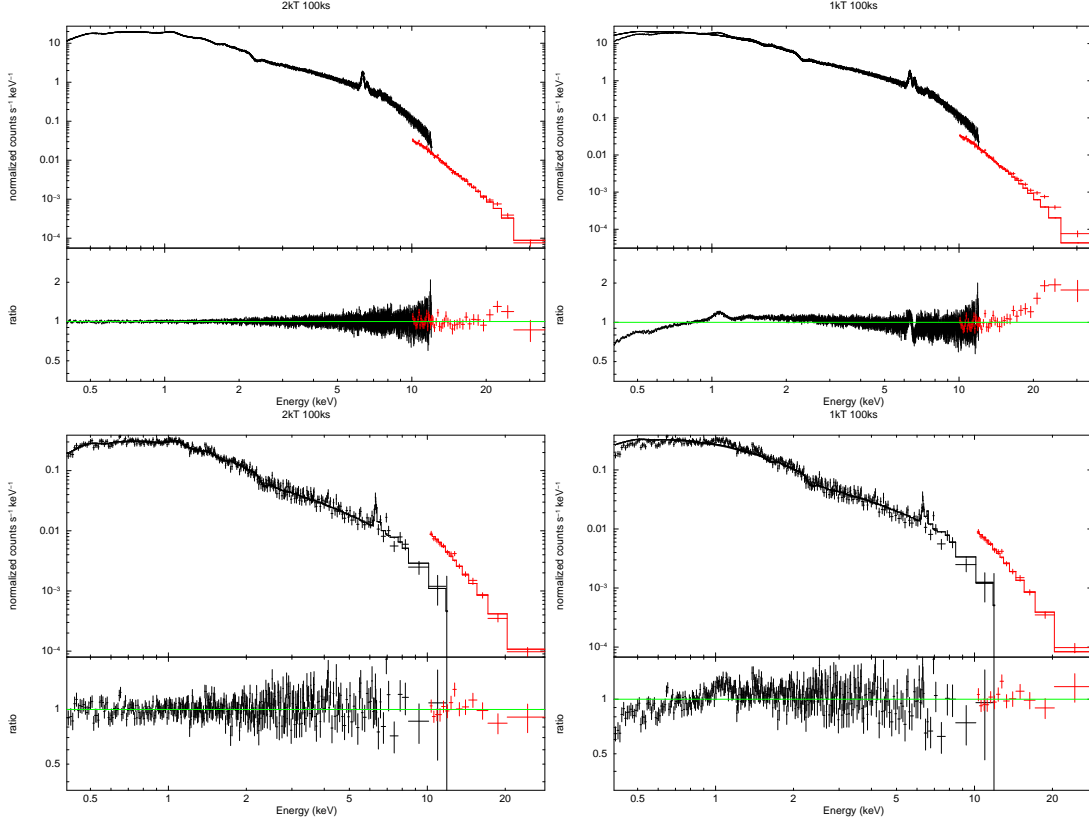


Figure 34: Simulated SXI and HXI spectra (100 ks) of the two-temperature ICM (4.7 keV and 19.2 keV) at the center of A3667, fitted with two-temperature model (top left, $\chi^2/d.o.f = 2500.7/2519 = 0.993$; null hypothesis probability = 0.598) and one-temperature model (top right, $\chi^2/d.o.f = 37572.6/2522 = 14.9$; null hypothesis probability = 0.000). Another simulation at the adjacent HXI region is also fitted with two-temperature model (bottom left, $\chi^2/d.o.f = 580.8/572 = 1.015$; null hypothesis probability = 0.391) and one-temperature model (bottom right, $\chi^2/d.o.f = 960.9/575 = 1.671$; null hypothesis probability = 0.000).

6.4 Lessons Learned from *NuSTAR*

It is important to take advantage of the lessons learned from the cluster observations with *NuSTAR*. So far (as of April 1, 2014), there is one publication reporting the observations of galaxy clusters with *NuSTAR* (Wik et al. 2014). That paper, reporting the observations of the Bullet Cluster, 1E 0657–558 at $z = 0.296$, contains a very extensive discussion of background and systematic effects associated with hard X-ray imaging observations of extended sources. The *NuSTAR* bandpass covers roughly 3 - 80 keV, so it is quite comparable to *ASTRO-H* HXI. The effective area is also comparable, peaking at $\sim 250 \text{ cm}^2$ per module. The Point-Spread Function of *NuSTAR*, $\sim 1'$, is somewhat better than of the HXI, so the image quality is likely somewhat better. *NuSTAR* is on an equatorial orbit, so the particle and activation backgrounds are lower than those for the orbit expected for *ASTRO-H* (here, the background rejection scheme adopted in the design of the HXI detectors might mitigate the difference). However, *NuSTAR* lacks the light baffle in front of the instrument, and the stray Cosmic X-ray Background partly contaminates the detector. In *ASTRO-H*, the CXB shield has been designed to fully block such stray cosmic X-rays. All those effects need to be taken into consideration in deriving the expected sensitivity of the HXI for extended sources, and in the comparison of the two instruments. In any case, the *NuSTAR* observations of the Bullet Cluster indicate a multi-temperature structure, with the hot component at $kT \sim 15 \text{ keV}$, and only a marginal evidence of non-thermal emission. All this means that the very accurate determination of background from all sources will be key in any conclusive hard X-ray measurements.

Table 19: Sensitivity of HXI+SXI on the non-thermal emission with $\Gamma = 2.0$ from the center of Coma for a range of systematic errors, neglecting statistical errors (assuming an exposure time of 500 Ms).

Systematic errors	Upper limit (90%, 20–80 keV) [erg s ⁻¹ cm ⁻² arcmin ⁻²]
NXB 3%	4.0×10^{-16}
NXB 5%	5.3×10^{-16}
NXB 7%	6.5×10^{-16}
NXB 3%, CXB 5%	4.6×10^{-16}
NXB 5%, CXB 5%	5.8×10^{-16}
NXB 7%, CXB 5%	7.1×10^{-16}
NXB 7%, CXB 5%, Cross-norm 1%	7.4×10^{-16}
NXB 7%, CXB 5%, Cross-norm 5%	8.3×10^{-16}
NXB 7%, CXB 5%, Cross-norm 7%	8.7×10^{-16}

Again, two main “direct” goals resulting from the detection / measurement of non-thermal emission in clusters are: the volume-integrated distribution of energetic particles in the cluster, and the average magnetic field. However, those can be strongly enhanced by taking advantage of data in other bands.

(1) Measurement of cluster magnetic fields: here, the most important will be correlative studies with radio bands. For relatively nearby clusters, the PSF of the Hard X-ray Imagers will be sufficient to perform detailed spatial cross-correlations with radio maps. In addition, radio polarization observations will be very valuable. Such observations provide a clue to the structure and physical scale of the coherence of magnetic fields.

(2) Process of thermalization of the cluster plasma: given the excellent complement of X-ray instruments on board of *ASTRO-H*, we should be able to address the question of thermalization of the intra-cluster gas. One aspect that will weigh in on understanding this process is the strength and structure of magnetic field discussed above, but importantly, the distribution of temperature of the thermal plasma will play an important role. Since the SXI and the SXS observations will be secured as all instruments are co-aligned, no additional data will be necessary. However, good measurements of the temperature structure will require that the instruments are accurately cross-calibrated, with an additional requirement that the off-axis effective area of *all* imagers is well-determined.

7 Chemical Composition and Evolution

Overview

The chemical composition of the hot gas in galaxies and clusters of galaxies contains valuable information about the origin of chemical elements and their distribution during the evolution of the universe. It is currently believed that most heavy elements were produced by type Ia and core-collapse supernovae during the major epoch of star formation around $z = 2 - 3$. The chemical abundances provide clues about stellar populations, the history of star formation, the Initial-Mass Function (IMF), and the type Ia explosion mechanism. We summarize the expected science results from spatially resolved abundance measurements in bright clusters of galaxies. Many of these clusters are also discussed in other scientific contexts in this paper. Typically, 100 ksec exposures are required for detecting a range of elements in cluster cores. In the data with the highest statistics we may detect rare elements such as Na, Al, Cr, and Mn. Measuring the evolution of elements as a function of redshift would be challenging.¹⁴

¹⁴Coordinators of this section: J. de Plaa, K. Sato

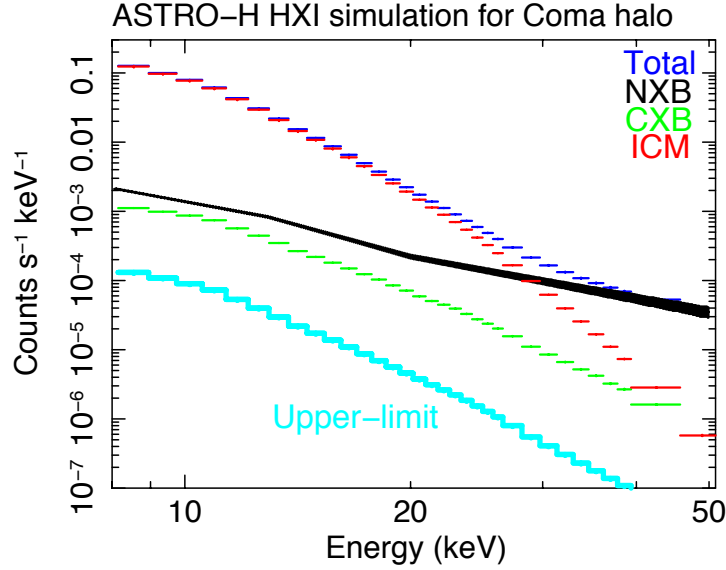


Figure 35: Simulated HXI spectrum (blue) from the center of the Coma cluster (500 Ms exposure) with 7%, 5%, and 7% uncertainties in the NXB, the CXB, and the cross normalization between the SXI and the HXI, respectively. Also shown is each spectral component, the ICM (red), NXB (black), CXB (green), and 90% upper limit of non-thermal power-law emission (cyan).

7.1 Background and Previous Studies

Chemical elements with atomic number 6 (C) and above have all been produced by stars and supernovae during the history of our Universe. The first stars that started the epoch of re-ionization around $z = 10$, known as Population III stars, were also the first objects to create heavier metals. Their total contribution to the enrichment of the current-day Universe is, however, thought to be small (e.g. Matteucci & Calura, 2005). The bulk of the metals are produced by the stars formed around the peak of the universal star-formation rate at $z \sim 2-3$. Core-collapse (SNcc), which would include the Population III stars, and type Ia supernovae have very different abundance ratio patterns. The initial metallicity of the progenitors, as well as the initial mass function of the stars that explode as SNcc, also influence the relative abundances in the present-day universe. The lighter metals, from O to Si and S, are mainly produced in massive stars and ejected in SNcc at the end of their life time. Since the metal yield of these supernovae depends on the mass of the progenitor star, which ranges between roughly $8 M_{\odot}$ and $100 M_{\odot}$, the total metal yield of the stellar population depends on the Initial-Mass Function (IMF). The metals from Si to Fe and Ni are also produced during type Ia supernova explosions (SNIa). The binary configuration of SNIa progenitors and their explosion mechanism is, however, still poorly known (see e.g. Howell, 2011, for a review). Current population synthesis models (Ruiter et al., 2009) suggest that most of the type Ia supernovae have a white dwarf binary progenitor and explode gigayears after the initial star burst. Binaries with one white dwarf and a different companion may produce a type Ia in the first few gigayears after the star burst. These models contain, however, several assumptions and uncertainties. In addition, uncertainties in the SNIa explosion mechanism cause uncertainties in the yields of about a factor of two. Observational constraints, therefore, would help to understand the SNIa origin and explosion mechanisms.

The ICM in clusters of galaxies serves as the repository for type Ia and SNcc ejecta. Since the formation of the ICM around $z \sim 2$, star formation in the member galaxies has been suppressed. The hot gas in clusters, which is heated through AGN feedback, also heats the cold molecular clouds in the member galaxies, preventing them to collapse and form stars (Gabor et al., 2010). Once the halo reaches a certain temperature and mass (around $z \sim 2$ for most clusters), star formation is effectively quenched. Therefore, the cluster core mostly contains elements produced by the stellar population formed during the $z = 2-3$ star burst, and has a different chemical

history than our own Galaxy. Measuring the chemical composition of the ICM provides a valuable insight in the production of metals by this early stellar population. On the other hand, recent IR and radio observations have found that some cD galaxies in the BCG have relatively higher star formation rate (see e.g. O’Dea et al., 2008; McNamara et al., 2014), which are associated with the AGN activity and the feedback mechanism.

Measuring abundances in clusters has several advantages over observations of individual supernovae or supernova remnants (SNRs). In our own Galaxy, supernova explosions are rare and there are only a handful of bright SNRs available for abundance studies. The progenitor is usually difficult to determine, and the shocked ejecta becomes mixed with material swept-up from the surrounding ISM, making it difficult to estimate yields. Furthermore, extragalactic supernovae are faint in X-rays and are thus difficult to observe. Optical abundance measurements are often unreliable while the explosion is ongoing because elements lying below the explosion’s photosphere may be unobservable. In contrast, the hot ICM of clusters is optically thin and contains the accumulated ejecta of billions of supernovae, providing an average yield from SN over time and space. Most supernova products have not been recycled into new stars since $z \sim 2$. Therefore, the measured abundances represent the average yield of the $z = 2-3$ stellar population. In the end, the SN/SNR observations and the cluster abundance measurements will play complementary roles in providing information about supernova explosion physics.

The soft X-ray band is amenable to abundance studies. The ICM is in or very close to collisional ionization equilibrium and is therefore relatively easy to model. Moreover, all elements between C and Zn show emission lines between 0.1 and 10 keV. With *ASCA*, it was possible for the first time to resolve lines of highly abundant elements, like Si and Fe (Mushotzky et al., 1996). *XMM-Newton* and *Suzaku* enabled us to study the abundance patterns of O, Mg, Si, S, Ar, Ca, Fe and Ni. With *Suzaku*, Tamura et al. (2009) detected the He-like Cr line from the cool core of the Perseus cluster. Using *ASCA*, and later *XMM-Newton* and *Suzaku*, several authors (for example Fukazawa et al., 1998; de Plaa et al., 2007; Sato et al., 2007) placed interesting constraints on supernova models using abundance measurements. For example, de Plaa et al. (2007) found that the Ar/Ca ratio was sensitive to the assumed SNIa model. Because a number of common elements from O to Ni were measured, these studies also provided estimates of the SNIa/SNcc ratio. The SNIa contribution is estimated to be about 30% of the total contribution, which is consistent with the SNIa/SNcc ratio of 0.2-0.4 as determined from studies at optical wavelengths.

The observed values of the Ni/Fe ratios in the ICM have a significant scatter (e.g. de Grandi & Molendi, 2009; Matsushita et al., 2013b). In contrast, in our Galaxy, both SNcc and SNIa have synthesized Ni in the same way as Fe, since the [Ni/Fe] of stars is ~ 0 , with no dependence on [Fe/H] (Feltzing & Gustafsson, 1998; Gratton et al., 2003). The observed scatter in the Ni/Fe ratio observed in several cool core clusters indicates that Ni synthesis in cD galaxies might be different from that in our Galaxy. However, with CCD detectors, both Ni-L and K lines are blended into the Fe-L lines and He-like Fe-K line at 7.9 keV, respectively, and the derived Ni abundance might have some systematic uncertainties.

While most heavy elements are produced in supernovae, C and N are most likely produced by and ejected from intermediate-mass and massive stars. Their origin is, however, still subject to debate. Because C and N are relatively light elements, their strong K-shell transitions are found in the soft X-rays. They both ionize completely at high temperatures, therefore their line emission is best detected in elliptical galaxies and groups with temperatures below 2 keV. Using the RGS instrument on *XMM-Newton*, Werner et al. (2006) and Grange (2011) detected N in the spectra of M 87, NGC 5044, and NGC 5813. Its relatively high abundance would be difficult to produce by supernova explosions, which are presumably rare in these objects, but would be more easily produced by intermediate-mass or massive stars.

Recent X-ray observations have yielded measurements of the metal abundance distributions in the ICM based on spatially resolved spectra. The metals in the cool cores of clusters represent a mixture of those present in the ICM and later supplies from the cD galaxies. The latter contain Fe synthesized by SNIa and originating from stars through stellar mass loss. However, in these regions, the distribution of metals is more extended compared to that of the stars. Processes such as jets from a central AGN or the sloshing of cD galaxies in the cluster’s gravitational potential may eject metals from cD galaxies. Therefore, the metal distributions in the cool-cores should be closely related with turbulence and bulk motions which will be measured with *ASTRO-H*

Measuring radial profiles of metals out to larger radii helps us understand the past chemical evolution process. Outside the cool-cores, the metals are accumulated over much longer time scales. The gas in groups and clusters has a very similar value of the Si/Fe ratio, around 1–1.5 (e.g. Sato et al., 2010; Matsushita et al., 2013a,b). The radial profiles of the Fe abundances in the ICM outside the core regions are relatively flat (Matsushita, 2011; Matsushita et al., 2013a; Werner et al., 2013) and both Si and Fe in the ICM are more extended than stars (Matsushita et al., 2013a). These results indicate that a significant fraction of metals is synthesized in an early phase of cluster evolution, certainly before the last merger epoch. Since Si and Fe are synthesized both by SNcc and SNIa, abundance measurements of O, Ne and Mg are needed to obtain unambiguous information on their origin. With some *Suzaku* observations, the O/Fe and Mg/Fe ratios suggest an increase with radius. However, with the CCD detectors, the emission lines from our Galaxy and surrounding Fe-L lines cause systematic uncertainties in the O and Mg abundance measurements.

Galactic winds, ram-pressure stripping, AGN activity, and sloshing play a role (e.g. Strickland & Stevens, 2000; Schindler & Diaferio, 2008) in the enrichment, diffusion, and mixing of the metals, as do contribution from intracluster stars (e.g. Zhang et al., 2011; Gal-Yam et al., 2003). Although this stellar component is difficult to observe, it appears to contribute a substantial amount of metals to the ICM in the core. Recent numerical simulations of the metal enrichment of the ICM indicate that it is difficult to know how the elements have been ejected from galaxies into the ICM; numerical simulations are currently unable to reproduce in detail the elemental distributions in the ICM (e.g. Kapferer et al., 2007; Planelles et al., 2014).

7.2 Prospects and Strategy

ASTRO-H is well suited to abundance measurements. Although its effective area is modest, deep observations of bright clusters using the high-spectral resolution SXS will provide accurate abundance measurements of the common elements from N to Ni. Elements with strong lines, like O, Si, S, and Fe, are relatively easy to measure. The challenge will be to measure abundances of elements with weak and/or blended lines. *ASTRO-H* will be adept at the measurement of abundances of elements associated with dense line complexes, such as Ne, which has lines in the Fe-L complex.

Abundance measurements of a wide range of heavy and light elements will place tight constraints on the progenitor and current stellar populations in clusters and the mechanisms that produced the chemical elements. O, Ne, and Mg are mainly ejected by SNcc. However, their relative abundances depend not only on the details of the explosion, but on the initial metallicity of the stars and the IMF. Heavier elements like Ar, Ca, Fe, and Ni, are produced in SNIa and their abundance ratios depend on the SNIa explosion mechanism and perhaps also their initial metallicity. Using accurate *ASTRO-H* abundances, we can learn more about the dominant stellar population that was formed in the cluster around $z = 2 - 3$. Within cool cores, the contributions of ongoing enrichment via stellar mass loss and SNe Ia from central galaxies may be significant (e.g. Matsushita et al., 2003; Böhringer et al., 2004), and can therefore be studied with *ASTRO-H*.

SXS may detect weak lines from rare elements in the ICM such as Cr, Mn, Al, and Na in high signal to noise observations. Nucleosynthesis models indicate that the abundances of odd-Z elements like Al and Na depend on the stellar metallicity (Nomoto et al., 2006; Kobayashi et al., 2006). These elements are enhanced by the surplus of neutrons in ^{22}Ne , which is synthesized by the CNO cycle during He-burning. Therefore, the metallicity of Al and Na of the ICM may trace the metallicity of the underlying stellar population. Similarly, the Cr/Mn ratio is correlated with the initial metallicity of SNIa (Badenes et al., 2008). In addition, nucleosynthesis models and observations of Galactic stars indicate that Mn is mostly produced by SNIa rather than SNcc. Therefore, the Cr/Mn ratio can be used to probe the relative contribution of SNcc and SNIa (Nomoto et al., 2006). Such abundance measurements will be possible in bright cD galaxies located in cluster cores, such as M 87, the Centaurus cluster and the Perseus cluster. Rare element abundances and the level of velocity broadening, which tends to wash-out the lines, are poorly understood, making feasibility estimates uncertain. This problem is discussed in Section 7.4.1.

The SXS is a non-dispersive spectrometer that provides full spectral resolution for extended sources. In contrast, the spectral resolution of extended sources observed using dispersive spectrometers, such as the grat-

ings on *XMM-Newton* and *Chandra*, is eroded as the lines are blended with the spatial extent of the source. Therefore, the spectral resolution depends on the angular extent of the source. In addition, every spectral line emitted by the source may have its own spatial distribution, which complicates correct modeling of the line profiles. The *ASTRO-H* SXS will not suffer this disadvantage, allowing much more accurate measurements of the strength of individual lines in extended sources.

A possible complication will be the currently unknown velocity profile of the spectral lines, which will be detected for the first time in these high-resolution spectra. Bulk motions of different pockets of gas in the core may cause complicated line profiles, especially when these pockets have a different enrichment history. Their velocity distributions may be difficult to model using the observed line profiles, resulting in small systematic errors in the abundance measurements.

In order to investigate the role of elliptical and spiral galaxies, and their (different) stellar populations, to the chemical enrichment of the ICM, it will be necessary to observe individual elliptical and star-burst galaxies, like NGC 5044 and NGC 253. Elliptical galaxies contain relatively old stellar populations and would mainly produce SNe Ia and AGB star products. Star-burst galaxies are dominated by SNcc and are likely to have different chemical compositions. These differences will provide better insight into the balance between the sources of metals. As for starburst galaxies, metals in the inter-stellar medium are thought to escape into the inter-galactic space via outflows heated by SNcc. Therefore, metal abundances and their ratios play key roles for investigating how the metals are transported into the inter-galactic and ICM space.

7.3 Targets and Feasibility

Measurements of elemental abundances in bright clusters can be done simultaneously with those of gas motions discussed in other sections of this paper. We intend to use this data supplemented by additional observations described in detail below. The proposed targets are nearby bright galaxies and galaxy clusters that span approximately a decade in gas temperature ($kT \sim 0.8\text{--}8$ keV). The sample is intended to investigate metal enrichment processes over a wide range of mass scales from individual galaxies to the largest galaxy clusters. In this section, we use 68% confidence limits, unless stated otherwise.

7.3.1 The metals in the cool cores

The Virgo (~ 2 keV, $z=0.004$), Centaurus (~ 4 keV, $z=0.010$), and Perseus clusters (~ 6 keV, $z=0.018$) are nearby, bright cool-core clusters. Their metal abundance patterns have been studied in detail using lower resolution CCD spectra obtained with *XMM-Newton*, *Chandra*, and *Suzaku* (Matsushita et al., 2003; Sanders & Fabian, 2006; Matsushita et al., 2007; Tamura et al., 2009; Million et al., 2011; Sakuma et al., 2011; Matsushita, 2011). Figure 36 shows the radial profiles of the Fe abundance of M 87, the Centaurus cluster, the Perseus cluster, and a more distant cluster A 1795 at $z = 0.062$, observed with *XMM-Newton*. Observations of relatively nearby clusters ($z < 0.03$) are required to spatially resolve the cool cores and derive metal distributions in these regions with SXS. *ASTRO-H* observations of the centers of these clusters will provide the best statistics, and provide benchmark measurements of the thermal and chemical structure of the intra-cluster medium (ICM), and of the ICM dynamics as described in Sections 2 and 3.

Metal distribution in cool-cores and AGN feedback

As shown in Figure 36, within the central $1.5'$ of M 87, the enrichment timescale of the Fe mass in the ICM, or the ratio of integrated Fe mass to the present Fe production rate by SN Ia, is only 1 Gyr. This short timescale indicates that the gaseous halo of M87 and its composition in this region may be explained by ongoing stellar mass loss and SNIa. Simionescu et al. (2008) suggested that AGN activity in M 87 is able to lift enriched material from the center further out into the ICM (see Sec. 3 for details). The simulations in Section 3 show that we will be able to accurately measure the metallicity of the uplifted gas independently from that of the surrounding ICM, determining the Fe abundance of the cool gas to better than 10% accuracy and thus robustly determining how gas motions induced by the AGN spread out metals produced in the central galaxy.

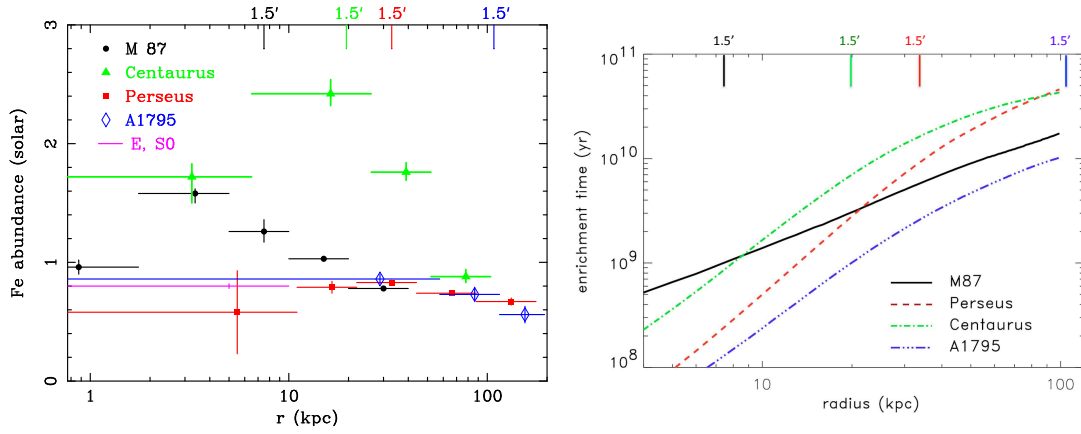


Figure 36: *Left:* The radial profiles of the Fe abundances in the center of the Virgo cluster (around M 87) (closed black filled circles, Matsushita et al., 2003), the Centaurus cluster (Matsushita et al., 2007, green filled triangles), Perseus cluster (red filled squares), and A1795 cluster (blue open diamonds, Matsushita, 2011) observed with *XMM-Newton*. The horizontal magenta lines show the weighted average of the Fe abundance in the hot ISM of 17 early-type galaxies observed with *Suzaku* (Konami et al., 2014). The short vertical lines indicate 1.5' from the center of each cluster. *Right:* The ratio of the integrated Fe mass to the present Fe production rate by SN Ia for the central Fe abundance peak of four clusters by metals from the cD galaxies (Böhringer et al., 2004). The short vertical lines indicate 1.5' from the center of each cluster.

The distributions of Fe in cool cores vary from cluster to cluster (Figure 36). The enrichment time scale within the central 1.5' for the Centaurus cluster and the Perseus cluster are an order of magnitude longer than that for M 87 (Figure 36). We will hence observe metals accumulated over a much longer time scale in these clusters. The Fe abundance within 1.5' of the center of the Centaurus cluster is exceptionally high, being roughly twice the solar value. This is much higher than in other clusters including the Perseus cluster. Panagoulia et al. (2013) suggest that the Fe abundance has a sharp drop within the central 5 kpc region, and would be uplifted by the bubbling feedback process to 10–20 kpc, where the Fe abundance becomes high. The difference in the Fe distributions may be related to differences in mixing due to AGN feedback from and sloshing motions. Therefore, in combination with measurements of turbulent velocities in these cool-cool cores, we will be able to study the effect of the AGN feedback.

Abundance pattern of SNIa of the Centaurus cluster

The Centaurus cluster is a compelling target for studying the abundance pattern synthesized by past SNIa. The O/Fe and Mg/Fe ratios in the ICM of the core of the Centaurus cluster is the lowest among cool core clusters observed with *Suzaku* (Sakuma et al., 2011). The very high Fe abundance with the sharp Fe abundance peak and the low Mg/Fe ratios suggest that the metals in the center of the Centaurus cluster are more dominated from those synthesized by SNIa in the central galaxy than those in other cool core clusters.

As shown in Figure 36, the peak Fe abundance in the Centaurus cluster is also significantly higher than that in the hot interstellar medium, ISM, in early-type galaxies, which have much smaller gas mass to light ratio than cool-core regions, and represent present metal supply from these galaxies. The O/Fe and Mg/Fe ratios in the ISM of these galaxies are close to the solar ratios and nearly a factor of two higher than those in the core of the Centaurus cluster (Konami et al., 2014). The difference in the Fe abundance and abundance ratios indicates that the metals in the center of the Centaurus cluster may not be a simple mixture of those in the ICM and the current ISM in early-type galaxies. A longer time scale implies that the ratio of SNIa rate to stellar mass loss rate was higher in the past.

The higher SN Ia contribution to the enrichment in the Centaurus cluster results in a higher abundance of Ar and Ca, whose abundance ratio is sensitive to the SNIa model. With a 100 ks exposure, both He-like and H-like lines of Ar and Ca from the Centaurus cluster will be easily detected with SXS as shown in Figure 37. The total expected number of photons from Ar and Ca lines are about 1000 and several hundred, respectively.

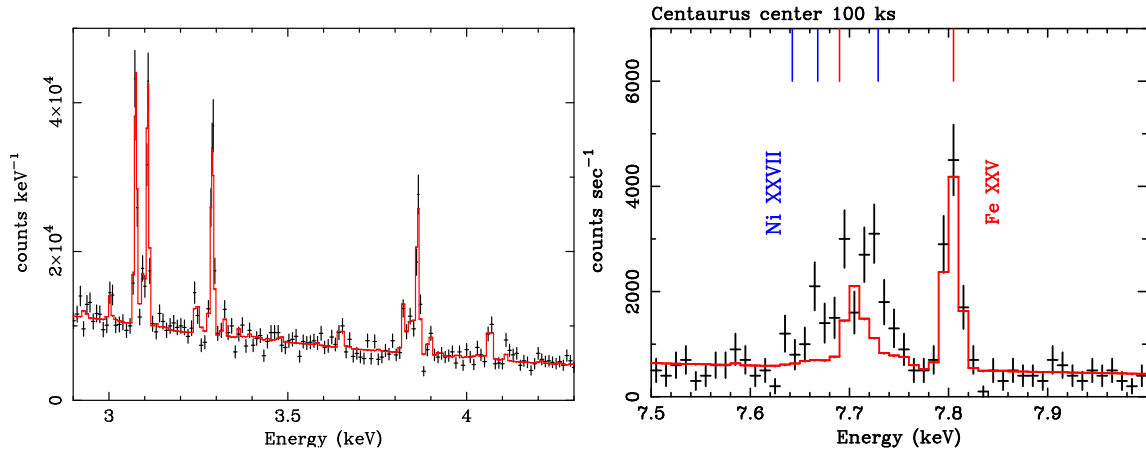


Figure 37: The simulated SXS spectra at the center of the Centaurus cluster (100 ks) around the Ar and Ca lines (left panel) and the He-like Ni and Fe lines (right panel). The solid lines in the right panel correspond to the models with zero Ni abundances. The blue vertical lines indicate the redshifted energies of strong lines in the He-like Ni triplets, whereas the red vertical lines those of Fe lines.

With *XMM-Newton*, the derived Ni/Fe abundance in the Centaurus cluster is significantly higher than the solar ratio, while those in the Perseus cluster and the Coma cluster are more consistent with the solar ratio (Matsushita et al., 2013b). With CCD detectors, the He-like Ni line at 7.8 keV (rest frame) and the He-like Fe line at 7.9 keV are blended into a single bump, and the Ni abundance measurements couple with the effect of resonant line scattering. In contrast, as shown in Figure 37, with *ASTRO-H*, these lines are separated from each other. With a 100 ks exposure of the center of the Centaurus cluster, we will expect a few hundred of photons for the He-like Ni line triplets and ~ 200 photons for the He-like Fe line at 7.9 keV.

Accurate measurements of the abundances of α -elements

The line diagnostics with SXS will constrain the temperature structure in cool-core regions. In addition, O, Ne and Mg lines will be separated from the surrounding Fe-L lines. With the CCD detectors, different plasma codes sometimes yield significantly different Ne and Mg abundances. As shown in Figure 38, on the other hand, the SXS will be able to derive line strengths of Ly α lines of H-like ions like Ne X and Mg XII. As a result, systematic uncertainties in the abundance measurements caused by uncertainties in the temperature structure and due to blending with other lines will be significantly reduced. The abundances of O, Ne, Mg, Si, S, Ar, and Ca will be measured within a few % statistical accuracy in 100 ks exposures of cool-cores. The expected statistical uncertainties of abundance measurements in the Perseus cluster are listed in Tables 1 and 2, and those for the Centaurus cluster and Abell 2199 ($z = 0.03$) are shown in Figure 39.

Using low-resolution *Chandra* data, Million et al. (2011) found the surprising trend that, in the Virgo cluster, the Si and S abundances are *more* centrally peaked than Fe, challenging the standard picture of chemical enrichment in galaxy clusters, wherein SNIa from an evolved stellar population are thought to dominate the central enrichment. *ASTRO-H* will allow us to check these results. As shown in Table 3, we will measure the O, Ne, Mg, Si, and S abundances in Virgo with an uncertainty of only ± 0.1 solar per 1×1 arcmin spatial resolution element in each of the central pointings with the same data as simulated in Section 3, providing a spatially resolved radial profile of the metal abundances and relative SNIa/SNcc contributions out to a radius of 5 arcmin (approximately 25 kpc).

Na and Al abundances of M 87

ASTRO-H will search for faint lines from rare elements. Due to relatively low ICM temperatures, the low energy lines below 3 keV from M 87 are much more prominent than those in hotter clusters. M 87 is the best target to measure the metal abundances from N to Al. Na and Al abundances in the ISM of M 87 derived

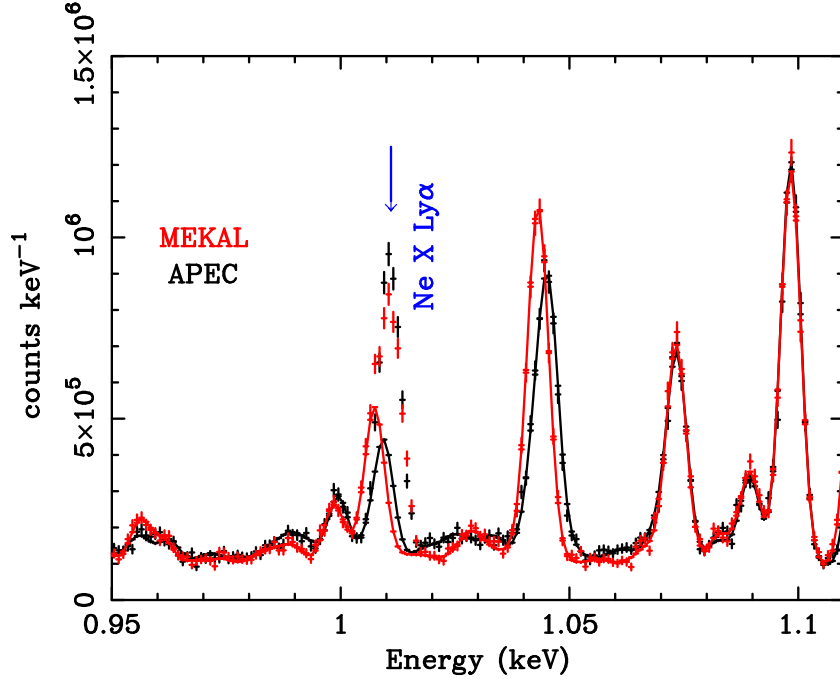


Figure 38: The simulated SXS spectra of the Centaurus cluster (100 ks) around the Ly α line of H-like Ne (1.02 keV in the rest frame). We use the best-fit two temperature vAPEC model (black, Fe=1.8 solar, Ne=2.4 solar) and vMEKAL model (red, Fe=2.1 solar, Ne=2.1 solar) to the *XMM-Newton* MOS spectra at $0.5' - 1.5'$ from the X-ray peak of the Centaurus cluster. The solid lines show the best-fit models but the Ne abundance was changed to 0.

from the simulated spectrum (assuming that the abundances of Na and Al are the same as that of Mg) are 0.92 ± 0.17 solar and 0.78 ± 0.06 solar, respectively, with a 100 ks exposure, considering only statistical errors. Unfortunately, there are Fe and Ni lines at almost same energies as the Ly α lines of Na and Al (Figure 40). Here, we also show a simulated SXS spectrum of the center of the Perseus cluster. The contribution of Fe lines to the Al and Fe line blend at 1.73 keV is higher in the hot clusters. For example, about a half of photons and a two-third of photons from the 1.73 keV line blend come from the Fe lines for M 87 and the Perseus cluster, respectively. The contribution of the Fe line should be much smaller for groups of galaxies. The Ly α line of Na is seen at the residual structure at 1.23 keV and 1.21 keV of the simulated spectra of the M 87 and the Perseus cluster, respectively (Figure 40). Using other Fe-L lines, we may compare the Fe-L atomic data and then, we will be able to constrain the systematic uncertainties due to uncertainties in the Fe-L contributions to the Na and Al lines.

7.3.2 Metal distributions outside cool-cores

Primary targets for measuring the radial profile of elemental abundances are those observed for measuring the gas motions out to large radii discussed in Section 4. They include Perseus with $kT \simeq 5$ keV at $z = 0.0179$ (see also Sec. 2.3.3), Abell 2199 with $kT \simeq 4$ keV at $z = 0.030$, Abell 1795 with $kT \simeq 6$ keV at $z = 0.062$, and Abell 2029 with $kT \simeq 8$ keV at $z = 0.077$. These clusters also span a range of gas temperatures, i.e., the mass scales of clusters. For Abell 2199 and Abell 1795, their intermediate gas temperatures allow us to constrain abundances of multiple elements both within and outside the cool cores (Figs 39 and 41). For a higher temperature system like Abell 2029, only the Fe lines are prominent, and its abundance will be determined with $\pm 30\%$ uncertainties out to $0.5 r_{500}$ (Figs 15–17). Although the statistical uncertainties in O and Mg abundance measurements are relatively large, we will be able to reduce systematic uncertainties caused by the strong emission lines of O from our Galaxy and systematic uncertainties in the Fe-L atomic data.

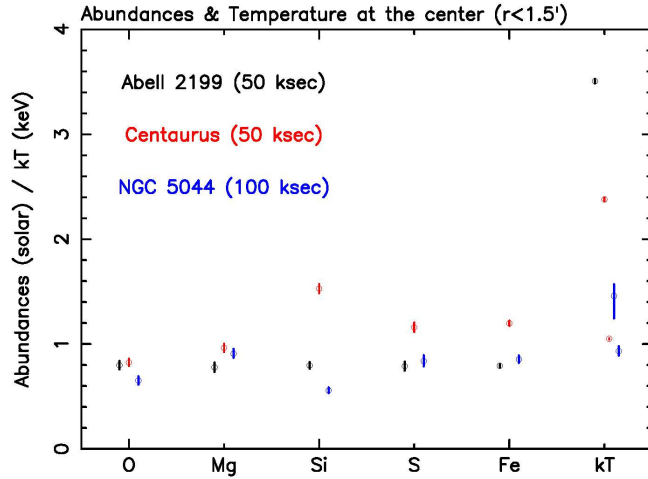


Figure 39: Simulated abundances and temperature at the center within $r < 1.5'$. All the simulations are performed by the SIMX package, and the simulations include the current PSF status.

7.3.3 NGC 5044 and galaxies

NGC 5044 is a giant elliptical galaxy centered in a nearby group of galaxies at redshift $z = 0.00902$. Its X-ray emission is spatially symmetric. In contrast to clusters, observations of galaxy groups will investigate differences in the chemical enrichment history between clusters and groups. Figure 39 shows the resulting temperature and abundances with the errors from the simulations with a 2T model and a velocity of 200 km/s at the central region within $r < 1.5'$ for a 100 ksec observation.

The abundances measured in clusters of galaxies or elliptical galaxies can be compared to abundances in spiral galaxies, like NGC 253. Spiral galaxies tend to have a much younger stellar populations and larger SNcc contributions. Due to the relatively complex structure of spiral galaxies, the presence of a halo, a disk component, and star-forming regions, the spectral model contains several components, which complicates abundance determinations. Using a 200 ks exposure, an estimate of the O/Fe abundance appears to be feasible, which roughly gives an indication about the SNIa/SNcc ratio. For the details about the simulations for elliptical and starburst galaxies, see an accompanying *ASTRO-H* white paper on ISM and galaxies (Paerels et al., 2014).

7.4 Beyond Feasibility

7.4.1 Detection of rare elements

The high spectral resolution of SXS in principle allows the detection of weak lines that place significant constraints on supernova models. The Na/Al and Cr/Mn ratio are, for example, sensitive to the initial metallicity of the stellar population. Weak lines are easier to detect in bright clusters. Nevertheless, the cores of the brightest clusters will require exposure times (well) above 100 ks to accurately determine abundances of the weakest lined elements. Despite these caveats, *ASTRO-H* will in principle be capable to enlarge the number of detected elements from typically 10 with *Suzaku* and *XMM-Newton* to about 20 (see Figure 42), including elements that are key to understanding the SNIa explosion mechanism better. The feasibility of detecting weak lines depends on their abundance, the velocity structure of the core, and the availability of long SXS exposures of bright cluster cores.

In Table 20 we show the expected errors from a simulation of the SXS spectrum of the Perseus core pointing of 50 ks, and what we would observe if the core pointing would be 100 ks. We need to stress that these errors are based on a simulation assuming Gaussian line profiles, which will probably not hold in reality. On the other hand, unless the lines are blended with neighboring lines, the number of counts in the line could be estimated even for lines with a more complex line profile. There is a dependence of the error on the velocity structure,

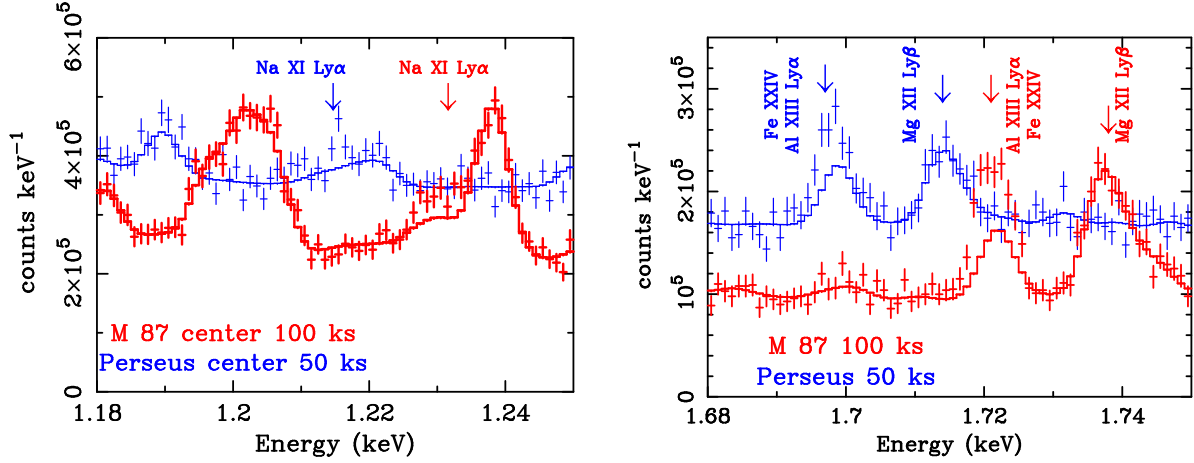


Figure 40: The simulated SXS spectra at the center of M 87 (red; 100 ks) and the Perseus (blue; 50 ks) cluster around Na (left), and Al (right) lines. The solid lines correspond to the models with zero Na, and Al abundances. The red (for M 87) and blue (for Perseus) down arrows indicate the redshifted line energies of Al XIII Ly α (1.729 keV in the rest frame), Fe XXIV (1.729 keV), Mg XII Ly β (1.745 keV), and Na XI Ly α (1.237 keV).

but it is not very strong. In a 50 ks Perseus core exposure we will probably be able to detect Na, Al, Cr, and Mn at a 3σ level. With a 100 ks exposure of the core, we would also get Cl. Table 20 also shows that the Mn abundance, needed for the important Cr/Mn ratio, will probably need more than 50 ks exposure to reach a 5σ significance level. Combining the abundance measurement from the core of Perseus with the results from the off-set pointings will likely provide a Cr/Mn ratio with $>5\sigma$ significance.

Table 20 shows that many other elements are in principle detectable using SXS, but only by using exposure times of more than 0.5 Ms. Detections of these elements would therefore only be expected toward the end of the *ASTRO-H* mission if sufficiently long observations of bright clusters can be stacked.

7.4.2 Abundances as a function of redshift

It may be possible to observe high redshift clusters using long observations with *ASTRO-H*. The limited effective area and the PSF, however, were not optimized for faint cluster detection. In Figure 43, we show the expected abundance errors (in solar units) for a sample of clusters lying between $z = 0.25$ and $z = 2.5$. Using the optimistic assumption that the abundances of O, Si, and Fe are close to the solar value, a 5σ detection would be feasible for points below the dashed line. From the plot it is clear that iron abundances can be well determined only out to $z = 1$ with a 100 ks exposure. Si abundances are feasible up to $z = 0.6$. Oxygen abundances will be much more difficult and only feasible for a few systems between $z = 0.2$ and $z = 0.5$. In addition, the spatial resolution of *ASTRO-H* will not permit the removal of cool cores, which are found to have enhanced metal abundance compared to the centers of non-cool core clusters and the outer ICM (e.g. De Grandi & Molendi, 2001). This unresolved metal abundance profile, along with the unresolved core temperature structure, could complicate analysis without accompanying high-spatial-resolution observations (e.g. Maughan, et al., 2008).

8 Detecting and Characterizing the Warm-Hot Intergalactic Medium

Overview

Understanding the discrepancy between the amounts of baryons measured at high and low redshifts has been the subject of extensive investigation in recent years both from the theoretical and observational point of view. In particular, the focus of the scientific community has been on the nature of the Warm-Hot Intergalactic Medium (WHIM), a warm, filamentary structure with density 20 to 1000 times the critical density of the universe and

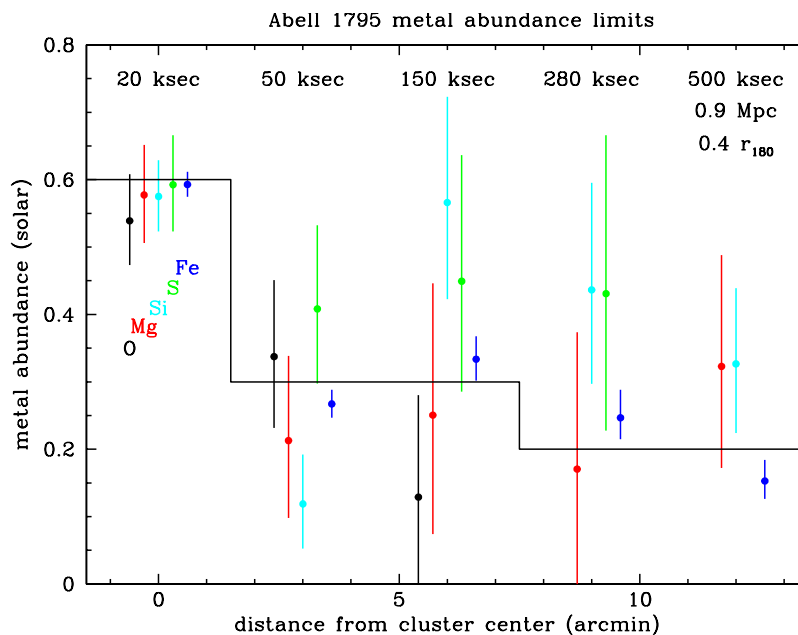


Figure 41: Constraints on metal abundance profile expected for five pointings in Abell 1795. The exposure time of each region needed to reach the errors is shown. The solid line shows the input metal abundance, assumed the same for all elements in a given annulus.

temperature greater than 5×10^5 K filling the intergalactic space. While the grasp (area times solid angle) of *ASTRO-H* is too small for a thorough investigation and characterization of the WHIM, a small number of focused pointings with the SXS high resolution would significantly improve our understanding of the WHIM properties and evolution. In particular, we considered 3 pointings in directions where WHIM filaments have either been detected or are expected. The expected outcome of such investigation is a clear detection of a WHIM filament and its characterization.¹⁵

8.1 Background and Previous Studies

High redshift measurements point to about 4% of the matter-energy density of the Universe to be in the form of baryons, while the rest consists of dark matter and dark energy (Rauch et al. , 1998; Weinberg et al., 1997; Burles and Tytler , 1998; Kirkman , 2003; Bennett , 2003). In contrast, the amount of baryons measured in the local Universe is less than 2% (e.g. Fukugita , 1998). Hydrodynamic simulations suggest that much of the “missing” material lies in a hot ($10^5 - 10^7$ K) filamentary gas at densities 20 to 1000 times the average baryon density of the Universe, filling the intergalactic medium, the Warm-Hot Intergalactic Medium (WHIM - Cen & Ostriker , 2006; Borgani et al., 2004).

The hydrodynamic simulations all agree on the existence of the WHIM, and predict, on average, that about half of the baryons in the current universe are “hidden” in WHIM filaments (Cen & Ostriker , 2006; Borgani et al., 2004). However, there is still great variability in the predicted quantities, and detecting and characterizing the WHIM has been difficult. At the WHIM temperatures and densities the baryons are in the form of highly ionized plasma, making them essentially invisible to all but low energy X-ray and UV observations, mostly through excitation lines of highly ionized heavy elements. However, the WHIM contribution to the total emission in these bands is weak and is expected to be on the order of 10-15% in the soft X-ray band (Takei et al., 2011; Ursino & Galeazzi, 2006; Ursino et al., 2010). Highly ionized metals in the WHIM are also responsible for absorption features whose strength is rather weak (Branchini et al., 2009).

The current clearest detection of the WHIM comes from absorption lines in the FUV spectra of bright, distant sources (Danforth et al. , 2006; Danforth & Shull , 2008; Tripp et al. , 2008; Thom and Chen , 2008; Tilton

¹⁵Coordinators of this section: M. Galeazzi, T. Kitayama

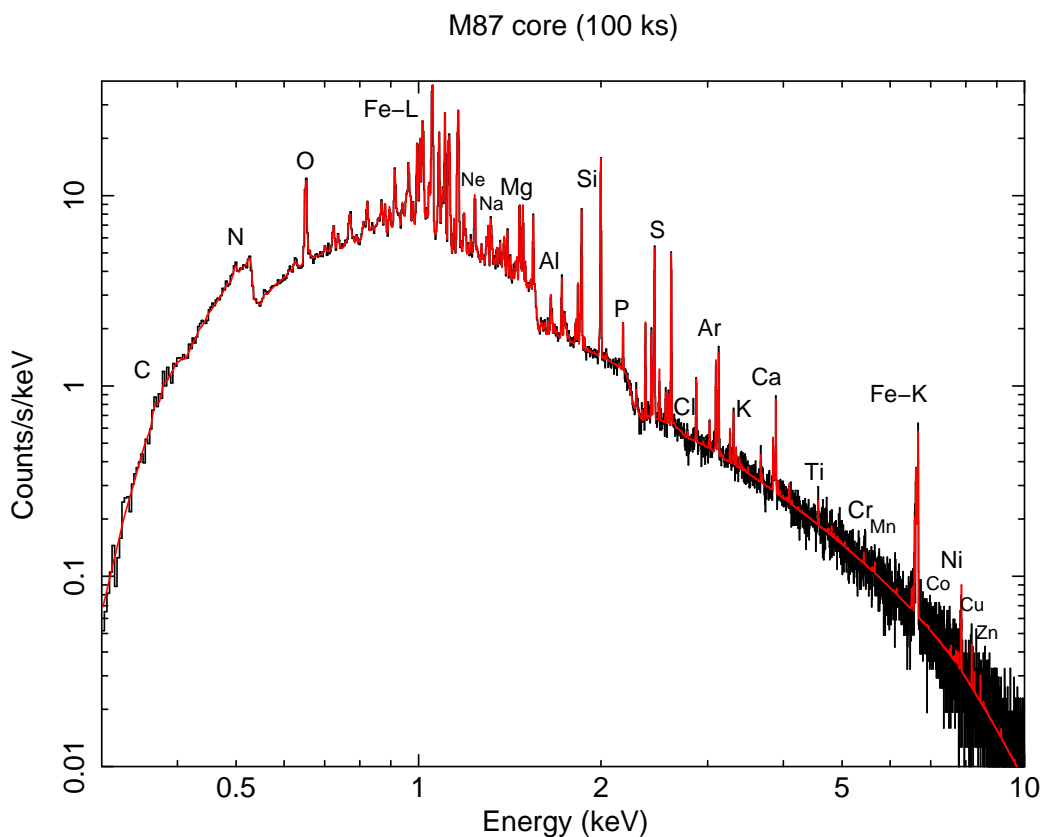


Figure 42: Simulated 100 ks spectrum of the M87 core including lines of rare elements. The positions of the strongest lines are labeled. It shows that a relatively cool objects like M87 produce magnificent line-rich spectra.

et al. , 2012). However, FUV absorbers trace primarily the warm gas ($T < 10^6$ K) and the bulk of the WHIM is expected to be at higher temperatures, characterized by soft X-ray features whose detection is more difficult. A small number of investigations have successfully detected the WHIM signal through soft X-ray absorption and emission measurements. In particular, absorption features have been identified in the soft X-ray spectra of distant quasars (Nicastro et al. , 2005; Buote et al., 2009; Fang et al. , 2010), and emission from one filament between the clusters A222 and A223 has been detected (Werner et al. , 2008). The WHIM signal in emission using a statistical approach based on the angular Autocorrelation Function (AcF) of data from *XMM-Newton* has also been identified (Galeazzi et al. , 2009).

Note that WHIM and cluster investigations conventionally use different definitions for the overdensity, the baryon overdensity $\delta \equiv \rho_b/\bar{\rho}_b$ and the mass overdensity $\Delta \equiv \rho_m/\rho_{\text{crit}}$, where $\bar{\rho}_b$ is the mean baryon density and ρ_{crit} is the critical density of the Universe. Throughout this section, we use the former, which gives a systematically larger value than the latter by $\delta \approx 3.5\Delta$ if baryon traces mass.

8.2 Prospects and Strategy

The *ASTRO-H* grasp (area times solid angle) is too small for any systematic study of the WHIM. However, the SXS instrument will have unprecedented combination of resolution and grasp to resolve emission lines from individual filaments and it is possible to focus on a few specific targets where WHIM filament are expected, to study their density and temperature distribution. In this paper we focus on how to take advantage of the energy resolution of the SXS instrument to detect WHIM filaments in emission and study the filament physical properties. We also investigated the potential of the SXS instrument to detect and characterize the WHIM in absorption and we concluded that the performance of SXS to detect absorption lines, while competitive with that of current instruments (such as *Chandra*), does not improve what is currently available. However,

Table 20: Expected errors in solar units in the SXS Perseus core pointing for several rare elements, assuming the abundance of 1 solar unit for each element. One would need an error smaller than 0.20 and 0.33 solar for a detection better than 5σ and 3σ , respectively. In the last column we provide an estimate of what exposure time is needed to detect an element at the 5σ level.

Element	Exposure		Exposure needed for detection at $>5\sigma$
	50 ks	100 ks	
F	83	59	-
Na	0.35	0.25	≥ 150 ks
Al	0.14	0.10	≥ 25 ks
P	0.7	0.5	≥ 625 ks
Cl	0.4	0.3	≥ 225 ks
K	0.7	0.5	≥ 625 ks
Sc	55	39	-
Ti	0.7	0.5	≥ 625 ks
V	6.0	4.3	-
Cr	0.14	0.10	≥ 25 ks
Mn	0.27	0.19	≥ 90 ks
Co	0.7	0.5	≥ 625 ks
Cu	4.0	2.8	-
Zn	1.6	1.1	-

ASTRO-H could have an advantage in observing transient sources such as GRB and brightening blazars in timely manner. For a discussion on the possibility of detecting WHIM filaments in absorption with *ASTRO-H*, please refer to the accompanying *ASTRO-H* white paper on the high redshift chemical evolution (Tashiro et al., 2014).

To have a high probability of detecting a WHIM filament with the relatively small FOV of *ASTRO-H*, we focused on regions separating virialized structures at the same redshift. Assuming that the virialized structures represent the “nodes” of the cosmic web, if two structures are sufficiently close in angle and redshift, there is a high likelihood of filament connecting the two. In our search, we also required such structures to be sufficiently apart to have a non-virialized region in between, corresponding to a true WHIM filament.

We identified several targets matching our criteria, and focused our attention on two targets, one where, as mentioned before, a high density, high temperature filament has been identified with *XMM-Newton*, and the other where there is indirect evidence of a WHIM filament (although a *Suzaku* investigation has not detected it, but set upper limits on the filament’s emission). Based on our simulations (described below), to have sufficient statistics on emission lines, we need ~ 200 ks observation for each target. We point out that, due to the SXS energy resolution, off-filament pointings to remove background are not necessary.

8.3 Targets and Feasibility

We discuss here the general characteristics of the two identified targets. Later, we will review each target in details, including the potential science outcome of such investigation.

1. Between A222 and A223 (observed with *XMM-Newton* - Werner et al. 2008)

- $z = 0.21$;
- Excess emission detected at $kT = (0.91 \pm 0.25)$ keV;
- Baryon overdensity $\delta \sim 330(L/3 \text{ Mpc})^{-1/2}$, where L is the line-of-sight extent of the filament.

2. Between A3556 and A3558 in the Shapley supercluster (observed with *Suzaku* - Mitsuishi et al. 2012)

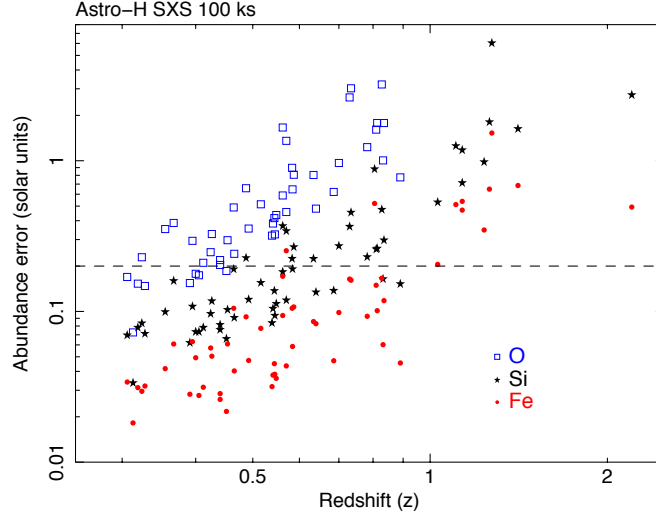


Figure 43: Expected abundance errors of O, Si, and Fe as a function of redshift. Simulated clusters are based on the sample used by Balestra et al. (2007). Each cluster has a simulated exposure time of 100 ks.

- $z = 0.048$;
- O VIII intensity $I < 1.5 \times 10^{-7} \text{ ph cm}^{-2} \text{ s}^{-1} \text{ arcmin}^{-2}$ (2σ);
- O VII intensity $I < 9.0 \times 10^{-7} \text{ ph cm}^{-2} \text{ s}^{-1} \text{ arcmin}^{-2}$ (2σ);
- Baryon overdensity $\delta \lesssim 220(Z/0.3Z_{\odot})^{-1/2}(L/3 \text{ Mpc})^{-1/2}$ (2σ);
- An excess of point sources has been detected with *Chandra*; indications are that the nature of the sources is a much higher than average density of galaxies that could be associated to a WHIM filament;
- A possible overdensity of Neon is suggested.

3. Between A2804 and A2811 in the Sculptor supercluster (observed with *Suzaku* - Sato et al. 2010)

- $z = 0.108$;
- O VIII intensity $I < 3.9 \times 10^{-8} \text{ ph cm}^{-2} \text{ s}^{-1} \text{ arcmin}^{-2}$ (2σ);
- Baryon overdensity $\delta \lesssim 100(Z/0.3Z_{\odot})^{-1/2}(L/3 \text{ Mpc})^{-1/2}$ (2σ).

8.3.1 Between A222 and A223

An excess X-ray emission attributed to a WHIM filament has already been detected in this direction by Werner et al. (2008). The use of *ASTRO-H*SXS would allow the determination with high accuracy of the redshift and temperature of the emitting plasma, to (a) confirm that it comes from a filament connecting the two clusters, and (b) determine the kinematic of the filament.

We simulated *ASTRO-H*SXS spectra for the filament connecting the clusters Abell 222/223, assuming a pointing between the clusters at coordinates 01:37:45.00, 12:54:19.6. Furthermore, we assumed analyzing a spectrum extracted from the full field of view of *ASTRO-H*SXS.

The assumed properties of the X-ray foreground/background components and of the filament were determined based on *XMM-Newton* data of Abell 222/223 (see Werner et al. 2008). We assumed that the filament is at the redshift of the clusters ($z = 0.21$), the hydrogen column density is $N_{\text{H}} = 1.6 \times 10^{20} \text{ cm}^{-2}$, the filaments

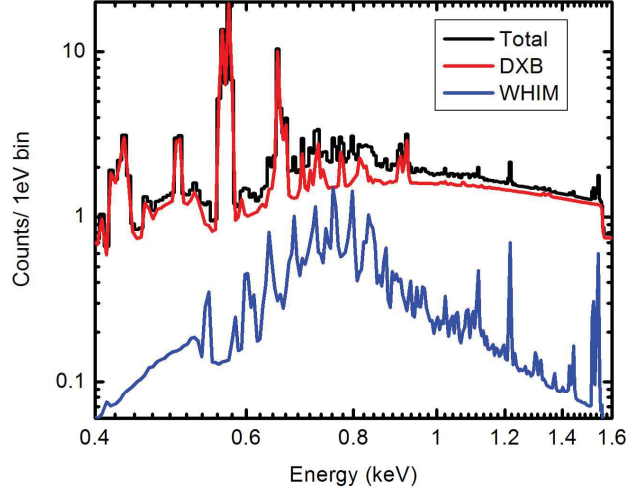


Figure 44: Simulated spectra for a 200 ks exposure of the filament between A222 and A223, broken down into total X-ray emission (black), the WHIM component (blue), and the Diffuse X-ray Background (DXB, red).

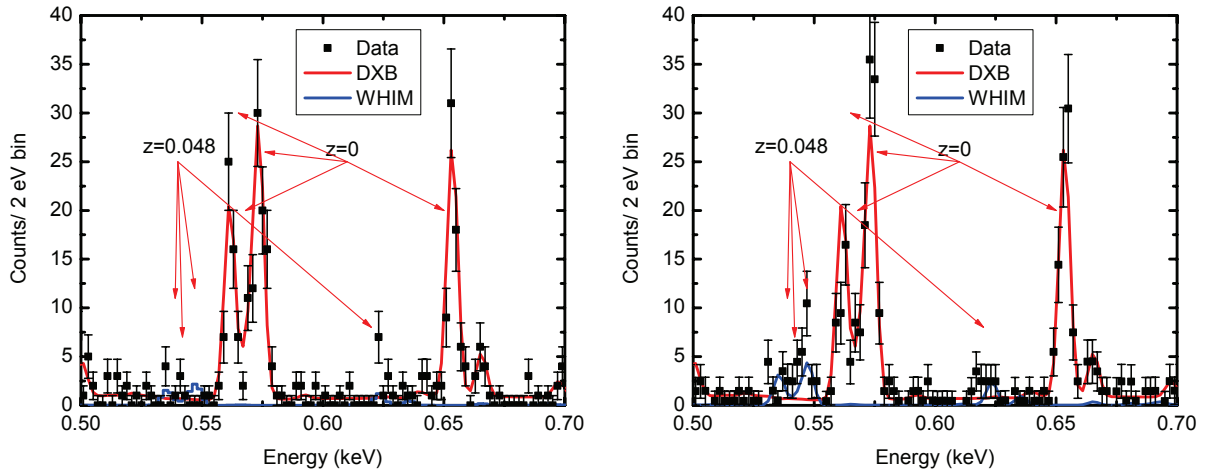


Figure 45: Simulated spectra for a 200 ks exposure of the filament between A3556 and A3558 in the Shapley supercluster. The figures included a potential filament at the 3σ detection threshold (left) and at twice that intensity (right). Each plot includes total emission (black squares), the WHIM component (blue line), and the DXB (red line).

emission measure is $(n_e \times n_p \times V) = 1.72 \times 10^{65} \text{ cm}^{-3}$, the filament temperature is $kT = 0.91 \text{ keV}$, and the filament metallicity is 0.2 solar (assuming proto-solar abundances of Lodders 2003).

Finally, we used the temperature $kT = 0.08 \text{ keV}$ and the flux $F(0.3 - 10 \text{ keV}) = 3.4 \times 10^{-12} \text{ erg s}^{-1} \text{ cm}^{-2}$ for the soft X-ray foreground component, $kT = 0.17 \text{ keV}$ and $F(0.3 - 10 \text{ keV}) = 2.9 \times 10^{-12} \text{ erg s}^{-1} \text{ cm}^{-2}$ for the galactic halo component, and the photon index $\Gamma = 1.41$ and the normalization $2.2 \times 10^{-11} \text{ erg s}^{-1} \text{ cm}^{-2}$ for the power-law component. The assumed metallicity of the Galactic foreground emitting plasma is $Z = 1$ solar.

The spectral simulations were done with the SPEX spectral fitting package. In the spectral fitting C-statistics was employed. According to the simulations a 200 ks *ASTRO-H* observation will allow us to detect the filament gas with a $\sim 9\sigma$ significance and measure its temperature with an expected 1σ uncertainty of 0.06 keV. Furthermore, we will be able to measure the redshift of the filament emission (and thus conclusively prove that it is not a local foreground component) with an expected uncertainty of $z = 0.21^{+0.0023}_{-0.0011}$. The simulated spectrum, including background, is reported in Figure 44.

8.3.2 Between A3556 and A3558 in the Shapley supercluster

A *Suzaku* investigation in this direction in search of a WHIM filament emission did not find it, and set upper limits on the oxygen emission and “filament” density. However, the investigation also found possible evidence of Ne IX emission and a stronger than usual “power-law” emission, associated with unresolved point sources. The same strong component is not present in two control observations one less than 2 deg away. The excess point source emission was confirmed and investigated by a subsequent short *Chandra* pointing. The *Chandra* pointing indicates that the excess is not simply due to cosmic fluctuations and that the source population responsible for the excess seems different from the typical one, dominated by AGNs. In fact, the characteristics of the population is in better agreement with a significantly higher than usual number of galaxies, which could be associated with a WHIM filament.

As no filament has been detected so far in this direction, we focused on the detectability of one and its accuracy. The redshift of the clusters is sufficient to separate the oxygen emission from any local component, making any detection and plasma study much simpler. The excess point sources mentioned before is represented by a larger than usual number of faint sources, which will appear in the SXS spectrum as a power-law distribution, roughly doubling the continuum term of the CXB, but marginally affecting the line detection capabilities.

Using the *Suzaku* and *Chandra* data toward the “filament” for the evaluation of the CXB, the expected SXS detector background, and assuming a 200 ks pointing, the 3σ detection limit for the combined oxygen lines is $0.4 \text{ ph s}^{-1} \text{ cm}^{-2} \text{ sr}^{-1}$, which improves the current limits (Mitsuishi et al. , 2012) by nearly an order of magnitude for OVIII and by a factor of 50 for OVII. Note that the above limit is the minimum brightness required for an uncontroversial detection of the filament. If the filament is only twice as bright as the threshold or brighter (i.e., 5–25 times dimmer than the current limits), any positive detection will be supported by the SXS high energy resolution, which, in addition to making the detection uncontroversial, will also provide detailed information about plasma conditions (e.g., temperature and pressure). Two simulated spectra, zoomed on the Oxygen lines, assuming a oxygen emission equal to the detection threshold (left) and twice the detection threshold (right), are shown in Figure 45.

To estimate the likelihood of detecting X-ray emission from a filament, we used multi-wavelength observations of the region to estimate the density of galaxies and, from there, the total gas density. Data from NASA/IPAC Extra-galactic Database (NED) indicate a significantly higher than average density of galaxies in the region between A3556 and A3558. The stellar mass of the NED galaxies in a field of radius $15'$ centered between the two clusters goes from 3 to 7 times the average baryon density $\bar{\rho}_b$. Including estimates of the galaxy halo mass (and possibly the Circumgalactic Medium - CGM) the estimated gas density in galaxies and their surroundings is between 25 and 100 times $\bar{\rho}_b$. Adding gas not associated with the galaxies brings the expected gas density in the region between 50 and 200 $\bar{\rho}_b$.

We compared such estimates of the density with the density necessary to produce OVII and OVIII lines above the calculated SXS detection limit for a 200 ks pointing, assuming the gas with metallicity $Z = 0.3Z_\odot$ and a line-of-sight extent $L = 3 \text{ Mpc}$. The result is shown in Figure 46 in a plot of baryon overdensity δ versus gas temperature. In the plot, the area in blue is our estimated filament density. The curves represent the SXS 3σ detection limit for OVII and OVIII alone and for the combination of the two. For reasonable values of the filament temperature (1-3 million degrees), we expect a 200 ks pointing with SXS to be sensitive to baryon overdensities of about 100 or higher, which is well within the range of expected densities for the filament.

8.4 Between A2804 and A2811 in the Sculptor supercluster

Most of the considerations for this target are similar to those discussed in the previous subsection and won't be repeated here. A *Suzaku* investigation has not found any evidence of excess emission attributable to the filament and upper limits have been set. Using *Suzaku* and data toward the “filament” for the evaluation of the CXB, the expected SXS detector background, and assuming a 200 ks pointing, the 3σ detection limit for the combined oxygen lines is $0.6 \text{ ph s}^{-1} \text{ cm}^{-2} \text{ sr}^{-1}$, which improves the current limits (Sato et al., 2010) by about a factor of 1.5.

It is important to notice that, while a factor of 1.5 may not seem like a significant improvement compared

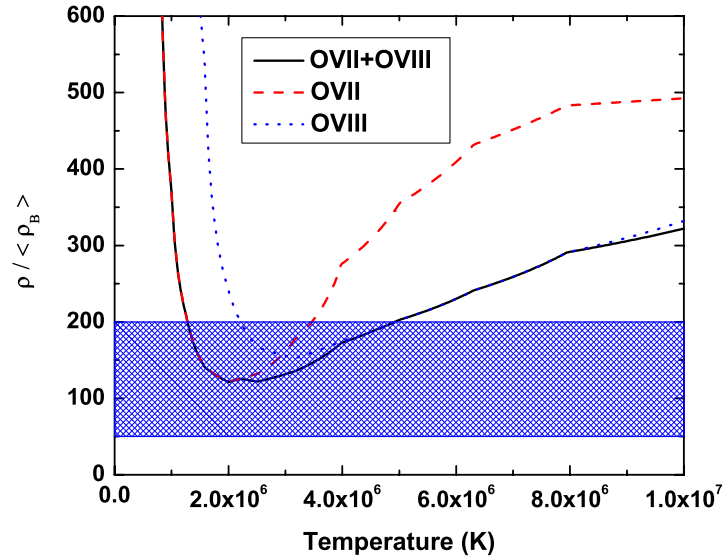


Figure 46: Expected gas overdensity in the region between A3556 and A3558 (blue shaded area), compared with the expected sensitivity (3σ) of SXS for a 200 ks pointing, as a function of the filament temperature. The curves represent the limit assuming that only OVII or OVIII is detected and for a combination of the two. The derived overdensity depends on metallicity and the line-of-sight extent of WHIM as $(Z/0.3Z_{\odot})^{-1/2}(L/3 \text{ Mpc})^{-1/2}$.

to previous investigations, there are compelling factors making this a quite interesting target and SXS a unique instrument for such investigation. First of all, the *Suzaku* limits were obtained by looking at the shape of the oxygen lines, searching for redshifted lines “hiding” behind the local emission. However, SXS will be able to clearly resolve and identify, if present, the redshifted oxygen lines due to the WHIM filament, with a significant reduction in systematic errors, and the possibility of combining multiple lines, beyond just oxygen, to improve the sensitivity. Moreover, the *Suzaku* investigation used the full $18' \times 18'$ XIS field of view, which is optimized for the filament detection. With the smaller $3' \times 3'$ SXS field of view it is possible to effectively go much deeper for a region right at the core of the filament.

8.4.1 Science outcome

Studying the filament between A222 and A223 would guarantee a positive result and significantly improve our understanding of the filament. However, its temperature and density are somewhat outside what is believed to be the bulk of the WHIM, limiting the broader impact of such investigation.

The pointing toward Shapley provides the most improvement in sensitivity compared to current limits. This is a high appealing target and could provide the first evidence of a filament between the two clusters. However, the proximity between clusters places the pointing at the limit of the virial radius of the two clusters. While such gas has not been investigated before, any positive detection would bear the question on whether it is due to true WHIM or the clusters.

On the other hand, the chance of detecting and studying a true WHIM filament in Sculptor is high risk (there is a chance that the filament is below the SXS detection threshold), but also high reward. The pointing in this case will be clearly outside the virial region of either cluster, guaranteeing that any detection will be associated with the WHIM filament. Moreover, the SXS energy resolution would guarantee a clean, uncontroversial detection of the filament and provides the possibility of further studying its characteristics.

9 A Spectroscopic Search for Dark Matter

Overview

X-ray spectroscopic observations provide a unique probe of direct signatures of dark matter, such as a decay line of a hypothetical sterile neutrino in the \sim keV mass range. In the event that any candidate emission line is detected in the 1 – 10 keV energy band, *ASTRO-H*SXS will offer the first opportunity to resolve its shape and distinguish it from plasma lines and instrumental effects. The significance of dark matter identification will be improved crucially if the line is detected from multiple sources with distinguishable differences in redshifts and velocity dispersions. Plausible targets include nearby galaxy clusters, the Milky Way Galaxy, and dwarf spheroidal galaxies, many of which will be observed by SXS for other purposes.¹⁶

9.1 Background and Previous Studies

The nature of dark matter is one of the fundamental unsolved problems in physics. Despite intensive search both in laboratories and from celestial objects, a direct identification is yet to be made. X-ray observations provide a direct probe of dark matter particles in the \sim keV mass range, which often comprise warm dark matter. They are of particular astrophysical interest because they alleviate several known problems of the conventional cold dark matter model (e.g., Weinberg et al., 2013). In addition, the mass of any fermionic dark matter should lie above the robust Tremaine-Gunn bound of \sim 0.3 keV (Tremaine & Gunn, 1979; Boyarsky et al., 2009).

A representative candidate of \sim keV mass dark matter is a sterile neutrino which arises in some extensions of the standard model of particle physics (Dodelson & Widrow, 1994; Shi & Fuller, 1999). The dark matter sterile neutrino is predicted to decay and emit a line in the X-ray energy band (Abazajian et al., 2001); even if its lifetime is much longer than the age of the Universe, the decay signal may reach a level accessible by existing and future instruments, owing to the high concentration of dark matter over the large volume of galaxies and galaxy clusters. Other candidates that can be searched for in X-rays include moduli (Kusenko et al., 2012) and axions (e.g., Higaki et al., 2014).

While most of previous dark matter searches in X-rays resulted only in upper limits (see Abazajian et al., 2012; Boyarsky et al., 2012, for reviews), there have also been reports on unidentified emission lines at \sim 3.5 keV from a sample of galaxy clusters and M31 (Bulbul et al., 2014; Boyarsky et al., 2014). For any candidate line that has been (or will be) inferred, the spectral resolution of current X-ray CCD detectors is still insufficient for resolving its shape and distinguishing it from plasma lines and instrumental effects. Key quantities in this regard are accurate centroid energy and width of the line. The former is crucial for identifying the line in a variety of astronomical objects at various redshifts, whereas the latter for extracting the velocity dispersion of dark matter which in general is different from thermal and turbulent velocities of metals in the plasma. The *ASTRO-H*SXS will provide the first opportunity to explicitly probe these quantities simultaneously.

9.2 Prospects and Strategy

For an arbitrary dark matter particle of mass m_{dm} that decays into a photon of energy E_γ at the rate per unit time Γ , the number of photons observed at the energy $E_{\text{obs}} = E_\gamma/(1+z)$ per unit area, unit solid angle, and unit time is given by

$$\mathcal{N}_\gamma = \frac{\Sigma_{\text{dm}}}{4\pi(1+z)^3} \frac{\Gamma}{m_{\text{dm}}} \quad (4)$$

$$\simeq 9.3 \times 10^{-5} \text{ cm}^{-2} \text{ sr}^{-1} \text{ s}^{-1} \frac{1}{(1+z)^3} \left(\frac{\Sigma_{\text{dm}}}{10^3 M_\odot \text{ pc}^{-2}} \right) \left(\frac{\Gamma}{10^{-32} \text{ s}^{-1}} \right) \left(\frac{m_{\text{dm}}}{\text{keV}} \right)^{-1}, \quad (5)$$

¹⁶Coordinators of this section: T. Kitayama, T. Tamura, S. W. Allen

where z is the source redshift, and Σ_{dm} is the dark matter mass column density. For example, a sterile neutrino is expected to decay into an active neutrino and a photon of energy $E_\gamma = m_{\text{dm}}c^2/2$ at the rate

$$\Gamma \simeq 1.4 \times 10^{-32} \text{s}^{-1} \left(\frac{\sin^2 2\theta}{10^{-10}} \right) \left(\frac{m_{\text{dm}}}{\text{keV}} \right)^5, \quad (6)$$

where θ is the mixing angle with the active neutrino (Pal and Wolfenstein, 1982; Loewenstein et al., 2009). Given the knowledge of Σ_{dm} toward the source, the intensity and the energy of the decay line hence give a measure of m_{dm} and Γ (or θ for the sterile neutrino).

The FWHM of the observed line is given by a convolution of the instrumental width W_{inst} (eq. [10]) and the width determined by the line-of-sight velocity dispersion σ_{dm} of the dark matter:

$$W_{\text{dm}} \simeq 7.9 \text{ eV} \left(\frac{\sigma_{\text{dm}}}{1000 \text{ km/s}} \right) \left(\frac{E_{\text{obs}}}{\text{keV}} \right). \quad (7)$$

It follows that $W_{\text{inst}} < 10 \text{ eV}$ is essential for resolving the decay line and distinguishing it from plasma lines that are broadened separately by thermal and turbulent motions of the gas (eqs [11] and [12]). The high spectral resolution is also crucial for eliminating the instrumental effects intrinsic to particular energies by comparing the positions of the line centroid from multiple sources with redshift differences down to $\Delta z < 10^{-2}$.

Equation (4) further indicates that, for given Γ/m_{dm} , stronger signals are expected from the targets with higher mass column within the field-of-view ($3' \times 3'$) of SXS. As shown in the next section, they include nearby galaxy clusters, the Milky Way Galaxy, and dwarf spheroidal galaxies. Long exposures are still required to detect (or place meaningful limits on) yet unidentified lines owing to the limited grasp (effective area times the field-of-view) of *ASTRO-H* SXS. A practical strategy will be to make use of the data obtained for other purposes and, if necessary, perform additional observations covering a range of redshifts and velocity (or mass) scales. In what follows, we examine the feasibility in more detail by taking into account relevant plasma emission, background components, and instrumental capabilities.

9.3 Targets and Feasibility

Figure 47 compares the normalized intensity, the quantity given by equation (4) divided by Γ/m_{dm} , from various targets (L. Strigari, private communication). Under the assumed density profile, the Milky Way appears to be a plausible target for a detection of the decay signal. The caveats are the high absorption column density and the bright X-ray emission in the vicinity of the Galactic center. One should hence choose carefully the regions of low Galactic absorption like the “1.5 degree Window” at $(l, b) = (0.08^\circ, -1.42^\circ)$ with $N_{\text{H}} \sim 7.5 \times 10^{21} \text{ cm}^{-2}$ or those in the lower brightness Galactic bulge (see also an accompanying *ASTRO-H* white paper (Koyama et al., 2014) on the feasibility toward the bulge regions). It should also be noted that the uncertainty in the dark matter mass profile toward the Galactic center will be a major source of systematic errors in the measured (or constrained) values of Γ (or θ for the sterile neutrino) from the data.

Clusters of galaxies provide complementary probes of the decay signal with better knowledge of the mass profile, lower absorption columns, and larger velocity dispersions. Observations of galaxy clusters at different redshifts and/or comparisons with the Milky Way will also be crucial for removing any instrumental effects. The pointings toward nearby clusters such as Perseus ($z = 0.0179$; Sec. 2), Virgo ($z = 0.0043$; Sec. 3), and Coma ($z = 0.0231$; Sec. 5) discussed in other sections of this paper will automatically provide useful data sets for this purpose.

Figure 48 shows simulated spectra toward the core of Perseus cluster. We confirm the results of Bulbul et al. (2014) that a 1 Ms exposure by SXS through this cluster will allow us to resolve the shape of the dark matter line inferred from the *XMM-Newton* data and distinguish it from plasma lines and instrumental effects. Note that the bright thermal emission from the intracluster plasma dominates the background toward the cluster cores. The relative importance of the dark matter line over the thermal emission is likely to increase with the distance from the core because the emissivity of the plasma is proportional to the gas density squared whereas

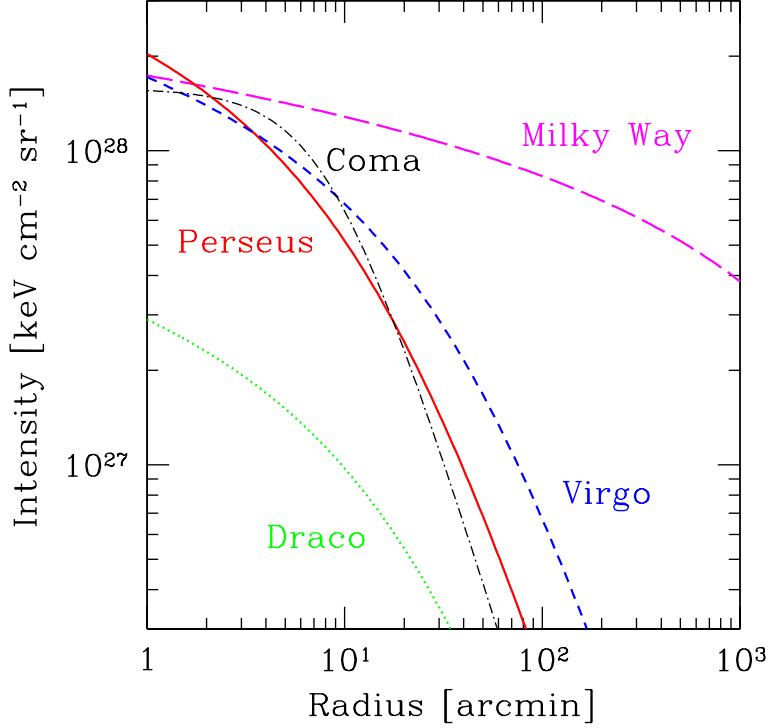


Figure 47: Normalized intensity (eq. [4] divided by Γ/m_{dm}) of a dark matter decay line from various targets as a function of the angle from the center (L. Strigari, private communication). The NFW dark matter density profile $\rho(r) = \rho_s(r/r_s)^{-1}(1+r/r_s)^{-1}$ is assumed with $(r_s, \rho_s) = (22 \text{ kpc}, 4.9 \times 10^{15} M_\odot \text{Mpc}^{-3})$ for the Milky Way (magenta long dashed line, Boyarsky et al., 2007), $(0.8 \text{ kpc}, 6.0 \times 10^{15} M_\odot \text{Mpc}^{-3})$ for the Draco dwarf galaxy (green dotted line, Strigari et al., 2007), $(430 \text{ kpc}, 1.0 \times 10^{15} M_\odot \text{Mpc}^{-3})$ for Perseus (red solid line), and $(250 \text{ kpc}, 1.0 \times 10^{15} M_\odot \text{Mpc}^{-3})$ for Virgo (blue short dashed line). For Coma (black dot-dashed line), the density profile $\rho(r) = \rho_0[1 + (r/r_c)^2]^{-3/2}$ is assumed with $(r_c, \rho_0) = (230 \text{ kpc}, 3.9 \times 10^{15} M_\odot \text{Mpc}^{-3})$. The density profiles of Perseus, Virgo, and Coma are consistent with the observed mass-temperature relation of local clusters (Vikhlinin et al., 2009a).

that of the decay line depends linearly on the dark matter density. The spatial variation of the ratio between the two can in turn be used to test the origin of the line.

Dwarf spheroidal galaxies such as Draco will offer yet further tests of a dark matter line against diffuse plasma emission and instrumental effects. Their observed stellar velocity dispersions of $10 - 30 \text{ km s}^{-1}$ (Mateo, 1998) imply that 1) broadening of the line should be well below the instrumental width (eq. [7]) and 2) contamination by plasma emission is very low since the diffuse X-ray gas cannot be sustained by their shallow gravitational potential. The caveats are the weaker decay signal and the larger uncertainty of the mass profile than the other targets mentioned above. Simulated spectra of a typical dwarf galaxy with a range of hypothetical sterile neutrino lines are shown in Figure 49. The continuum is dominated by instrumental and cosmic X-ray backgrounds with the expected brightness lower by about three orders of magnitude than the Perseus core (Figure 48). For a given value of θ , one expects a stronger line from the sterile neutrino decay at higher energies up to $\sim 10 \text{ keV}$. This is a result of two competing effects; Γ increases rapidly with m_{dm} (eq. [6]) whereas the effective area of SXS decreases with energy. It follows that the stronger limit on θ will be derived at higher energies in the case of no detection.

Figure 50 further illustrates the predicted line sensitivity of *ASTRO-H*SXS as compared to an existing X-ray CCD on board *Suzaku* (XIS). Note that this figure ignores any diffuse emission other than the instrumental background and the cosmic X-ray background; it corresponds to the limits that can be derived for X-ray faint sources such as dwarf spheroidal galaxies. In such cases, the sensitivity above $\sim 1 \text{ keV}$ is essentially photon limited after $\sim 100 \text{ ks}$ exposures, whereas the sensitivity in the softer energies remains background limited

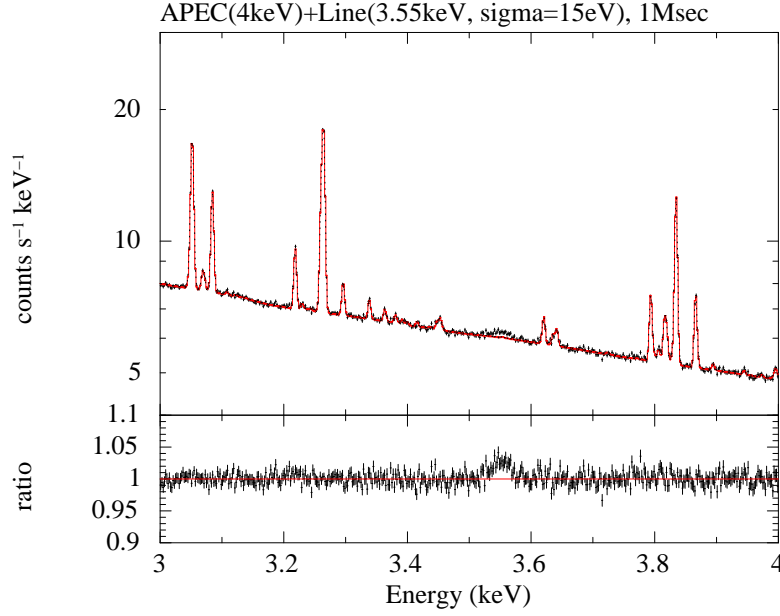


Figure 48: Simulated spectra of the Perseus core at $z = 0.0178$ with (black) and without (red) a dark matter line at 3.55 keV after an exposure of 1 Msec by SXS. For the dark matter line, we adopt the flux 3×10^{-5} ph s $^{-1}$ cm $^{-2}$ within the field-of-view of SXS from Table 5 of Bulbul et al. (2014) and $W_{\text{dm}} = 35$ eV corresponding to the velocity dispersion $\sigma_{\text{dm}} = 1300$ km s $^{-1}$. For the ICM thermal emission, we assume $kT = 4$ keV and $Z = 0.7$ solar with no turbulent broadening.

mainly due to the Galactic line emission. A major improvement in the sensitivity is expected in the hard band for the flux within the field-of-view of SXS, whereas the sensitivity is largely limited by the small grasp of SXS for the flux from the larger sky area. We stress that a highly improved spectral resolution will still be indispensable for identifying or rejecting any candidate lines once they are suggested.

Acknowledgments

We thank Louis Strigari, Ayuki Kamada, and Naoki Yoshida for many useful discussions on the dark matter search and their considerable input to Section 9.

Appendix

A Systematic Errors in Gas Velocities

For bright X-ray sources such as cores of nearby galaxy clusters, the accuracy of gas velocity measurements by *ASTRO-H*SXS can be limited by systematic errors rather than statistical errors. This section summarizes potential sources of the systematic errors and how they affect the measurements of bulk and turbulent velocities.

A.1 Bulk Velocity

Calibration errors in the energy gain ΔE_{gain} directly lead to the uncertainty in the line-of-sight bulk velocity measured by a line shift as

$$\Delta v_{\text{bulk}} = c \frac{\Delta E_{\text{gain}}}{E_{\text{obs}}} = 45 \text{ km/s} \left(\frac{\Delta E_{\text{gain}}}{\text{eV}} \right) \left(\frac{E_{\text{obs}}}{6.7 \text{ keV}} \right)^{-1}, \quad (8)$$

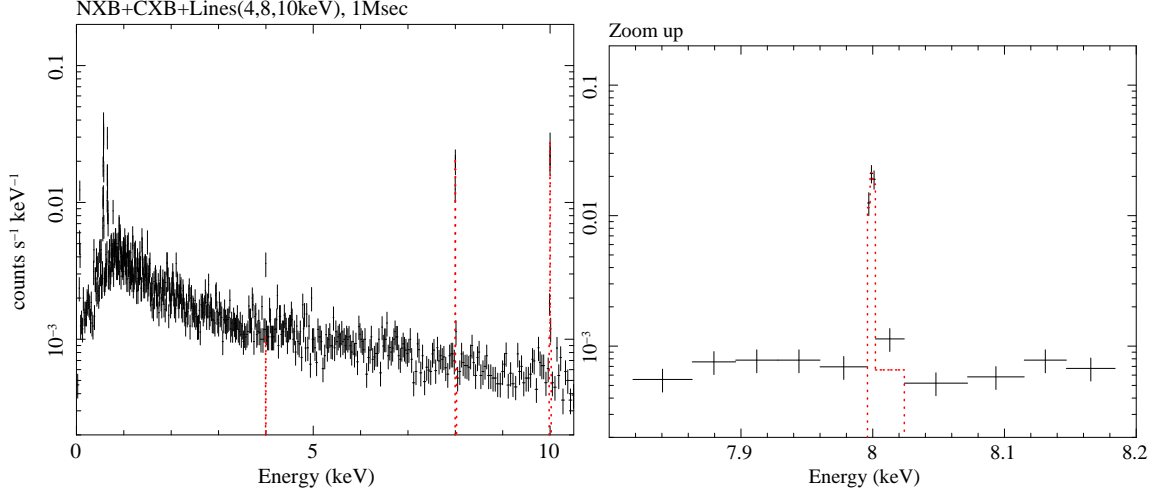


Figure 49: *Left:* A 1 Msec SXS simulated spectrum of a dwarf galaxy. We incorporate a range of hypothetical sterile neutrino lines (red dotted) at 4.0, 8.0, and 10.0 keV for $\Sigma_{\text{dm}} = 100 M_{\odot} \text{ pc}^{-2}$ and $\sin^2 2\theta = 10^{-10}$ corresponding to the flux 0.04 , 0.65 , and $1.6 \times 10^{-6} \text{ ph s}^{-1} \text{ cm}^{-2}$, respectively, within the field-of-view of SXS. The adopted value of Σ_{dm} is typical of local dwarf spheroidals and that of $\sin^2 2\theta$ lies close to the current observational limits. No diffuse galactic emission nor observable line broadening is assumed. The sum (black solid) includes instrumental and cosmic background models taken from the *ASTRO-H* internal release (sxs_cxb+nxb_7ev_20110211_1Gs.pha). *Right:* Same as the left panel, except that the line at 8 keV is zoomed in.

where E_{obs} is the observed energy of the line.

A.2 Turbulent Velocity

The line-of-sight component of the turbulent velocity measured by line broadening can be affected by calibration errors in instrumental broadening due to the line spread function and uncertainties in thermal broadening characterized by the ion temperature.

To quantify their impacts, let us decompose the observed FWHM of a spectral line, assuming a Gaussian profile for each component, as

$$W_{\text{obs}}^2 = W_{\text{inst}}^2 + W_{\text{therm}}^2 + W_{\text{turb}}^2 + \dots, \quad (9)$$

where W_{inst} , W_{therm} , and W_{turb} are the FWHMs of instrumental broadening, thermal broadening, and turbulent broadening, respectively. Their nominal values are

$$W_{\text{inst}} \simeq 5 \text{ eV}, \quad (10)$$

$$\begin{aligned} W_{\text{therm}} &= \sqrt{8 \ln 2} \left(\frac{kT_{\text{ion}}}{m_{\text{ion}} c^2} \right)^{1/2} E_{\text{obs}}, \\ &= 4.9 \text{ eV} \left(\frac{kT_{\text{ion}}}{5 \text{ keV}} \right)^{1/2} \left(\frac{m_{\text{ion}}}{56 m_{\text{p}}} \right)^{-1/2} \left(\frac{E_{\text{obs}}}{6.7 \text{ keV}} \right), \end{aligned} \quad (11)$$

$$\begin{aligned} W_{\text{turb}} &= \sqrt{8 \ln 2} \left(\frac{v_{\text{turb}}}{c} \right) E_{\text{obs}}, \\ &= 5.3 \text{ eV} \left(\frac{v_{\text{turb}}}{100 \text{ km/s}} \right) \left(\frac{E_{\text{obs}}}{6.7 \text{ keV}} \right), \end{aligned} \quad (12)$$

where T_{ion} and m_{ion} are the temperature and the mass of the ion producing the line observed at E_{obs} , m_{p} is the proton mass, and v_{turb} is the RMS turbulent velocity along the line of sight. Note that natural line broadening takes a Lorentzian profile with the FWHM of

$$W_{\text{nat}} = \hbar A = 0.31 \text{ eV} \left(\frac{A}{4.67 \times 10^{14} \text{ s}^{-1}} \right), \quad (13)$$

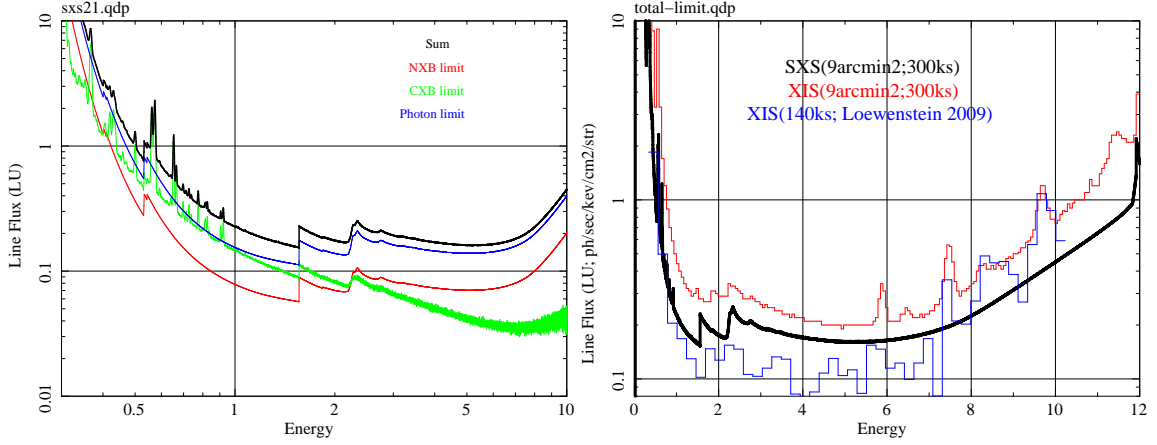


Figure 50: *Left:* The 3σ line sensitivities over a sky coverage $\Omega = 9 \text{ arcmin}^2$ after a 300 ks exposure in unit of LU (line unit; photons $\text{cm}^{-2} \text{ s}^{-1} \text{ str}^{-1}$) for *ASTRO-H/SXS*. We assume that the signal-to-noise ratio (S/N) in an energy bin is given by $\sqrt{C_{\text{Line}}^2 / (C_{\text{Line}} + 2C_{\text{B}})}$, where C_{Line} and C_{B} denote the counts of a line and background, respectively (e.g. Bradt, 2004). The 'photon limit' (blue) assumes $C_{\text{Line}} \gg C_{\text{B}}$, whereas 'Background limits' (red and green) $C_{\text{Line}} \ll C_{\text{B}}$. The 'Sum' (black) is calculated by adding these components in quadrature. The instrumental background (NXB) and the cosmic X-ray background (CXB) models are taken from the *ASTRO-H* SWG internal release. *Right:* The same quantity as the left panel for *Suzaku* XIS (2FI; red) and *ASTRO-H/SXS* (black). Also shown for reference is the limits for *Suzaku* XIS with $\Omega = 240 \text{ arcmin}^2$ (blue) from Loewenstein et al. (2009) obtained using a Monte Carlo simulation.

where A is the Einstein coefficient and the quoted value is for the Fe XXV resonant line at 6.7 keV. The presence of natural broadening has little effect on the decomposition given by equation (9) and on the results presented in this section.

In the following, we quantify the errors in W_{turb} arising from those in W_{inst} and W_{therm} . Note that a conventional error propagation law of the form

$$\Delta W_{\text{turb}} = \left| \frac{\partial W_{\text{turb}}}{\partial W_{\text{inst}}} \right| \Delta W_{\text{inst}} = \frac{W_{\text{inst}}}{W_{\text{turb}}} \Delta W_{\text{inst}} \quad (14)$$

is NOT valid for $\Delta W_{\text{turb}} > W_{\text{turb}}$ because equation (14) is based on a linear approximation; e.g., ΔW_{turb} diverges as $W_{\text{turb}} \rightarrow 0$, even if W_{inst} and ΔW_{inst} are both finite. We may readily face such a situation if the observed turbulence is small and only an upper limit is to be placed on W_{turb} . We hence present more general expressions of ΔW_{turb} . The conversion to Δv_{turb} is done by

$$\Delta v_{\text{turb}} = \frac{c}{\sqrt{8 \ln 2}} \frac{\Delta W_{\text{turb}}}{E_{\text{obs}}} = 19 \text{ km/s} \left(\frac{\Delta W_{\text{turb}}}{\text{eV}} \right) \left(\frac{E_{\text{obs}}}{6.7 \text{ keV}} \right)^{-1}. \quad (15)$$

A.2.1 Instrumental broadening

Equation (9) implies that ΔW_{inst} alone gives rise to ΔW_{turb} via

$$\Delta(W_{\text{turb}}^2) = \Delta(W_{\text{inst}}^2), \quad (16)$$

where, for an arbitrary component j ,

$$\Delta(W_j^2) \equiv (W_j + \Delta W_j)^2 - W_j^2 = 2W_j \Delta W_j + (\Delta W_j)^2. \quad (17)$$

Equation (16) is quadratic in ΔW_{turb} and yields

$$\Delta W_{\text{turb}} = -W_{\text{turb}} + \sqrt{W_{\text{turb}}^2 + \Delta(W_{\text{inst}}^2)}, \quad (18)$$

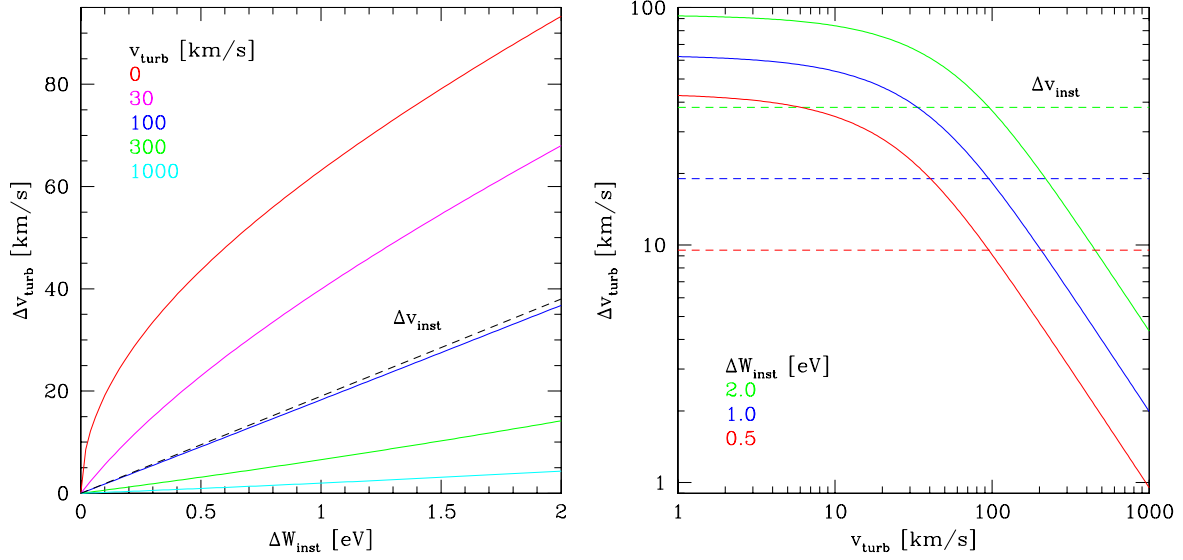


Figure 51: Δv_{turb} originating from instrumental broadening (eq. [18]) as a function of ΔW_{inst} (left panel) and v_{turb} (right panel) in the case of $W_{\text{inst}} = 5$ eV and $E_{\text{obs}} = 6.7$ keV. For reference, dashed lines show Δv_{inst} defined by equation (23). The color assignment is indicated in the panels.

whereas the other solution, $-W_{\text{turb}} - \sqrt{W_{\text{turb}}^2 + \Delta(W_{\text{inst}}^2)}$, is irrelevant here (it is nonzero for $\Delta(W_{\text{inst}}^2) = 0$). Equation (18) depends on both W_{inst} and ΔW_{inst} . Its asymptotes are:

1. For $\Delta W_{\text{turb}} \ll W_{\text{turb}}$ and $\Delta W_{\text{inst}} \ll W_{\text{inst}}$,

$$\begin{aligned} \Delta W_{\text{turb}} &\simeq \frac{W_{\text{inst}}}{W_{\text{turb}}} \Delta W_{\text{inst}}, \quad (\text{in agreement with eq. [14]}) \\ &= 0.95 \text{ eV} \left(\frac{v_{\text{turb}}}{100 \text{ km/s}} \right)^{-1} \left(\frac{W_{\text{inst}}}{5 \text{ eV}} \right) \left(\frac{\Delta W_{\text{inst}}}{\text{eV}} \right) \left(\frac{E_{\text{obs}}}{6.7 \text{ keV}} \right)^{-1}, \end{aligned} \quad (19)$$

$$\Delta v_{\text{turb}} \simeq 18 \text{ km/s} \left(\frac{v_{\text{turb}}}{100 \text{ km/s}} \right)^{-1} \left(\frac{W_{\text{inst}}}{5 \text{ eV}} \right) \left(\frac{\Delta W_{\text{inst}}}{\text{eV}} \right) \left(\frac{E_{\text{obs}}}{6.7 \text{ keV}} \right)^{-2}. \quad (20)$$

2. For $\Delta W_{\text{turb}} \gg W_{\text{turb}}$ and $\Delta W_{\text{inst}} \ll W_{\text{inst}}$,

$$\begin{aligned} \Delta W_{\text{turb}} &\simeq \sqrt{2W_{\text{inst}}\Delta W_{\text{inst}}}, \quad (\text{independent of } v_{\text{turb}}) \\ &= 3.2 \text{ eV} \left(\frac{W_{\text{inst}}}{5 \text{ eV}} \right)^{1/2} \left(\frac{\Delta W_{\text{inst}}}{\text{eV}} \right)^{1/2}, \end{aligned} \quad (21)$$

$$\Delta v_{\text{turb}} \simeq 60 \text{ km/s} \left(\frac{W_{\text{inst}}}{5 \text{ eV}} \right)^{1/2} \left(\frac{\Delta W_{\text{inst}}}{\text{eV}} \right)^{1/2} \left(\frac{E_{\text{obs}}}{6.7 \text{ keV}} \right)^{-1}. \quad (22)$$

Figure 51 illustrates Δv_{turb} given by equations (18) and (15). At large v_{turb} , Δv_{turb} is nearly proportional to $\Delta W_{\text{inst}}/v_{\text{turb}}$ in agreement with the error propagation law of equation (14). At the smallest v_{turb} , on the other hand, Δv_{turb} does not diverge and is bounded by equation (22). Equation (22) corresponds to the “tightest upper limit on v_{turb} ” that can be inferred in the absence of other errors. In any case, it should be distinguished from

$$\Delta v_{\text{inst}} \equiv \frac{c}{\sqrt{8 \ln 2}} \frac{\Delta W_{\text{inst}}}{E_{\text{obs}}} = 19 \text{ km/s} \left(\frac{\Delta W_{\text{inst}}}{\text{eV}} \right) \left(\frac{E_{\text{obs}}}{6.7 \text{ keV}} \right)^{-1}. \quad (23)$$

A.2.2 Thermal broadening

Similarly, ΔW_{therm} contributes to ΔW_{turb} as

$$\Delta W_{\text{turb}} = -W_{\text{turb}} + \sqrt{W_{\text{turb}}^2 + \Delta(W_{\text{therm}}^2)}, \quad (24)$$

where, from equation (11),

$$\Delta(W_{\text{therm}}^2) = 4.7 \text{ eV}^2 \left(\frac{k\Delta T_{\text{ion}}}{\text{keV}} \right) \left(\frac{m_{\text{ion}}}{56m_{\text{p}}} \right)^{-1} \left(\frac{E_{\text{obs}}}{6.7\text{keV}} \right)^2. \quad (25)$$

Equation (24) depends on ΔT_{ion} but not on T_{ion} . Its asymptotes are:

1. For $\Delta W_{\text{turb}} \ll W_{\text{turb}}$,

$$\begin{aligned} \Delta W_{\text{turb}} &\approx \frac{1}{2} \frac{\Delta(W_{\text{therm}}^2)}{W_{\text{turb}}}, \quad (\text{in agreement with eq. [14]}) \\ &= 0.45 \text{ eV} \left(\frac{v_{\text{turb}}}{100\text{km/s}} \right)^{-1} \left(\frac{k\Delta T_{\text{ion}}}{\text{keV}} \right) \left(\frac{m_{\text{ion}}}{56m_{\text{p}}} \right)^{-1} \left(\frac{E_{\text{obs}}}{6.7\text{keV}} \right), \end{aligned} \quad (26)$$

$$\Delta v_{\text{turb}} \approx 8.6 \text{ km/s} \left(\frac{v_{\text{turb}}}{100\text{km/s}} \right)^{-1} \left(\frac{k\Delta T_{\text{ion}}}{\text{keV}} \right) \left(\frac{m_{\text{ion}}}{56m_{\text{p}}} \right)^{-1}, \quad (27)$$

2. For $\Delta W_{\text{turb}} \gg W_{\text{turb}}$,

$$\begin{aligned} \Delta W_{\text{turb}} &\approx \sqrt{\Delta(W_{\text{therm}}^2)}, \quad (\text{independent of } v_{\text{turb}}) \\ &= 2.2 \text{ eV} \left(\frac{k\Delta T_{\text{ion}}}{\text{keV}} \right)^{1/2} \left(\frac{m_{\text{ion}}}{56m_{\text{p}}} \right)^{-1/2} \left(\frac{E_{\text{obs}}}{6.7\text{keV}} \right), \end{aligned} \quad (28)$$

$$\Delta v_{\text{turb}} \approx 41 \text{ km/s} \left(\frac{k\Delta T_{\text{ion}}}{\text{keV}} \right)^{1/2} \left(\frac{m_{\text{ion}}}{56m_{\text{p}}} \right)^{-1/2}. \quad (29)$$

A.2.3 Combined error

Since uncertainties in the instrumental and thermal widths are in principle independent of each other, their contribution to $\Delta(W_{\text{turb}}^2)$ can be added in quadrature:

$$\{\Delta(W_{\text{turb}}^2)\}^2 = \{\Delta(W_{\text{inst}}^2)\}^2 + \{\Delta(W_{\text{therm}}^2)\}^2 + \dots, \quad (30)$$

$$\rightarrow \Delta W_{\text{turb}} = -W_{\text{turb}} + \sqrt{W_{\text{turb}}^2 + \left[\{\Delta(W_{\text{inst}}^2)\}^2 + \{\Delta(W_{\text{therm}}^2)\}^2 + \dots \right]^{1/2}}, \quad (31)$$

$$\approx \begin{cases} \frac{\left[\{\Delta(W_{\text{inst}}^2)\}^2 + \{\Delta(W_{\text{therm}}^2)\}^2 + \dots \right]^{1/2}}{2W_{\text{turb}}}, & (\Delta W_{\text{turb}} \ll W_{\text{turb}}) \\ \left[\{\Delta(W_{\text{inst}}^2)\}^2 + \{\Delta(W_{\text{therm}}^2)\}^2 + \dots \right]^{1/4}, & (\Delta W_{\text{turb}} \gg W_{\text{turb}}) \end{cases} \quad (32)$$

where $\Delta(W_{\text{turb}}^2)$ and $\Delta(W_{\text{inst}}^2)$ are given by equation (17), $\Delta(W_{\text{therm}}^2)$ by equation (25), and the dots represent the other random uncertainties including statistical errors.

Figure 52 shows Δv_{turb} given by equations (31) and (15). It follows that Δv_{turb} increases with decreasing v_{turb} and hampers the measurement of v_{turb} less than ~ 70 km/s, if $W_{\text{inst}} \simeq 5$ eV, $\Delta W_{\text{inst}} \simeq 1$ eV, and $k\Delta T_{\text{ion}} \simeq 1$ keV.

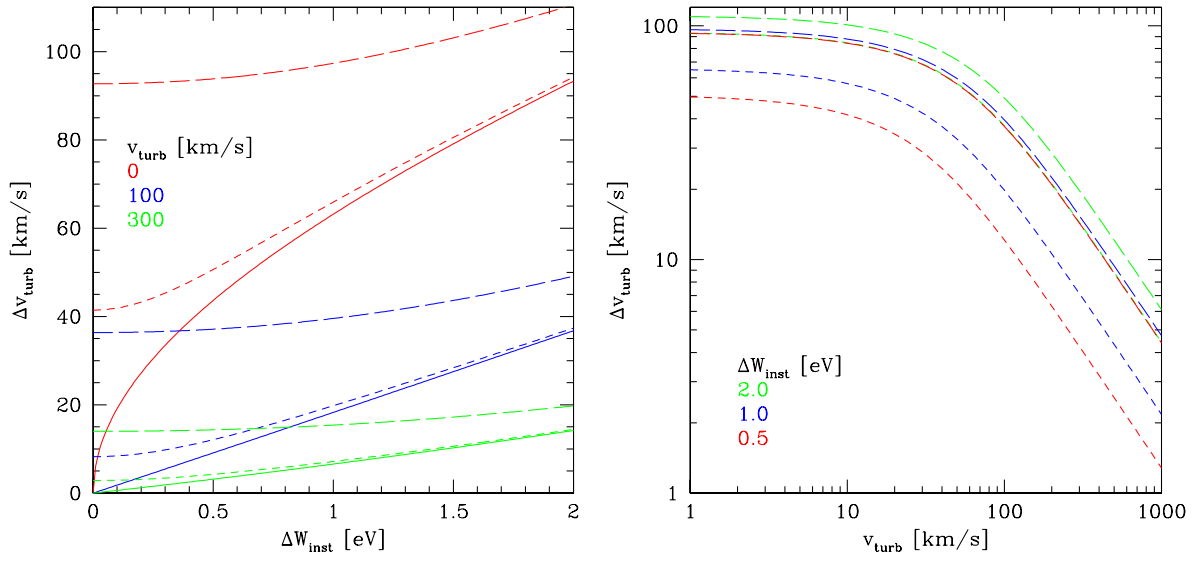


Figure 52: Same as Figure 51 except for adding uncertainties in thermal broadening (eq. [31]) with $k\Delta T_{\text{ion}} = 5$ keV (long dashed), 1 keV (short dashed), and 0 (solid; omitted for clarity in the right panel since the results are identical to Figure 51).

References

- Abazajian, K., Fuller, G. M., & Tucker, W. H. 2001, *ApJ*, 562, 593
- Abazajian, K., et al., 2012, arXiv:1204.5379
- Ackermann, M., et al. 2010, *ApJ*, 717, L71
- Ajello, M., et al. 2010, *ApJ*, 725, 1688
- Allen, S. W., Evrard, A. E., & Mantz, A. B. 2011, *ARA&A*, 49, 409
- Allen, S. W., Schmidt, R. W., Ebeling, H., Fabian, A. C., & van Speybroeck, L. 2004, *MNRAS*, 353, 457
- Allen, S. W., Rapetti, D. A., Schmidt, R. W., Ebeling, H., Morris, R. G., & Fabian, A. C. 2008, *MNRAS*, 383, 879
- Andersson, K., et al. 2009, *ApJ*, 696, 2019
- Badenes, C., Bravo, E., Hughes, J. P., 2008, *ApJ*, 680, L33
- Balestra, I., et al. 2007, *A&A*, 462, 429
- Belsole, E., et al. 2001, *A&A*, 365, L188
- Bennett 2003, *ApJS*, 148, 1
- Benson, B. A., et al. 2013, *ApJ*, 763, 147
- Biretta, J. A., Sparks, W. B., & Macchetto, F. 1999, *ApJ*, 520, 621
- Böhringer, H., Matsushita, K., Churazov, E., Finoguenov, A., & Ikebe, Y. 2004, *A&A*, 416, L21
- Böhringer, H., Nulsen, P. E. J., Braun, R., & Fabian, A. C. 1995, *MNRAS*, 274, L67
- Böhringer, H., Voges, W., Fabian, A. C., Edge, A. C., & Neumann, D. M. 1993, *MNRAS*, 264, L25
- Böhringer, H., Matsushita, K., Churazov, E., Finoguenov, A., & Ikebe, Y. 2004, *A&A*, 416, L21
- Bonafede, A., Feretti, L., Murgia, M., Govoni, F., Giovannini, G., Dallacasa, D., Dolag, K., Taylor, G. B., 2010, *A&A*, 513, 30
- Borgani, S. et al. 2004, *MNRAS*, 348, 1078
- Boyarsky, A., Iakubovskiy, D., & Ruchayskiy, O., 2012, *Phys. Dark Univ.*, 1, 136
- Boyarsky, A., Nevalainen, J., & Ruchayskiy, O. 2007, *A&A*, 471, 51
- Boyarsky, A., Ruchayskiy, O., & Iakubovskiy, D., 2009, *JCAP*, 03, 005
- Boyarsky, A., Ruchayskiy, O., Iakubovskiy, D., & Franse, J., 2014, arXiv:1402.4119
- Bradt, H. 2004, "Astronomy Methods", by Hale Bradt. ISBN 0521535514. UK: Cambridge University Press, 2004.
- Branchini, E., et al. 2009, *ApJ*, 697, 328
- Brunetti, G., & Jones, T. W. 2014, *International Journal of Modern Physics D*, 23, 30007
- Bulbul, E., Markevitch, M., Foster, A., Smith, R. K., Loewenstein, M., & Randall, S. W., *ApJ*, 789, 13
- Buote, D. A., et al. 2009, *ApJ*, 695, 1351
- Burles and Tytler 1998, *ApJ*, 499, 699
- Cen, R., Ostriker, J. P. 2006, *ApJ*, 650, 560
- Churazov, E., Brüggen, M., Kaiser, C. R., Böhringer, H., & Forman, W. 2001, *ApJ*, 554, 261
- Churazov, E., Forman, W., Jones, C., & Böhringer, H. 2000, *A&A*, 356, 788
- . 2003, *ApJ*, 590, 225
- Churazov, E., Forman, W., Jones, C., Sunyaev, R., & Böhringer, H. 2004, *MNRAS*, 347, 29
- Churazov, E., Zhuravleva, I., Sazonov, S., & Sunyaev, R. 2010, *Space Sci. Rev.*, 157, 193
- Danforth, C. W., et al. 2006, *ApJ*, 640, 716
- Danforth, C.W., & Shull, J.M. 2008, *ApJ*, 679, 194
- De Grandi, S., & Molendi, S. 2001, *ApJ*, 551, 153
- de Grandi, S., & Molendi, S. 2009, *A&A*, 508, 565
- de Plaa, J., et al. 2007, *A&A* 465, 345
- de Plaa, J., Zhuravleva, I., Werner, N., Kaastra, J. S., Churazov, E., Smith, R. K., Raassen, A. J. J., & Grange, Y. G. 2012, *A&A*, 539, A34
- Dodelson, S., & Widrow, L. M. 1994, *Phys. Rev. Lett.*, 72, 17
- Evrard, A. E. 1990, *ApJ*, 363, 349
- Fabian, A. C., et al. 2000, *MNRAS*, 318, L65
- Fabian, A. C., Hu, E. M., Cowie, L. L., & Grindlay, J. 1981, *ApJ*, 248, 47
- Fabian, A. C., Sanders, J. S., Allen, S. W., Crawford, C. S., Iwasawa, K., Johnstone, R. M., Schmidt, R. W., & Taylor, G. B. 2003a, *MNRAS*, 344, L43
- Fabian, A. C., Sanders, J. S., Crawford, C. S., Conselice, C. J., Gallagher, J. S., & Wyse, R. F. G. 2003b, *MNRAS*, 344, L48
- Fabian, A. C., Sanders, J. S., Taylor, G. B., Allen, S. W., Crawford, C. S., Johnstone, R. M. Iwasawa, K. 2006, *MNRAS*, 366, 417
- Fabian, A. C., Sanders, J. S., Williams, R. J. R., Lazarian, A., Ferland, G. J., & Johnstone, R. M. 2011, *MNRAS*, 417, 172
- Fang, T., Buote, D. A., Humphrey, P. J., Canizares, C. R., Zappacosta, L., Maiolino, R., Tagliaferri, G., Gastaldello, F. 2010, *ApJ*, 714, 1715
- Feigelson, E. D., Wood, P. A. D., Schreier, E. J., Harris, D. E., & Reid, M. J. 1987, *ApJ*, 312, 101
- Feltzing, S., & Gustafsson, B. 1998, *A&AS*, 129, 237

- Feretti, L., Giovannini, G., Govoni, F., & Murgia, M. 2012, *A&A Rev.*, 20, 54
- Finoguenov, A., Sarazin, C. L., Nakazawa, K., Wik, D. R., Clarke, T. E., *ApJ*, 715, 1143
- Forman, W., et al. 2005, *ApJ*, 635, 894
- . 2007, *ApJ*, 665, 1057
- Forman, W., Kellogg, E., Gursky, H., Tananbaum, H., & Giacconi, R. 1972, *ApJ*, 178, 309
- Fukazawa, Y., et al. 1998, *PASJ* 50, 187
- Fukugita 1998, *Phys. Rev. D* 58, 054503
- Fusco-Femiano, R., et al. 2000, *ApJ*, 534, L7
- Gabor, J. M., et al. 2010, *MNRAS* 407, 749
- Gabriel, A. H. 1972, *MNRAS*, 160, 99
- Galeazzi, M., Gupta, A., & Ursino, E. 2009, *ApJ*, 695, 1127
- Gal-Yam, A., et al. 2003, *ApJ*, 125, 1087
- Gilfanov, M. R., Sunyaev, R. A., & Churazov, E. M. 1987, *Soviet Astronomy Letters*, 13, 3
- Grange, Y.G., et al. 2011, *A&A* 531, A15
- Gratton, R. G., Carretta, E., Claudi, R., Lucatello, S., & Barbieri, M. 2003, *A&A*, 404, 187
- Grevesse, N., & Sauval, A. J. 1998, *Space Science Reviews*, 85, 161
- Gursky, H., Kellogg, E. M., Leong, C., Tananbaum, H., & Giacconi, R. 1971, *ApJ*, 165, L43
- Harris, D. E. & Romanishin, W. 1974, *ApJ*, 188, 209
- Higaki, T., Jeong, K. S., & Takahashi, F., *Physics Letters B*, 733, 25
- Howell, D. A. 2011, *Nature Communications* 2, 350
- Ichikawa, K., et al. 2013, *ApJ*, 766, 90
- Kaastra, J. S., Bykov, A. M., & Werner, N. 2009, *A&A*, 503, 373
- Kaastra, J. S., Mewe, R., & Nieuwenhuijzen, H. 1996, in *UV and X-ray Spectroscopy of Astrophysical and Laboratory Plasmas* p.411, K. Yamashita and T. Watanabe. Tokyo : Universal Academy Press
- Kapferer, W., Kronberger, T., Weratschnig, J., et al. 2007, *A&A*, 466, 813
- Kawaharada, M., et al. 2010, *ApJ*, 714, 423
- Kirkman 2003, *ApJS*, 149,1
- Kirkpatrick, C. C., McNamara, B. R., & Cavagnolo, K. W. 2011, *ApJ*, 731, L23
- Kitayama, T., Komatsu, E. Ota, N. Kuwabara, T. Suto, Y. Yoshikawa, K. Hattori, M. & Matsuo, H. 2004, *PASJ*, 56, 17
- Kitayama, T. 2014, *Prog. Theor. Exp. Phys.*, 06B111
- Kobayashi, C., Umeda, H., Nomoto, K., Tominaga, N., & Ohkubo, T. 2006, *ApJ*, 653, 1145
- Konami, S., Matsushita, K., Nagino, R., & Tamagawa, T. 2014, *ApJ*, 783, 8
- Koyama, K., et al., 2014, *ASTRO-H White Paper* (9)
- Kravtsov, A. V., Vikhlinin, A., & Nagai, D. 2006, *ApJ*, 650, 128
- Krivonos, R. A., Vikhlinin, A. A., Markevitch, M. L., & Pavlinsky, M. N. 2003, *Astronomy Letters*, 29, 425
- Kusenko, A., Loewenstein, M., & Yanagida, T. T., 2012, *Phys. Rev. D*, 87, 043508
- Lau, E. T., Kravtsov, A. V., & Nagai, D. 2009, *ApJ*, 705, 1129
- Lodders, K. 2003, *ApJ*, 591, 1220
- Loewenstein, M., Kusenko, A., & Biermann, P. L. 2009, *ApJ*, 700, 426
- Macario, G., Markevitch, M., Giacintucci, S., Brunetti, G., Ventura, T., & Murray, S. S. 2011, *ApJ*, 728, 82
- Mantz, A. B., Allen, S. W., Morris, R. G., Rapetti, D. A., Applegate, D. E., Kelly, P. L., von der Linden, A., & Schmidt, R. W. 2014, *MNRAS*, 440, 2077
- Markevitch, M. 2006, *The X-ray Universe 2005*, 604, 723
- Markevitch, M., & Vikhlinin, A. 2007, *Phys. Rep.*, 443, 1
- Mateo, M. L. 1998, *ARA&A*, 36, 435
- Matsushita, K., Belsole, E., Finoguenov, A., Böhringer, H. 2002, *A&A*, 386, 77
- Matsushita, K., Finoguenov, A., Boehringer, H. 2003, *A&A*, 401, 443
- Matsushita, K., Böhringer, H., Takahashi, I., & Ikebe, Y. 2007, *A&A*, 462, 953
- Matsushita, K. 2011, *A&A*, 527, A134
- Matsushita, K., Sakuma, E., Sasaki, T., Sato, K., & Simionescu, A. 2013, *ApJ*, 764, 147
- Matsushita, K., Sato, T., Sakuma, E., & Sato, K. 2013, *PASJ*, 65, 10
- Matteucci, F. & Calura, F. 2005, *MNRAS* 360, 447
- Maughan, B., et al. 2008, *ApJ*, 174, 117
- McNamara, B. R., Russell, H. R., Nulsen, P. E. J., et al. 2014, *ApJ*, 785, 44
- McNamara, B. R., & Nulsen, P. E. J. 2007, *ARA&A*, 45, 117
- McNamara, B. R., O'Connell, R. W., & Sarazin, C. L. 1996, *AJ*, 112, 91

- Mendygral, P. J., O'Neill, S. M., & Jones, T. W. 2011, *ApJ*, 730, 100
- Million, E., and Allen, S. W. 2009, *M.N.R.A.S.*, 39, 1307
- Million, E. T., Allen, S. W., Werner, N., & Taylor, G. B. 2010, *MNRAS*, 405, 1624
- Million, E. T., Werner, N., Simionescu, A., & Allen, S. W. 2011, *MNRAS*, 418, 2744
- Mitsuishi, I., Gupta, A., Yamasaki, N. Y., Takei, Y., Ohashi, T., Sato, K., Galeazzi, M., Henry, J. P., & Kelley, R. L. 2012, *PASJ*, 64, 18
- Molendi, S. 2002, *ApJ*, 580, 815
- Mushotzky, R., et al. 1996, *ApJ* 466, 686
- Nicastro, F., et al. 2005, *Nature*, 433, 495
- Nakazawa, K., et al. 2009, *PASJ*, 61, 339
- Nomoto, K., Tominaga, N., Umeda, H., Kobayashi, C., & Maeda, K. 2006, *Nuclear Physics A*, 777, 424
- Norman, M. L., & Bryan, G. L. 1999, *The Radio Galaxy Messier 87*, 530, 106
- O'Dea, C. P., Baum, S. A., Privon, G., et al. 2008, *ApJ*, 681, 1035
- Ota, N., et al. 2008, *A&A*, 491, 363
- Ota, N., et al. 2007, *PASJ*, 59, 351
- Paerels, F., et al., 2014, *ASTRO-H White Paper* (10)
- Pal, P. B., & Wolfenstein, L. 1982, *Phys. Rev. D*, 25, 766
- Panagoulia, E. K., Fabian, A. C., & Sanders, J. S. 2013, *MNRAS*, 433, 3290
- Peterson, J. R., & Fabian, A. C. 2006, *Phys. Rep.*, 427, 1
- Petrosian, V. 2001, *ApJ*, 557, 560
- Petrosian, V., Madejski, G., and Lili, K. 2006, *ApJ*, 652, 948
- Planck Collaboration XX, 2014, *A&A*, 571, A20
- Planelles, S., Borgani, S., Fabjan, D., et al. 2014, *MNRAS*, 438, 195
- Rasia, E., Meneghetti, M., Martino, R., et al. 2012, *New Journal of Physics*, 14, 055018
- Rauch 1998, *ApJ*, 489, 1
- Rebusco, P., Churazov, E., Böhringer, H., & Forman, W. 2006, *MNRAS*, 372, 1840
- Rebusco, P., Churazov, E., Sunyaev, R., Böhringer, H., & Forman, W. 2008, *MNRAS*, 384, 1511
- Rephaeli, Y., et al. 2006, *ApJ*, 649, 673
- Reiprich, T., et al. 2002, *ApJ*, 567, 716
- Röttgering, H. J. A., et al. 1997, *MNRAS*, 290, 577
- Ruiter, A. J., et al. 2009, *ApJ* 699, 2026
- Russell, H. R., McNamara, B. R., Sanders, J. S., et al. 2012, *MNRAS*, 423, 236
- Sakuma, E., Ota, N., Sato, K., Sato, T., & Matsushita, K. 2011, *PASJ*, 63, 979
- Sanders, J. S., & Fabian, A. C. 2006, *MNRAS*, 371, 1483
- . 2007, *MNRAS*, 381, 1381
- . 2011, *MNRAS*, 412, L35
- . 2012, *MNRAS*, 429, 2727
- Sanders, J. S., Fabian, A. C., Allen, S. W., & Schmidt, R. W. 2004, *MNRAS*, 349, 952
- Sanders, J. S., Fabian, A. C., & Smith, R. K. 2011, *MNRAS*, 410, 1797
- Sanders, J. S., Fabian, A. C., Smith, R. K., & Peterson, J. R. 2010, *MNRAS*, 402, L11
- Sasaki, S., 1996, *PASJ*, 48, L119
- Sato, K., et al. 2007, *ApJ* 667, L41
- Sato, K., Kawaharada, M., Nakazawa, K., Matsushita, K., Ishisaki, Y., Yamasaki, N. Y. & Ohashi, T. 2010, *PASJ*, 62, 1445
- Sato, K., Kelley, R. L., Takei, Y., Tamura, T., Yamasaki, N. Y., Ohashi, T., Gupta, A., & Galeazzi, M. 2010, *PASJ*, 62, 1423
- Schindler, S., & Diaferio, A. 2008, *SSRv*, 134, 363
- Shang, C., & Oh, S. P. 2012, *MNRAS*, 426, 3435
- . 2013, *MNRAS*, 433, 1172
- Shi, X., & Fuller, G. M. 1999, *Physical Review Letters*, 82, 2832
- Simionescu, A., Böhringer, H., Brüggén, M., & Finoguenov, A. 2007, *A&A*, 465, 749
- Simionescu, A., et al. 2011, *Science*, 331, 1576
- . 2012, *ApJ*, 757, 182
- Simionescu, A., Werner, N., Böhringer, H., Kaastra, J. S., Finoguenov, A., Brüggén, M., & Nulsen, P. E. J. 2009, *A&A*, 493, 409
- Simionescu, A., Werner, N., Finoguenov, A., Böhringer, H., & Brüggén, M. 2008, *A&A*, 482, 97
- Snowden, S. L., Mushotzky, R. F., Kuntz, K. D., & Davis, D. S. 2008, *A&A*, 478, 615
- Strickland, D. K., & Stevens, I. R. 2000, *MNRAS*, 314, 511
- Strigari, L. E., Koushiappas, S. M., Bullock, J. S., & Kaplinghat, M., 2007, *Phys. Rev.*, D75, 083526
- Takei, Y., et al. 2011, *ApJ*, 734, 91
- Tamura, T., et al. 2009, *ApJ*, 705, L62

- Tamura, T., Hayashda, K., Ueda, S., Nagai, M. 2011, PASJ, 63, S1009
- Tamura, T., et al. 2014, ApJ, 782, 38
- Tashiro, et al. (2014) *ASTRO-H* White Paper (20)
- Thom, C., & Chen, H.-W. 2008, ApJ, 683, 22
- Tilton, E. M., Danforth, C. W., Shull, J. M., Ross, T. L. 2012, ApJ, 759, 112
- Tremaine, S., & Gunn, J. E., 1979, Phys. Rev. Lett., 42, 407
- Tripp, T. M., Sembach, K. R., Bowen, D. V., Savage, B. D., Jenkins, E. B., Lehner, N., & Richter, P. 2008, ApJS, 177, 39
- Urban, O., et al. 2014, MNRAS, 437, 3939
- Ursino, E., & Galeazzi, M., 2006 ApJ, 652, 1085
- Ursino, E., Galeazzi, M., & Roncarelli, M. 2010, ApJ, 721, 46
- Vernaleo, J. C., & Reynolds, C. S. 2007, ApJ, 671, 171
- Vikhlinin, A., Markevitch, M., & Murray, S. S. 2001, ApJ, 551, 160
- Vikhlinin, A., et al. 2006, ApJ, 640, 691
- Vikhlinin, A., et al. 2009, ApJ, 692, 1033
- Vikhlinin, A., et al. 2009, ApJ, 692, 1060
- von der Linden, et al. 2014, MNRAS, 443, 1973
- Weinberg, D. H.; Miralda-Escude, J., Hernquist, L., & Katz, N., 1997, ApJ, 490, 564
- Weinberg, D. H., Bullock, J. S., Governato, F., de Naray, R. K., & Peter, A. H. G., 2013, arXiv:1306.0913
- Werner, N., Böhringer, H., Kaastra, J. S., de Plaa, J., Simionescu, A., & Vink, J. 2006, A&A, 459, 353
- Werner, N., et al. 2008, A&A, 482, L29
- Werner, N., et al. 2010, MNRAS, 407, 2063
- Werner, N., Urban, O., Simionescu, A., & Allen, S. W. 2013, Nature, 502, 656
- Werner, N., Zhuravleva, I., Churazov, E., Simionescu, A., Allen, S. W., Forman, W., Jones, C., & Kaastra, J. S. 2009, MNRAS, 398, 23
- White, S. D. M., Navarro, J. F., Evrard, A. E., & Frenk, C. S. 1993, Nature, 366, 429
- Wik, D., et al. 2009, ApJ, 696, 1700
- Wik, D., et al., 2014, ApJ, 792, 48
- Xu, H., et al. 2002, ApJ, 579, 600
- Young, A. J., Wilson, A. S., & Mundell, C. G. 2002, ApJ, 579, 560
- Zhang, Y.-Y., Laganá, T. F., Pierini, D., Puchwein, E., Schneider, P., & Reiprich, T. H. 2011, A&A, 535, A78
- Zhuravleva, I., Churazov, E., Kravtsov, A., & Sunyaev, R. 2012, MNRAS, 422, 2712
- Zhuravleva, I. V., Churazov, E. M., Sazonov, S. Y., Sunyaev, R. A., & Dolag, K. 2011, Astronomy Letters, 37, 141
- Zhuravleva, I., et al. 2013, MNRAS, 435, 3111
- Zhuravleva, I., et al. 2014, ApJ, 788, L13
- Zhuravleva, I., et al. 2014b, Nature, 515, 85
- ZuHone, J. A., Markevitch, M., Brunetti, G., & Giacintucci, S. 2013, ApJ, 762, 78